universität wien

DIPLOMARBEIT

Titel der Diplomarbeit

„Improvement of lithium ionic conduction properties in solid state garnet ceramic electrolytes“

Verfasserin

Barbara Stiaszny

angestrebter akademischer Grad

Magistra der Naturwissenschaften (Mag^{a}.rer.nat)

Wien, 2010

Studienkennzahl lt. Studienblatt:	A 419
Studienrichtung lt. Studienblatt:	Chemie
Betreuerin / Betreuer:	O. Univ.-Prof. Dr. Herbert Ipser

„Man muss nicht nur mehr Ideen haben als andere, sondern auch die Fähigkeit besitzen, zu entscheiden, welche dieser Ideen gut sind.“

Linus Pauling

Acknowledgement

This work was accomplished at the Robert-Bosch-GmbH in Stuttgart-Gerlingen from March 2010 until August 2010.

I'm grateful to the department CR/ARM2 of the Robert-Bosch-GmbH for the opportunity to write my diploma thesis in a perfectly equipped laboratory and internationally well-known company.

I want to express my greatest thanks to my supervisor Alan Logéat for all his support, his help during all the steps of my thesis, his readiness for discussions and his commitment.

Special thanks to Prof. Herbert Ipser, who enabled me to write my thesis in a company by adopting the academic supervision and who always was ready for external inputs.

Thanks to Dr. Ulrich Eisele (CR/ARM) for his interesting suggestions in all fields of my thesis, thanks to Dr. Jan Tomforde (CR/ARA), who facilitated a possibility to measure my sample by neutron diffraction. I also want to thank Dr. Thomas Köhler (CR/ARA), who performed the evaluation of neutron diffraction data. Many thanks to Dr. Christine Engel and Hideki Ogihara, who always helped me with questions and difficulties concerning impedance spectroscopy.

Thanks to the team of materialography (CR/ARM1) and the team of physical analytic (CR/ARA) who prepared lots of samples for materialographic investigation and accomplishment of all materialographic measurements.

I would like to thank my parents for all their interest and their support during my studies.

Finally I would like to thank my colleagues in the CR/ARM2 department creating a harmonically atmosphere and my friends for all their understanding and time.

Table of contents

1. Introduction

1.1. History of batteries – the development of galvanic elements:

In 1789 Luigi Galvani did the first experiments to create the basis for the development of the galvanic cells. He investigated the leg muscle contraction of a dead frog by touching it with an iron or zinc plate. Subsequently Alessandro Volta constructed the first suitable galvanic cell – the Voltaic Pile. The Pile was arranged by stacked copper and zinc discs, which were separated by an electrolyte. As the Voltaic Pile was very susceptible to corrosion, the British chemist John Frederic Daniell introduced the first cell containing two electrolytes in 1836. It consisted of a zinc electrode, a copper electrode and two electrolytes separated by a porous ion-conducting barrier. The electrolytes were $CuSO_4$ and H_2SO_4 and the operating voltage was around 1.1 V. From 1860, when the lead-acid-cell and the Leclanché-element were invented, many new types of cells were introduced for commercial use. [1,2]

Two general types of galvanic elements exist:

1. Primary cells, which are not rechargeable
2. Secondary cells, which can be recharged by applying a reversed excess voltage. [1]

1.2. Fundamentals:

In principle a galvanic element consists of two electrodes: the anode and the cathode, the electrolyte, the battery housing, the "active masses", which are converted at the electrodes, and if required a separator between the electrodes. [1]

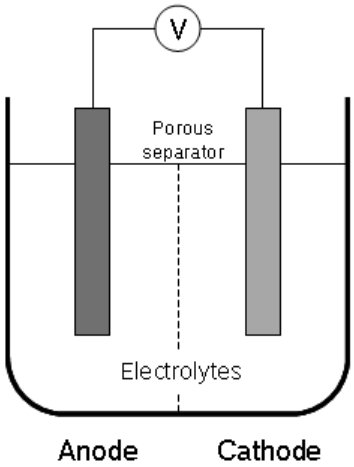

Fig.1.1: Schematic Assembly of a galvanic cell

In most of the cases, the active masses are arranged as electrodes in a solid state. Every electrochemical oxidisable substance can be used as “negative active mass”. Vice versa, every reducible matter can be used as “positive active mass”.

1.3. Primary cells:

In primary cells the “active masses” of the electrodes react irreversibly during the discharging process. Their field of application is most often in electronic portable devices with low current drain. Established types of disposable batteries are the zinc-carbon battery, lithium batteries, alkali-manganese batteries, zinc-mercury systems and the already mentioned Leclanché-element. [1]

1.3.1. Assembly and principles of the primary Lithium-battery (Li-MnO_2):

Within the lithium battery, lithium is used as “active mass” for the anode. As can be seen in Fig. 1.2 a non-aqueous aprotic electrolyte impregnated separator is located between the MnO_2-cathode and the anode.

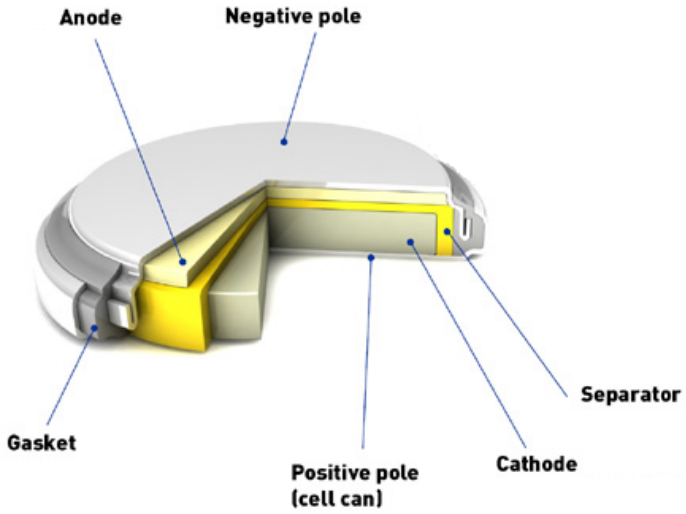

Fig.1.2: Assembly of a Li-MnO_2-button cell: consisting of a lithium metal anode, cathode (a MnO_2 powder + conducting carbon additive) and a lithium perchlorate or propylene carbonate electrolyte

The $LiMnO_2$ cell electrode reactions are given by equations Eq.(1.1.), Eq.(1.2.), Eq.(1.3.). A cell voltage of 3.2 V enables commercial producers to make a battery with a single cell.

Cathode: $MnO_2 + Li^+ + e^- \longrightarrow LiMnO_2$ Eq.(1.1)

Anode: $Li \longrightarrow Li^+ + e^-$ Eq.(1.2)

Total: $Li + MnO_2 \longrightarrow LiMnO_2$ Eq.(1.3)

Lithium batteries show several advantages, such as the high cell voltage up to 3.2 V, a wide working temperature range between -20 °C and +70 °C and high specific energies and energy densities of 70-120 Wh/kg, compared to conventional battery systems. Originally primary lithium batteries were used for military and aeronautic applications. Nowadays these batteries are also used in artificial pacemakers, watches and photo cameras, because of their low self-discharge. [4]

Primary cells have to fulfill special specifications to be applied:

- Wide working temperature range
- Low self discharge
- High efficiency
- Environmental compatibility

1.4. Secondary cells:

As long ago as 1802 Johann Wilhelm Ritter developed the first rechargeable battery followed by the invention of the lead-acid-cell. [2]

Secondary cells are rechargeable cells, whose electrochemical processes and electrode reactions are reversible. As the process can be repeated many times, such secondary cells are used as energy storage media for electricity. [10]

In addition to electrochemical reversible reactions, special specifications have to be fulfilled for every secondary battery:

- Long cycle stability
- Wide working temperature range
- Low self-discharge
- High efficiency
- Safe and fast charging
- Environmental compatibility

1.4.1. Types of secondary cells:

The most famous secondary cells are probably the lithium-metal and the lithium-ion battery, because of their miscellaneous applications. Contrary to the aforementioned lead-acid accumulator, the nickel-cadmium, the nickel-iron, the nickel-metal hydride and the silver-zinc battery lithium secondary cells contain non-aqueous electrolytes. [1]

1.4.1.1. Assembly and principles of the lead-acid accumulator:

The lead-acid accumulator consists of a Pb-anode, a PbO_2-coated lead grid as cathode, and aqueous H_2SO_4 as electrolyte. Electrodes are separated by a barrier to prevent them from contacting each other. The lead-acid electrode reactions are given by equations Eq.(1.4.), Eq.(1.5.), Eq.(1.6.) and provide a voltage of 2 V.

Cathode: $$PbO_2 + H_2SO_4 + 2H^+ + 2e^- \longleftrightarrow PbSO_4 + 2H_2O \qquad \text{Eq.(1.4)}$$

Anode: $$Pb + H_2SO_4 \longleftrightarrow PbSO_4 + 2H^+ + 2e^- \qquad \text{Eq.(1.5)}$$

Total: $$PbO_2 + Pb + H_2SO_4 \longleftrightarrow PbSO_4 + 2H_2O \qquad \text{Eq.(1.6)}$$

To obtain a commercially applicable accumulator, the “active masses” have to be arranged in a porous shape, to create a large surface where the electrochemical reaction can occur. As the discharging already finishes before the whole “active mass” is discharged, the mass exploitation of the lead-acid accumulator (and of most of the galvanic cells) is only about 50%.

For a common 12 V car battery, six cells have to be connected in series. [1,9,10]

The following Figure 1.3 gives a short overview of the specific energy [Wh/kg] versus the energy density [Wh/L] for several types of batteries. It can be seen that lithium ion batteries show high specific energy as well as high energy density, which mark them as best current battery systems and predestine them for future applications. Different cell geometries are used, which will be described later on in details.

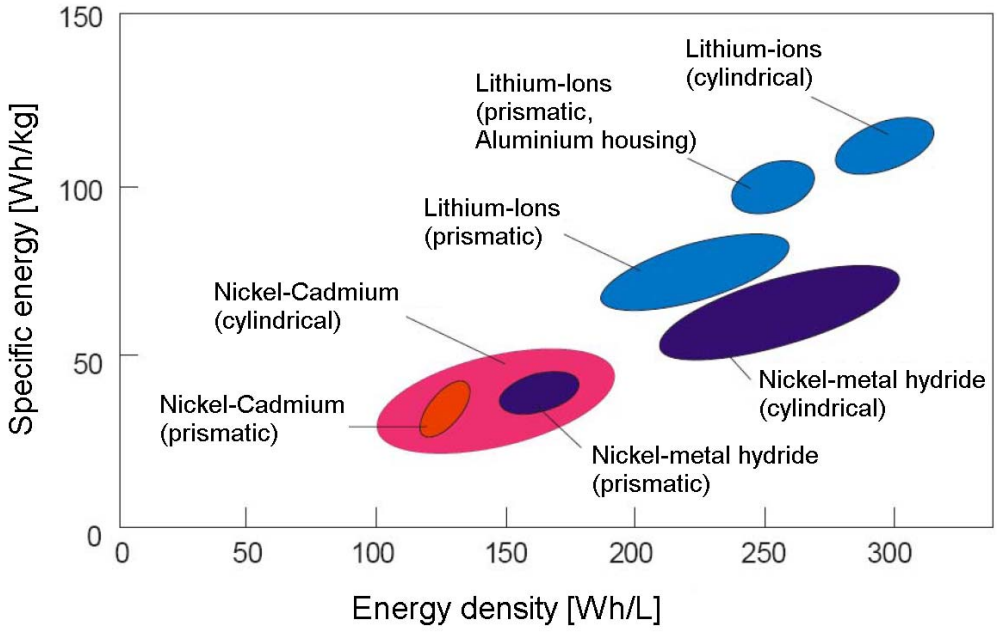

Fig. 1.3: Specific energies [Wh/kg] and energy densities [Wh/L] for small format accumulators. Compared to prismatic cells cylindrical cells can achieve higher energy densities per battery-housing volume, but prismatic cells fit better into angular devices.

The following two graphs in Figure 1.4 show the development of lithium ion batteries among secondary cells on the battery market.

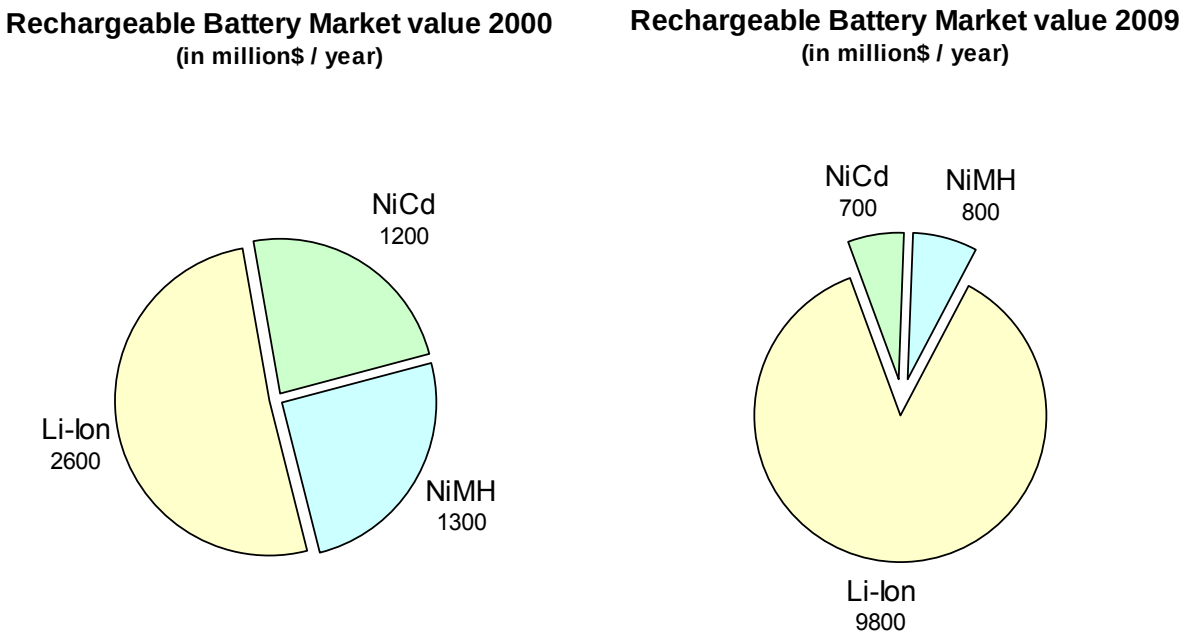

Fig.1.4: Development of market share of lithium ion batteries in 2000 (left) and 2009 (right). Values are given in million$ / year.

1.5. History and development of lithium ion batteries

Lithium is one of the most electronegative elements and thus exhibits the highest electrochemical standard potential. Consequently it shows higher energy densities than lead and zinc, which have been used in accumulators and batteries, respectively, for a long time.
In 1978 Exxon developed one of the first rechargeable batteries with metallic lithium as anode. These early batteries suffered from safety problems because of the tendency of lithium metal to build dendrites, which can lead to short circuits. Another great disadvantage is that lithium reacts intensively with water forming gaseous hydrogen, which can lead to an explosion of the cell. Nowadays, batteries with lithium metal electrodes are only permitted in coin cells.
Due to safety regulations, the attention in research and development was shifted to anode materials intercalated with lithium ions. In 1981 the first intercalation material was patented. In the same year B. Goodenough developed the cathode material $LiCoO_2$ which is still used. Ten years later, Sony Energytec Incorporation used these materials to produce the first commercial cells with an incorporated electronic circuitry to control the charge and discharge process. [3,8]

1.6. Assembly and principles of lithium-ion batteries

The main constituents of the lithium-ion battery are:

- A highly conducting lithium ion electrolyte
- Lithium storing anode and cathode
- Mechanically and chemically stable separator
- Current collectors at both electrodes

Lithium is the active species within lithium-ion systems. Both electrodes act as host lattices, where ions are stored during charging and discharging.
During charging process, lithium ions are transported from the cathode via the electrolyte to the anode as shown in Figure 1.5.

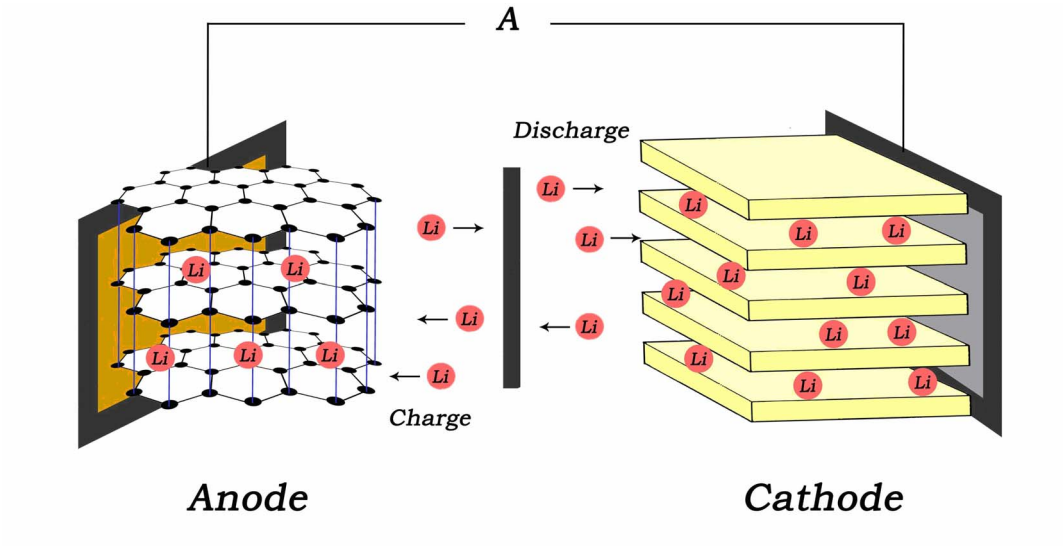

Fig.1.5: Schematic representation of a lithium-ion battery

At the surface of the anode, lithium ions react with electrons, allocated by the outer current path, to neutralize lithium ions, which are stored between anode layers. This process is called intercalation. During the discharge the inverse process occurs. Lithium atoms release an electron at the surface of the anode and are transported as ions through the electrolyte to the surface of the cathode. There, lithium ions react with electrons and are stored in the lattice of the cathode material.

Out of this principle representative chemical reactions for discharge can be expressed as follows:

Cathode: $Li_yCoO_2 + xLi^+ + xe^- \longrightarrow Li_{x+y}CoO_2$ Eq.(1.7.)

Anode: $Li_1C_6 \longrightarrow Li_{1-x}C_6 + xLi^+ + xe^-$ Eq.(1.8.)

Depending on their capacities, cathode and anode have different thicknesses inside the battery. Graphite anodes typically have a thickness of 60 µm while for example the $LiCoO_2$ cathode is 150 µm thick and separated by a 15 µm thick spacer from the anode. [3]

1.7. Materials and compounds for lithium-ion batteries

Lithium usually does not form one of the electrode masses itself. This enables many materials to be used as electrodes as long as they are able to intercalate lithium ions.

The goal for the energy storage industry is to create a cell with high voltage and high storage capacity. It would also be beneficial to assemble electrode materials with low variation in

potential during discharge, high reversibility in lithium storage, high stability of the active masses, high ionic conductivity and compliance with safety and environmental aspects. All these parameters drastically limit potential candidates. [3]

1.7.1. Li^+-intercalation compounds as electrode materials

An intercalation implicates the storage of free moving species in a host lattice without damaging it. Host lattices can appear as layers, tubes or cage-structures. The intercalation of anions is always connected to an oxidation of the host lattice, and cations with a reduction. Ionic mobility is high, when the host lattice is made of layers. The intercalation can be divided into three major steps. At first, solvated ions diffuse to the electrochemical double layer of the host lattice. Afterwards the ions loose their solvate in order to fit into free lattice positions in the host lattice and finally diffuse further inside the lattice. [4]

1.7.2. Anode materials

In anode materials lithium gets intercalated as ions instead of atoms. Hence the packing density of lithium alloys such as $Li_{22}Sn_5$ or LiAl can reach similar or even higher charge densities than lithium metal. Lithium alloys would be preferred as anode materials due to their high charge densities, however, suffer from drastic changes in structure and volume up to 400% and show low cycle stability.

Amorphous carbon is able to store reversibly 0.6 lithium atoms per 6 carbon atoms which corresponds to a capacity of 200 mAh/g. The potential strongly depends on the loading condition and varies therefore during discharging which yields a lower voltage.

Graphite is built up of hexagonal layers and is capable of intercalating 1 lithium per 6 carbon atoms in average.

$$C_6 + Li^+ + e^- \longrightarrow LiC_6 \qquad \text{(Eq.1.9.)}$$

Lithium ions are located in the Van-der-Waals cavities, involving a change in volume of about 10 % and leading to an excellent cycle stability of around 1000 cycles. The theoretical capacity for graphite is 372 mAh/g. Due to storage capacity and cost efficiency reasons graphitic carbons are favored over amorphous carbon and nowadays represent the standard material for anodes in lithium ion batteries. Although graphitic carbons show many advantages one serious problem persists. During the intercalation process, some Li^+ ions,

remain solvated, and intercalate as solvated species such as $Li_x(solv)_yC_n$, at the rims of the electrode, resulting in an increased volume of the edge of the electrode up to 200 % (see Figure 1.6). [3,4]

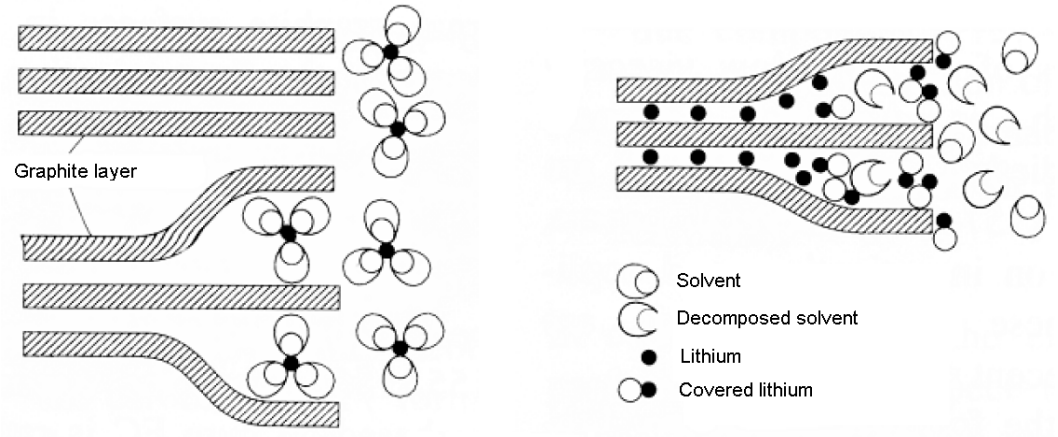

Fig.1.6: Left: Schematic depicture of solvated (e.g. $Li_x(solv)_yC_n$) lithium intercalation.

Right: Schematic depicture of desolvated (e.g. LiC_6) lithium intercalation

1.7.3. Cathode materials

Cathode materials provide lithium during charging and possess a high redoxpotential. The combination of graphitic carbon anodes with these materials afford high voltages. Most cathode materials have layered or spinel structure which enables the lithium ions to diffuse, respectively, in two or in three spatial directions. Most common layered materials have the theoretical composition $LiMO_2$, where M can be e.g. Co, Ni, Mn.

Nowadays lithium cobalt dioxide ($LiCoO_2$) is the most used cathode material because of its high voltage of 3.9 V against lithium and a capacity of about 150 mAh/g. The charging voltage is limited to 4.2 V since thermal decomposition of the material occurs when it exceeds 4.4 V. In the last few years the prices for cobalt increased, and consequently energy storage industries are searching for alternatives.

Potential alternatives are for example lithium nickel oxide ($LiNiO_2$) and lithium manganese oxide ($LiMn_2O_4$). Although the energy density of $LiNiO_2$ is higher than that of $LiCoO_2$, the lacking operational safety is the main drawback, which hinders its applicability in lithium ion batteries.

Concerning safety aspects, price and environmental compatibility, $LiMn_2O_4$ is probably the most promising electrode candidate. Lithium manganese oxide has a spinel structure and can

provide an average voltage of 4 V against lithium. Its temperature stability is quite good and the raw materials can be extracted easily. To stabilize the structure below 3.1 V the spinel structure has to be doped, but this doping limits the capacity to 110 mAh/g.

A recent development has been the introduction of a new material $Li(Ni_xCo_yMn_z)O_2$. The idea was to combine all positive characteristics of $LiCoO_2$, $LiNiO_2$ and $LiMn_2O_4$ and resulted in a new material with a voltage of 3.9 V and a capacity between 130-160 mAh/g, depending on the mixing ratio. [3,4,8]

1.7.4. Electrolyte

The main task of electrolytes is to transport lithium ions between the two electrodes during charging and discharging. In contrast to lead and nickel batteries, lithium-ion batteries use non-aqueous aprotic organic solvents, where lithium salts are dissolved. The electrochemical stability of organic solvents is much higher than aqueous solvents, which show electrolysis of water at a defined potential. This can lead to a critical increase in pressure inside the cell.

1.7.4.1. Non-aqueous electrolytes

Organic electrolytes consist of different components such as the liquid component which is a mixture of different solvents, a conducting salt which contains the lithium ions, and solid or liquid additives. The first requirement is that the electrolyte is electrochemically stable in the voltage range between 0 V and 4.5 V against lithium metal. Addition of the conducting salt is necessary to increase the conductivity of the organic liquid. To achieve an acceptable solubility of the conducting salt, large negatively charged counter ions are selected, resulting in the choice of salts such as $LiPF_6$, $LiBF_4$, $LiClO_4$ or $LiN(SO_2CF_3)_2$. The concentration of e.g. $LiPF_6$, which is the most commonly used salt, is about 1 mol/L. As higher salt concentrations increase the viscosity of the electrolyte, the conductivity is approximately limited to 10^{-2} S·cm^{-1}.

Typical liquid solvents for the electrolyte are ethylenecarbonate (EC), propylenecarbonate (PC), dimethylcarbonate (DMC), dimethoxyethan (DME) and diethylcarbonate (DEC). To compensate the high viscosity of the solvents and the dissolved conducting salt at lower temperatures, a second solvent being less viscous is added.

In order to vary the properties of the solid electrolyte interface, which is described in detail in chapter 2.3.5., further solid or liquid supplements are added. Liquid components such as

vinylidencarbonate (VC) are widely used, and solid additives like SiO_2 and Al_2O_3 prevent the contamination of the electrolyte by e.g. water. Beside low ionic conducting properties, higher costs and higher risk of combustion are severe disadvantages of nonaqueous electrolytes. [3,4,5]

1.7.4.2. Polymer and gel electrolytes

Electrolytes can be prepared under the form of polymeric films which do not undergo electrochemical reactions. The main advantages of polymer electrolytes consist of a reduced cell volume and prevention of leakage, as no liquid electrolyte is present any longer. The conducting salt is positioned in long-chain solid polyethylenoxide (PEO). However the ion conductivity at room temperature is too low for industrial applications.

Nowadays interest focuses on a subunit of polymer electrolytes called gel electrolytes, which are liquid organic electrolytes within a polymer matrix system like polyvinylidenfluorid (PVDF) or polyacrylnitril (PAN). The ion conductivities of $10^{-2} – 10^{-3}$ $S \cdot cm^{-1}$ are acceptable. [3,4,5,8]

1.7.5. Solid electrolyte interface film formation

At the interfaces between the electrodes and the electrolyte a solid layer called “solid electrolyte interface – (SEI)” forms. This layer is electrically insulating, but permeable for Li^+ ions and consists of electrolyte decomposition products. The SEI protects the electrode surface from corrosive electrolyte solutions. A variation of the electrolyte composition and addition of different substances allows a control of the thickness and the permeability for Li^+ of the SEI film.

Contrary to the spontaneous formation of the SEI at the interface between lithium metal and electrolyte, in case of a carbon electrode, the layer appears in situ at the very first charging at the surface of the anode. The corresponding irreversible loss of material and charge has to be considered for the cell construction. These films have to disaggregate lithium ions from solvent molecules, so that no solvated Li can get intercalated into the graphite structure, which would damage the electrode. The self-discharge, and thus the aging of the battery, are closely linked with the formation of SEI. [3, 4,5,11]

1.7.6. Current collectors and separator

Current collectors are thin foils, which enable electron transport to and from the electrodes. Copper having a thickness of at least 10 µm is mainly used for the anode. Copper is stable in the potential area of the anode and is inert towards lithium or constituents of the electrolyte. Aluminium is the first choice for the positive electrode. It has the same qualities as copper for the anode and is produced in thicknesses of 15 µm.

The separator is a mechanically stable electrical insulator. This protective layer is placed between the electrodes to avoid short circuit. It consists of a material which has to have long-term stability against reduction, oxidation and organic solvents. The thickness, which is actually 20-25 µm, should be as low as possible, and the separator should not influence the internal resistance of the cell. Often the separator consists of a highly porous plastic foil like polyethylene or polypropylene. The porosity is approximately 50 % of the volume and is saturated with electrolyte. [3]

1.8. Properties and applications of lithium ion batteries

The high cell voltage of 3.6 V for the currently used cells allows the production of batteries with fewer cells. During discharge the voltage curve shows a smooth declining devolution (see Figure 1.7.).

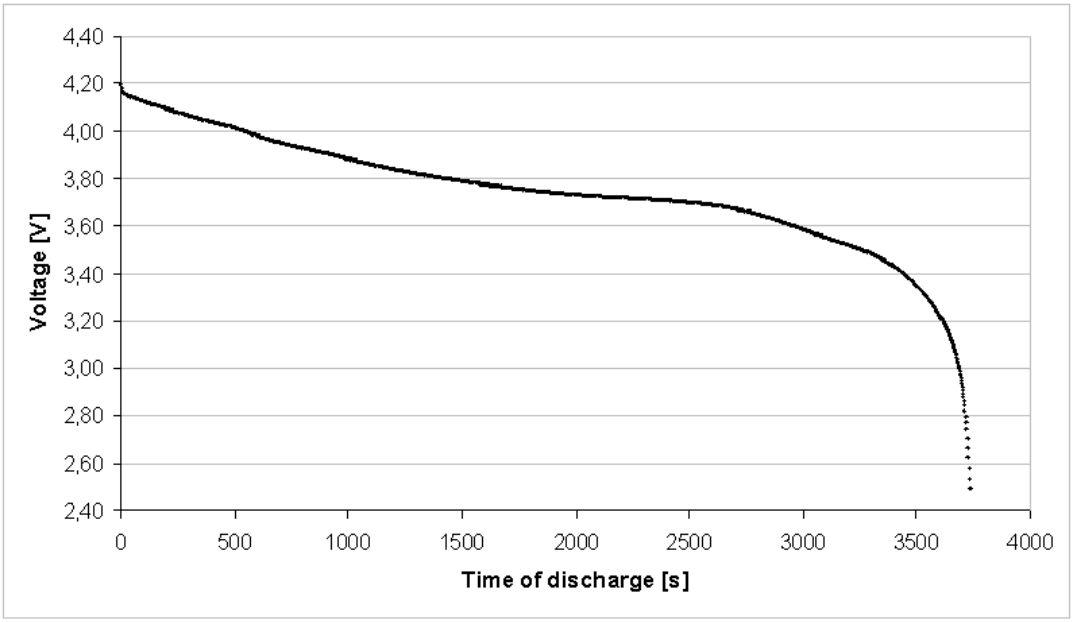

Fig.1.7. Voltage curve at discharge of a pouch cell at a discharge rate of 1C

It is possible to calculate the voltage curve for an intercalation with the following formula:

$$E(x) = E_0 + E_F - \frac{RT}{zF} \ln\left(\frac{x}{1-x}\right) \qquad \text{Eq.(1.10.)}$$

where E_0 is the ground potential in V, E_F the Fermi energy in eV, R the ideal gas constant in $J \cdot K^{-1} \cdot mol^{-1}$, T the temperature in K, z the charge number, F the Faraday constant in $C \cdot mol^{-1}$ and x is the mass of active species, which is in our case the lithium atoms.

The voltage of lithium ion batteries ranges from 4.2 V which equals the fully charged state to and 2.7 V, corresponding to the final discharge voltage.

Current lithium ion battery systems exhibit a high specific energy density (150-250 Wh/kg), which predestines them to be used in a wide range of applications. Batteries in the lower range are used for consumer electronic devices like photo cameras, toys or mobile phones, while batteries with high energy densities are applied in prototypes of electric vehicles and aerospace applications. Another big advantage is the low self-discharge at room temperature which is about 3 % per month. Lithium ion batteries will lead the global marked due to their low weight, fast charging times and lack of memory effects. [3]

1.9. Construction types and safety of lithium ion batteries

Lithium ion batteries are available in three different construction types:

- Cylindrical cells
- Prismatic cells
- Flat plate constructions also called “Pouch-type or coffee bag” cells

The most widely spread type of cell is the cylindrical cell, as it exhibits the highest energy density, is easy to produce and is mechanically very stable. The electrodes, the separator with electrolyte and the current collectors are layered as shown in Figure 1.8. This stack is spiral-wrapped for packing.

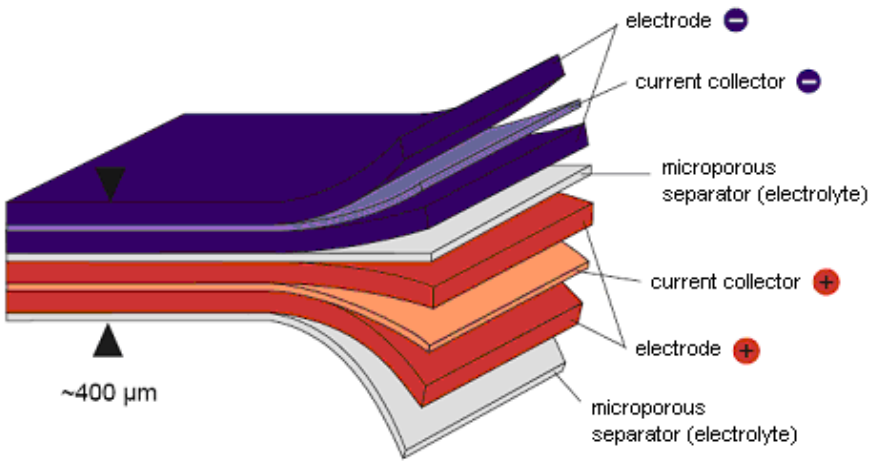

Fig.1.8: Arrangement of different components of the lithium ion battery before wrapping

As the electrodes are coated with current collectors on both sides it is necessary to insert a further separation layer at the outer side of the anode to avoid contact with the cathode of the next layer when the layer assembly is wrapped. This wrapped cell core is brought into the cell case, which maintains pressure and compression to provide a good contact between the different parts of the cell. Figure 1.9 shows the arrangement inside the cell case.

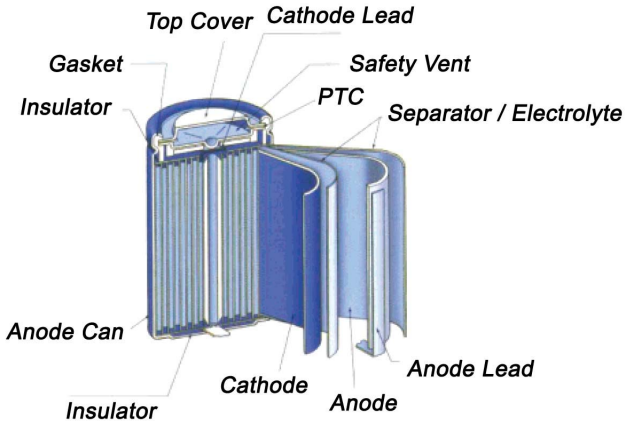

Fig.1.9: Assembling of a cylindrical lithium ion battery

One electrode is welded to the bottom of the cell, creating the first pole, the other electrode with the top, which gives the second pole. Beyond this pole a safety device, the so called positive temperature coefficient (PTC) element, is located. In case of a breakdown and exothermic reaction, it changes it resistance at a defined temperature and interrupts the current flow in order to stop further heating of the cell.

Prismatic cells can be produced either as layers or as wrapped cells. Prismatic cells were developed for applications where cylindrical cells could not be accommodated, which means

that it is not a standard size but constructed on consumer's request. Due to the shape of the cell, the pressure inside is lower than in cylindrical cells, which influences lifetime and aging. The parts of a prismatic cell are shown in Figure 1.10(a). As already mentioned, it is possible to build prismatic cells with a layer technique as depicted in Figure 1.10(b), although this technique is more suitable for polymer cells.

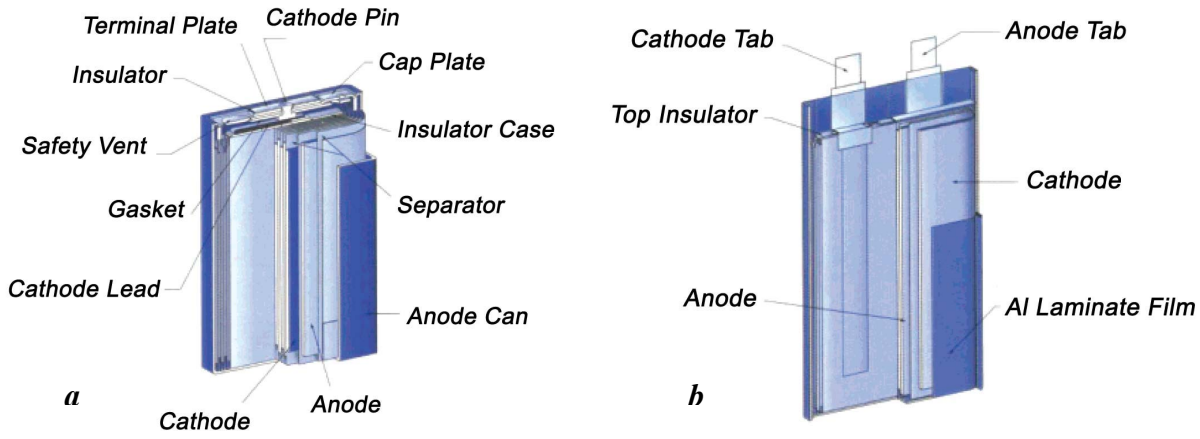

Fig.1.10: Assembling of a prismatic cell (a) and a "coffee bag" cell (b)

Layers in polymer cells are stuck together by cohesive forces, caused by the structure of the electrolyte. The name coffee bag cell belongs to the Al-foil packaging of the cell which resembles a coffee bag. The Al-foil is plastic-laminated and protects the cell from gas diffusion.

Besides the already mentioned PTC device, lithium ion batteries contain additional safety systems. The electrodes are designed to store all lithium atoms in the system. Metallic lithium must not be in the cell, as it could cause uncontrolled dendritic growth. Doped active masses increase their electrochemical stability, especially at higher voltage. In case of excess pressure, due to gas formation, a safety vent opens. The separator melts at a certain temperature and blocks the reaction inside the cell. [2,3,8]

1.10. Solid electrolytes in lithium ion batteries

Another safety precaution, which was not mentioned in the previous chapter, would be the replacement of liquid electrolytes by solid electrolytes.
Using solid electrolytes provides several advantages. The most important aims, which can be reached by using solid electrolytes, will be:

- No leakage of liquid electrolyte
- Higher stability of the total arrangement
- Higher chemical stability against electrode materials
- No hazard of combustibility and thus explosion of the cell
- Possibility of higher temperature exposure

Recently fast lithium ion conducting solids have been identified as potential electrolytes in all-solid-state rechargeable batteries and also in other solid-state electrochemical devices [26]. Replacing the liquid or polymer electrolyte with a solid would lead to simplification of the cell design as well as an improvement of safety and durability [21].

1.10.1. Ionic conduction in solids:

In the same way electrons, ions can act as charge carriers, as they are always present in crystalline materials such as oxides. The electrical conductivity σ_i resulting from migrating ions is dependant on the number n_i, the charge $z_i e$, and the mobility μ_i of the charge carriers and can be developed out of equation 1.11.

$$\sigma_i = n_i z_i e \mu_i \qquad \text{Eq.(1.11.)}$$

Ions moving through the lattice by the influence of an electric field must exhibit a certain thermal energy in order to overcome the energy barrier ΔG for hopping to another lattice site. The ion mobility μ can be expressed as:

$$\mu_i = \frac{e z_i a^2 \nu}{kT} e^{\frac{-\Delta G}{kT}} \qquad \text{Eq.(1.12.)}$$

where a is the jump distance to be overcome, ν is the lattice vibrational frequency and ΔG is the Gibbs free energy, which is also called activation energy for ionic motion.
The absolute mobility B_i of the charge carriers is given by the Nernst-Einstein relationship (see Equation 1.13.) where D_i is the diffusion coefficient:

$$B_i = \frac{a^2 \nu}{kT} e^{\frac{-\Delta G}{kT}} = \frac{D_i}{kT} \qquad \text{Eq.(1.13.)}$$

Therefore the ionic conductivity is expressed as:

$$\sigma_i = \frac{n_i z_i^2 e^2 D_i}{kT} \qquad \text{Eq.(1.14.)}$$

Depending on the material, the total conductivity can be composed of several different terms, which behave additively. The main contributions are the conductivity of the bulk material σ_b and the grain boundaries σ_{gb}, which leads to:

$$\sigma_i = \sigma_b + \sigma_{gb} \qquad \text{Eq.(1.15.)}$$

The ionic conductivity is expressed as a function of the energy barrier, which is the activation energy in the so called Arrhenius plot:

$$\sigma T = A e^{\frac{-Ea}{kT}} \qquad \text{Eq.(1.16.)}$$

where A is the pre-exponential factor, T is the absolute temperature and k is the Boltzmann constant. [6]

1.11. Lithium ion conducting substances – requirements and limitations:

Lithium ion conductivity has been reported for a lot of crystalline materials. Due to chemical and mechanical stability, oxide materials are preferred to non-oxide materials. [26] Appropriate lithium-ion conductors should have the following properties [28]:

- High lithium conductivity within the working temperature range
- Negligible electronic conductivity within the used voltage range
- Small grain boundary resistance
- Electrochemical decomposition voltage > 5.5 V against lithium
- Electrochemical stability against the electrode materials and humidity
- Environmental compatibility
- Low cost and easy production

Especially crystalline and amorphous metal oxides and halides show lithium ion conduction, but most of them are not compatible for current battery systems, due to various limiting factors [12]. Most of the explored lithium-ion conductors either show high ionic conductivity

or high chemical stability. $Li_{3x}La_{(2/3)-x}\square_{(1/3)2-x}TiO_3$ [(1)] ($(Li,La)TiO_3$) for example is a very good Li^+ conductor and exhibits a bulk conductivity of 10^{-3} S·cm^{-1} at 27 °C. At higher lithium activities given by the electrodes $(Li,La)TiO_3$ becomes mainly electronically conducting. [19] Additionally $(Li,La)TiO_3$ shows a large grain boundary resistance and Ti^{4+} gets reduced to Ti^{3+} as it is unstable against Li-metal. [28] Other good lithium ion conducting materials are:

- Li_3N, which decomposes at low voltages around 0.445 V at room temperature
- $Li_{14}ZnGe_4O_{16}$, which is highly reactive towards CO_2 and metallic lithium
- $Li_{1,3}Ti_{1,7}Al_{0,3}(PO_4)_3$, which is unstable against Li-metal and suffers from reduction of titanium as $(Li,La)TiO_3$
- Li-β-alumina, which is not thermodynamically stable and highly hygroscopic.

On the other hand $Li_{2,88}PO_{3,86}N_{0,14}$ and Li_9AlSiO_8 would be very stable against electrode materials and have high decomposition voltages, but exhibit low ionic conductivity. [28]
A few crystalline and amorphous substances showing both, high conductivity together with chemical stability are known. Searching for new solid state ion conductors led to the investigation of substances with compounds similar to $(Li,La)TiO_3$ but without reducible titanium. [31]
Recently lithium containing synthetic garnet-like materials, which are derivatives related to natural ideal garnets, have been identified as favorable candidates for solid state electrolytes in all-solid-state rechargeable batteries. [29]

1.12. Atom positions and arrangements in garnet and garnet-like materials

1.12.1. The Ideal Garnet structure

Garnets are cubic minerals of the space group $Ia\bar{3}d$ with the general structure $A_3^{II}B_2^{III}(SiO_4)_3$ (see Figure 1.11) where A and B stand for different cations on different positions. Position A can be occupied by e.g. Mg^{2+}, Fe^{2+}, Mn^{2+}, Ca^{2+}. Position B can be occupied by e.g. Al^{3+}, Cr^{3+}, Fe^{3+}.

(1) □ represents a vacancy, 0<x<0.16

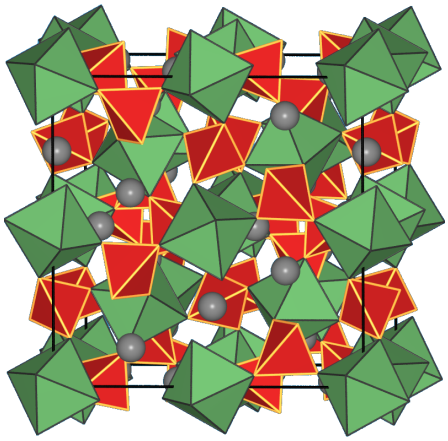

Fig.1.11: Structure model of a natural garnet (red: SiO_4-tetrahedra, green: BO_6-octahedra, grey: A^{2+} ions in pseudo-dodecahedral surrounding)

Garnets have a three-dimensional network of oxide-polyhedra, sharing faces and edges (see Figure 1.15, Chapter 1.15), and belong to the group of neosilicates, where SiO_4-tetrahedra are connected on all corners with BO_6-octahedra and vice versa. A atoms are located in between on pseudo-dodecahedral positions. [12]

1.12.2. General atom positions in garnet-like materials

Garnet-like materials can have an excess of lithium ions ($n_{Li} > 3$), where n_{Li} is the number of lithium atoms per formula unit, depending on the constituting elements, compared to the ideal lithium garnet composition ($n_{Li} = 3$). [37] Oxygen anions are located at general positions in the cell, forming octahedral dodecahedra, tetrahedra and prisms. [29] Lanthanum, and lanthanum substituents (K, Mg, Ca, Sr, Ba), occupy the eight-coordinated crystallographic sites. The high symmetry octahedral site, conventionally occupied in the ideal garnet structure, is fully occupied in the garnet-like structure by zirconium, tantalum or niobium, antimony or bismuth. [29,37]

1.12.3. Lithium coordination in garnet-like materials

On closer examination of the structure, especially of the $[La_3Ta_2O_{12}]^{5-}$ framework (see Figure 1.12.) it can be seen that lithium ions might occupy three different positions, which are octahedral, tetrahedral and prismatic coordinated sites.

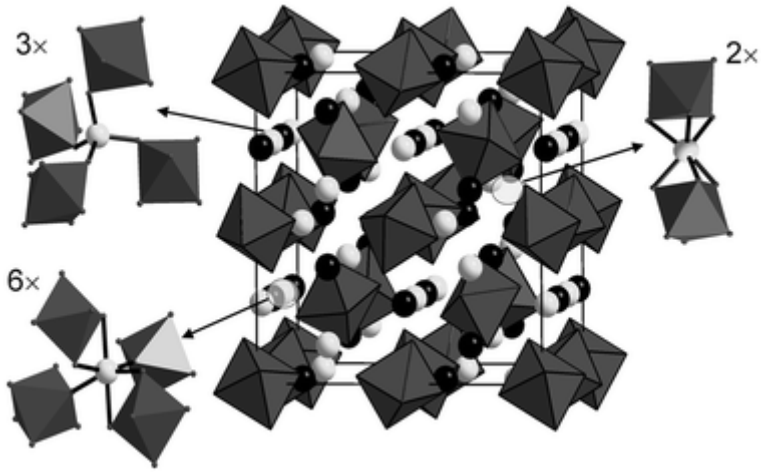

Fig.1.12: Crystal structure of a garnet and suitable lithium positions in $Li_5La_3Ta_2O_{12}$ *: six octahedral, three tetrahedral and two prismatic sites per formula unit.*

In garnets tetrahedral sites are occupied by Li and investigation of bond valence sums approaches showed that lithium occupies the octahedral sites rather than prismatic and tetrahedral ones. In contrary neutron diffraction experiments proved that lithium is found in the center of tetrahedral sites as well as in distorted oxide octahedra. If a neighboring tetrahedral site is occupied, a displacement of lithium atoms in the octahedra occurs which results in a reduction of electrostatic repulsion between the two lithium atoms.

By increasing the lithium content to six atoms in the structure, a continuous increase of vacancies at the tetrahedral sites together with a higher population on octahedral sites, can be detected.

In compositions as $Li_7La_3Zr_2O_{12}$, having 7 lithium atoms per formula unit, Li is distributed throughout tetrahedral and octahedral sites. $\frac{1}{3}$ of the tetrahedral sites and all octahedral sites are occupied. [45]

1.13. Properties and ionic conductivity in garnet-like materials

1.13.1. $Li_5La_3M_2O_{12}$ $(M = Ta, Nb)$

A new class of fast lithium ion conducting materials having the chemical composition $Li_5La_3M_2O_{12}$ $(M = Ta, Nb)$ was found to crystallize in the symmetry group $Ia\bar{3}d$ of the cubic system. [28]

The starting materials of all published structure are metal oxides, metal carbonates, nitrates or hydroxides. The raw materials are mixed in a stoichiometric ratio and 10 wt% excess Li_2CO_3 is added to compensate the loss of lithium during temperature treatment. In addition M_2O_5 $(M = Ta, Nb)$ is used for the preparation. The calcination temperature is 700 °C with 14 hours dwell, while the sintering temperature ranges between 900 °C and 1050 °C with 12 – 24 hours dwell. [28,35,41]

$Li_5La_3Ta_2O_{12}$ possessing the space group $Ia\bar{3}d$ was found to have a lattice parameter between $a = 12.804$ Å [28] and $a = 12.823(2)$ Å [33] depending on the sintering temperature [35], while the niobium compound has a lattice parameter between $a = 12.797$ Å [28] and $a = 12.889(3)$ Å [33]. Both $Li_5La_3M_2O_{12}$ compounds exhibit a similar lithium ion conductivity of the order of magnitude of about 10^{-6} S/cm at room temperature [28,43]. With an activation energy for the conductivity of $E_A = 0.43\,eV$ for $Li_5La_3Ta_2O_{12}$, this compound is of great interest for the application as electrolyte material, compared to $Li_5La_3Nb_2O_{12}$ possessing an activation energy $E_A = 0.56\,eV$.

There are two theories of lithium occupations for this structure. Thangadurai et al. [43] proposed that Li is located in the octahedral sites only, while tetrahedral sites are empty. In contrast, Cussen [32] announced for the space group $Ia\bar{3}d$ that lithium ions are occupying tetrahedral as well as distorted octahedral sites. A more detailed examination will be described later on. [24]

1.13.1.1. $Li_5Ln_3M_2O_{12}$ $(M = Ta, Nb;$ $Ln =$ La or rare earths) derivates:

$Li_3Nd_3Te_2O_{12}$, $Li_5Nd_3Sb_2O_{12}$, $Li_5La_3Sb_2O_{12}$, $Li_5La_3Bi_2O_{12}$

By replacing pentavalent tantalum or niobium in $Li_5Ln_3M_2O_{12}$ by hexavalent tellurium, or by antimony or bismuth, and lanthanum by yttrium, praseodymium, neodymium or samarium respectively, the content of lithium ions within the structure can be varied. In $Li_3Nd_3Te_2O_{12}$, which exhibits a very poor ionic conductivity of $\sigma_t = 10^{-5}\ S \cdot cm^{-1}$ at 600 °C and an activation energy of $E_A = 1.2\,eV$, all three lithium ions are occupying tetrahedral sites. [36,41]

$Li_5Nd_3Sb_2O_{12}$ also crystallizes as cubic structure ($Ia\bar{3}d$) with a lattice constant of $a = 12.66238(3)$ Å, which is smaller than for $Li_5La_3M_2O_{12}$ $(M = Ta, Nb)$, in coherence with the smaller ionic radius of tellurium compared to tantalum or niobium. [38]

Replacing tantalum in $Li_5La_3Ta_2O_{12}$ by antimony, the cubic ($Ia\bar{3}d$) substance $Li_5La_3Sb_2O_{12}$ is created with a lattice constant of $a = 12.8566(18)$ Å, an ionic conductivity of $\sigma_t = 7.8 \cdot 10^{-6}\ S \cdot cm^{-1}$ at room temperature and an activation energy of $E_A = 0.51 eV$. [26]

A new garnet-related structure having the chemical composition $Li_5La_3Bi_2O_{12}$ was reported recently. On the one hand, with $a = 13.0652(4)$ Å the lattice parameter of $Li_5La_3Bi_2O_{12}$ is quite high compared to other compositions. On the other hand, calcination and sintering temperature being 675 °C (6 hours dwell) and respectively 750 °C (48 hours dwell), are relatively low. This substance exhibits a total conductivity of $\sigma_t = 1.9 \cdot 10^{-5}\ S \cdot cm^{-1}$, measured at room temperature in argon, and an activation energy of $E_A = 0.47 eV$. [30]

1.13.2. $Li_6ALa_2M_2O_{12}$ ($A = Mg, Ca, Sr, Ba$ and $M = Ta, Nb$)

It is also possible to vary the amount of lithium ions within the structure by the partial replacement of trivalent lanthanum by divalent alkaline earth ions, which yields a novel series of cubic garnet compounds with the general formula $Li_{5+x}A_xLa_{3-x}M_2O_{12}$ ($A = Mg, Ca, Sr, Ba$ and $M = Ta, Nb$). [27,28]

The mixed raw materials are calcined and subsequently sintered within an alumina crucible. Before and after the first step, the material is milled with zirconia balls for 12 hours. [17,20,33,36,37,40] For sintering, the powder is pressed under isostatic pressure into a pellet and positioned into a powder bed consisting of mother substance in order to reduce lithium evaporation at elevated temperatures.

1.13.2.1. $Li_6ALa_2M_2O_{12}$ ($A = Mg, Ca$ and $M = Ta, Nb$)

The lattice constants of magnesium and calcium doped $Li_5La_3M_2O_{12}$ decrease because of their smaller ionic radius taking into account the ionic radii of eight-coordinated elements, which are $r_{Mg^{2+}} = 0.86$ Å for magnesium and $r_{Ca^{2+}} = 1.12$ Å for calcium compared to the larger ionic radius of lanthanum $r_{La^{3+}} = 1.18$ Å.

$Li_6MgLa_2Ta_2O_{12}$, $Li_6CaLa_2Ta_2O_{12}$ and $Li_6CaLa_2Nb_2O_{12}$ have lattice parameters of $a = 12.794(1)$ Å, $a = 12.719(1)$ Å and $a = 12.697(2)$ Å respectively for samples sintered at 900 °C. The lattice constants for pellets sintered at 950 °C are slightly higher. Considering the

lithium ion conductivities and activation energies, the magnesium compound exhibits a total conductivity of $\sigma_t = 2.03 \cdot 10^{-6}\, S \cdot cm^{-1}$ measured at room temperature and an activation energy of $E_A = 0.51 eV$, the calcium tantalum and the calcium niobium compounds show $\sigma_t = 2.61 \cdot 10^{-6}\, S \cdot cm^{-1}$ measured at room temperature and $E_A = 0.54 eV$, and $\sigma_t = 1.6 \cdot 10^{-6}\, S \cdot cm^{-1}$ measured at 50 °C and $E_A = 0.55 eV$ respectively. [20,37]

1.13.2.2. $Li_6 ALa_2 M_2 O_{12}$ (A = Sr, Ba and M = Ta, Nb)

With increasing ionic radius of the alkaline earth ions, $r_{Sr^{2+}} = 1.25$ Å and $r_{Ba^{2+}} = 1.42$ Å compared to $r_{La^{3+}} = 1.18$ Å, the lattice parameter increases. The substances and their properties are listed in the following Table 1.1.

The data from Table 1.1. show that there is a correlation between sintering temperature and compound properties. In Figure 1.13. it can be seen that with increasing sintering temperature the conductivity is increasing.

	Ionic radius	Lattice parameter	$\sigma_{bulk,\ total}$	Activation Energy	σ (T_{sint}) 900→950°C
Ba	↑	↑	↑	↓	↓
$Sr_{0.5}Ba_{0.5}$					↑
Sr				↓	
Ca		↑			
Mg	↑		↑		↓

Fig.1.13: Schematic representation of the relationship between the lattice parameter, increase in sintering temperature (T_{sint}), bulk and total conductivity ($\sigma_{bulk,total}$) for the various alkaline earth elements substituting one La atom in the garnet-like compound $Li_5La_3Ta_2O_{12}$. The Mg substituted compound is not following the systematic dependence because of the formation of additional phases.

With increasing radius a decrease in activation energy and an expansion of the lattice parameter takes place. [16] Furthermore it is interesting, that for alkaline earth ion substituted materials, grain boundary contribution is just a very low percentage of the total conductivity compared to pure $Li_5La_3M_2O_{12}$ $(M = Ta, Nb)$. [27,37]

Line	Compound*	Sintering temperature [°C]	Lattice parameter [Å]	Total conductivity [S/cm] (°C)[2]	Activation energy [eV]	Reference
1	$Li_6SrLa_2Ta_2O_{12}$	900	12.808(2)	$7.00 \cdot 10^{-6}$ (22)	0.50	33
2	$Li_6SrLa_2Ta_2O_{12}$	900	12.82(6)	$9.33 \cdot 10^{-6}$ (33)	0.45	20
3	$Li_6SrLa_2Ta_2O_{12}$	950	12.83(0)	$1.18 \cdot 10^{-5}$ (33)	0.45	20
4	$Li_6Sr_{0,5}Ba_{0,5}La_2Ta_2O_{12}$	900	12.87(6)	$5.21 \cdot 10^{-6}$ (33)	0.44	20
5	$Li_6Sr_{0,5}Ba_{0,5}La_2Ta_2O_{12}$	950	12.86(0)	$6.62 \cdot 10^{-6}$ (22)	0.44	20
6	$Li_6SrLa_2Nb_2O_{12}$	900	12.811(1)	$4.20 \cdot 10^{-6}$ (22)	0.50	27/37
7	$Li_6SrLa_2Ta_2O_{12}$	900	12.8575(2)	$7.00 \cdot 10^{-6}$ (22)	0.50	29
8	$Li_{6,4}Sr_{1,4}La_{1,6}Ta_2O_{12}$	900	12.87(0)			29
9	$Li_6BaLa_2Ta_2O_{12}$	900	12.946(3)	$4.00 \cdot 10^{-5}$ (22)	0.40	33
10	$Li_6BaLa_2Ta_2O_{12}$	900	12.97(5)	$1.78 \cdot 10^{-5}$ (17)	0.42	20
11	$Li_6BaLa_2Ta_2O_{12}$	950	12.97(6)	$1.22 \cdot 10^{-5}$ (17)	0.42	20
12	$Li_6BaLa_2Nb_2O_{12}$	900	12.868(1)	$6.00 \cdot 10^{-6}$ (22)	0.44	27/37
13	$Li_5BaLa_2Ta_2O_{11,5}$	900	12.89(1)	$4.90 \cdot 10^{-6}$ (50)	0.52	19
14	$Li_{5,5}BaLa_2Ta_2O_{11,75}$	900	12.93(7)	$3.10 \cdot 10^{-5}$ (50)	0.47	19
15	$Li_{5,75}BaLa_2Ta_2O_{11,875}$	900	12.96(2)	$9.00 \cdot 10^{-5}$ (50)	0.44	19
16	$Li_6BaLa_2Ta_2O_{12}$	900	12.97(5)	$1.51 \cdot 10^{-4}$ (50)	0.42	19
17	$Li_{6,25}BaLa_2Ta_2O_{12,125}$	900	12.96(1)	$1.46 \cdot 10^{-4}$ (50)	0.42	19
18	$Li_{6,5}BaLa_2Ta_2O_{12,25}$	900	12.95(6)	$1.04 \cdot 10^{-4}$ (50)	0.42	19
19	$Li_{6,75}BaLa_2Ta_2O_{12,375}$	900	12.94(8)	$1.05 \cdot 10^{-4}$ (50)	0.42	19
20	$Li_7BaLa_2Ta_2O_{12,5}$	900	12.94(7)	$9.70 \cdot 10^{-5}$ (50)	0.45	19
21	$Li_{5,25}Ba_{0,25}La_{2,75}Ta_2O_{12}$	900	12.84(2)	$7 \cdot 10^{-6}$ (33)	0.48	36
22	$Li_{5,5}Ba_{0,5}La_{2,5}Ta_2O_{12}$	900	12.86(5)	$1.9 \cdot 10^{-5}$ (33)	0.46	36
23	$Li_6BaLa_2Ta_2O_{12}$	900	12.97(5)	$5 \cdot 10^{-5}$ (33)	0.42	36
24	$Li_{6,25}Ba_{1,25}La_{1,75}Ta_2O_{12}$	900	12.98(2)	$7 \cdot 10^{-5}$ (33)	0.40	36
25	$Li_{6,5}Ba_{1,5}La_{1,5}Ta_2O_{12}$	900	12.98(0)	$5 \cdot 10^{-5}$ (33)	0.40	36
26	$Li_{6,75}Ba_{1,75}La_{1,25}Ta_2O_{12}$	900	12.978	$1.5 \cdot 10^{-5}$ (33)	0.42	36
27	$Li_7Ba_2LaTa_2O_{12}$	900	12.96(0)	$5 \cdot 10^{-6}$ (33)	0.44	36
28	$Li_{6,5}Ba_{0,5}La_{2,5}ZrTaO_{12}$	1100	12.783(4)	$2.00 \cdot 10^{-4}$ (23)	0.31	20
29	$Li_{6,5}Ba_{0,5}La_{2,5}ZrNbO_{12}$	1100	12.815(4)	10^{-5} (23)		20

*Table 1.1.: Strontium and barium doped compounds (*all substances having space group $Ia\bar{3}d$)*

[2]measuring temperature for ionic conductivity

Another series of compounds, $Li_{5+x}Sr_xLa_{3-x}Nb_2O_{12}$ $(x = 0;\ 0.25;\ 0.5;\ 0.75;\ 1.0;\ 1.25)$, which is not listed in the table was reported possessing the space group $Ia\bar{3}d$ and exhibiting similar lithium ion conductivity and activation energy. Within this series the highest conductivity was $\sigma_t = 5.51 \cdot 10^{-5}\, S/cm$ for the composition at $x = 1.0$ corresponding to $Li_6SrLa_2Nb_2O_{12}$. The appearance of secondary phases was reported for x-values larger than 1.25. [34]

Compounds mentioned in the 13-20 of table 3.1. belong to a series having the general formula $Li_{5+x}BaLa_2Ta_2O_{11.5+0.5x}$ $(x = 0-2)$. The bulk ionic conductivity increases with increasing values for x, reaching a maximum at $x = 1.25$, the maximum for the total ionic conductivity is mentioned for $x = 1.0$, which is established due to an optimum ratio of lithium ions and vacancies [17].

The lines 21-27 of Table 1.1. correspond to the series $Li_{5+x}Ba_xLa_{3-x}Ta_2O_{12}$ $(x = 0-2)$. XRD patterns show the presence of a secondary phase in addition to the main garnet-like phase for x-values larger than 1.5. Considering the data from Table 1.1. it can be seen that the conductivity increases with increasing barium content, exhibiting a maximum at $x = 1.25$ and then decreases with further increase in the barium content.

Among all reported materials it is mentioned that strontium and barium, together with lanthanum, are occupying eight-coordinated crystallographic sites in a random distribution. The octahedral site is conventionally filled with tantalum or zirconium respectively. Depending on the amount of lithium within the structure, Li is located at the tetrahedral and at highly distorted octahedral sites. [29]

1.13.2.2.1. $Li_{5,5}K_{0,25}La_{2,75}Nb_2O_{12}$ and $Li_6ALa_2M_2O_{12}$ $(A = Sr\ and\ M = Ta, Nb)$ derivates:

$Li_6SrLa_2Sb_2O_{12}$ and $Li_6SrLa_2Bi_2O_{12}$

For the preparation of $Li_{5,5}K_{0,25}La_{2,75}Nb_2O_{12}$, where trivalent lanthanum is partially replaced by monovalent potassium, KNO_3 was used with an excess of 10 wt% to compensate the loss of potassium during temperature treatment. For a sintered pellet at 1000 °C the total conductivity at 50°C is around $\sigma_t = 6.0 \cdot 10^{-5}\, S/cm$ and the activation energy is $E_A = 0.49\, eV$. Although the ionic radius of potassium is $r_{K^+} = 1.33$ Å the lattice constant is rather small $a = 12.7937(8)$ Å. [26,35]

Lately, two new compounds possessing garnet-like structure, i.e. $Li_6SrLa_2Sb_2O_{12}$ and $Li_6SrLa_2Bi_2O_{12}$ have been investigated. The sintering temperature for the bismuth compound is slightly lower than for the antimony-containing compound. However their electrical properties are quite different. The strontium doped samples exhibit a total conductivity of $\sigma_t = 6.3 \cdot 10^{-6} S \cdot cm^{-1}$, measured at 24 °C in argon, and an activation energy of $E_A = 0.54eV$ for the antimony and $\sigma_t = 2.0 \cdot 10^{-5} S \cdot cm^{-1}$ (measured at 22 °C in argon), $E_A = 0.42eV$ for the bismuth containing material, which correlates to the much larger lattice parameter of $Li_6SrLa_2Bi_2O_{12}$ $a = 13.0893(9)$ Å, where ionic conductivity can be accomplished probably more easily, compared to $a = 12.8933(3)$ Å for $Li_6SrLa_2Sb_2O_{12}$. [26,30]

1.13.3. $Li_7La_3Zr_2O_{12}$

Lately $Li_7La_3Zr_2O_{12}$ was reported to be a fast lithium ion conductor and to possess a garnet-like structure. Thermal and chemical stability, environmental compatibility as well as low costs and ease of preparation suggest that this garnet-type material has overcome existing problems for solid-state electrolytes.

Polycrystalline $Li_7La_3Zr_2O_{12}$ is prepared by a simple solid-state reaction. Before and after each heat treatment at 900 °C and 1125 °C the mixed powders are ball-milled with zirconia balls in 2-propanol. The heat treatments are performed in an alumina crucible for 5 hours. After calcination the powder is pressed under isostatic pressure into pellets and sintered at 1230 °C for 36 hours covered by a powder bed out of mother substance.

$Li_7La_3Zr_2O_{12}$ can appear in two stable conformations having a lattice constant of $a = 12.9682(6)$ Å for cubic ($Ia\bar{3}d$) symmetry and $a = 13.134(4)$ Å and $c = 12.663(8)$ Å for tetragonal ($I4_1/acd$) symmetry. The cubic material exhibits a bulk conductivity of $\sigma_b = 5.11 \cdot 10^{-4} S \cdot cm^{-1}$, a total conductivity of $\sigma_t = 7.74 \cdot 10^{-5} S \cdot cm^{-1}$ at room temperature and an activation energy of $E_A = 0.32eV$, while the tetragonal material shows a bulk and total conductivity of $\sigma_b = 1.63 \cdot 10^{-6} S \cdot cm^{-1}$ and $\sigma_t = 2.19 \cdot 10^{-6} S \cdot cm^{-1}$ respectively and an activation energy of $E_A = 0.54eV$.

Lithium atoms in the tetragonal conformation can be positioned in three types of atomic sites occupying a tetrahedral and two types of octahedral sites. The octahedral sites are vacant in the ideal garnet. [19,22]

1.13.4. Aluminum doped $Li_7La_3Zr_2O_{12}$

In addition to the mentioned raw materials in chapter 1.13.1. $\gamma - Al_2O_3$ is used for the preparation. $\gamma - Al_2O_3$ is added in concentrations between 0,1 wt% and 2 wt%. The mixed raw materials are calcined at 900 °C for 6 hours and afterwards sintered at 1000 °C for another 36 hours. The lithium ion conductivity is around $\sigma_t = 1 \cdot 10^{-4} S/cm$. Activation energies as well as lattice parameters are not specified. [44]

1.14. Structure models for garnet-like materials

In 1988 Mazza [46] determined the structure of $Li_5La_3M_2O_{12}$ $(M = Nb, Ta)$ from powder XRD data and proposed the crystal structure $Ia\bar{3}d$ to be closely related to the natural garnet structure. According to that proposal, three of the Li atoms are positioned on the tetrahedral coordinated site, while the remaining two Li occupy octahedral positions. In the same year Hyooma and Hayashi [47] suggested a lower symmetry $I2_13$, which has a higher structural flexibility and was also supported by the investigations of Isasi et al. [43,48]
Subsequently Thangadurai et al. [43] published, by aid of a bond valence approach, that lithium is solely located in the octahedral sites and not in the tetrahedral site. [38]
Recently, based on the neutron diffraction data Cussen [29] confirmed the space group $Ia\bar{3}d$ as to be the appropriate symmetry group and additionally determined lithium positions. [24]
The contemporary valid model for tetragonal $Li_7La_3Zr_2O_{12}$ was developed by Awaka, having a lattice constant of $a = 13.134(4)$ Å $c = 12.663(8)$ Å. [22]

1.15. Lithium conductivity and migration pathways

In $Li_3Nd_3Te_2O_{12}$, where lithium is exclusively on tetrahedral positions, investigations showed, that lithium conductivity is very low at room temperature. This suggests that lithium atoms in these tetrahedral sites play no part in the conductivity of garnet-like materials. Contrary to ideal garnets, garnet-like materials have more lithium charge carriers and contain vacancies in tetrahedrally coordinated sites. These vacancies, which are absent in stoichiometric garnets, provide potential hopping sites for Li. Increasing the lithium content in a garnet-like structure will increase the occupation in the octahedral sites and the amount of

vacancies on tetrahedral sites (see Figure 1.14). This leads to the assumption that lithium conductivity is dependant on occupancies of tetrahedral and octahedral sites.

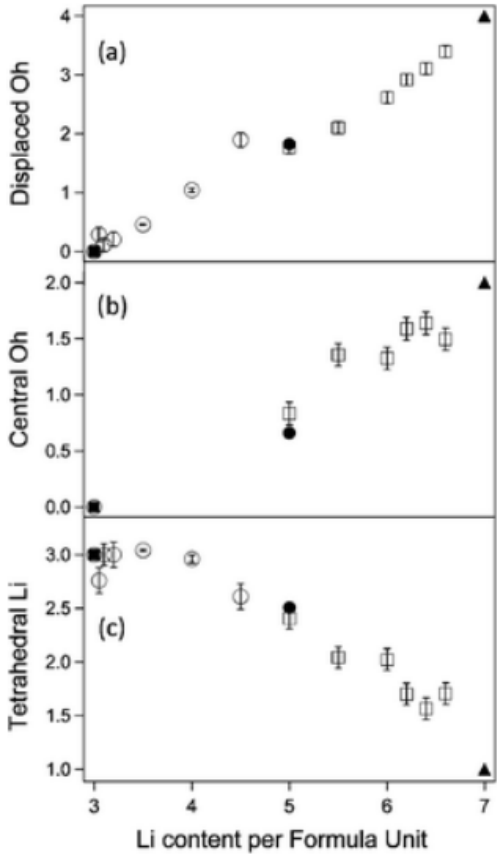

Fig.1.14: The number of lithium cations in octahedral and tetrahedral sites per formula unit for different lithium content

Providing potential hopping positions (vacancies) on tetrahedral as well as on octahedral positions, leads to the fact that Li in octahedral sites is highly mobile and thus these sites are responsible for the fast lithium ion conductivity. [45]

The lithium ion pathway through the structure is pictured in Figure 1.15. which is a sketch of connected polyhedra in $Li_5La_3Sb_2O_{12}$, sharing faces and edges, which form a three-dimensional network for lithium diffusion. [26]

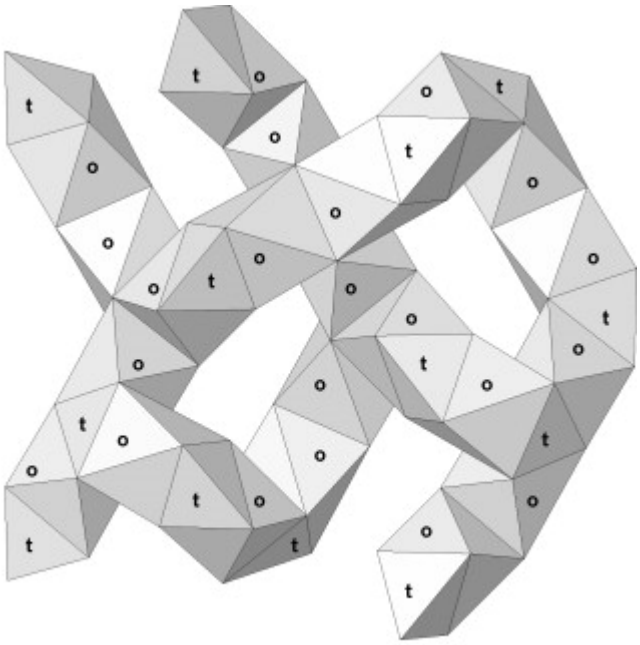

Fig.1.15: Three-dimensional network of polyhedra, which can host Li, in garnet-like materials. t: tetrahedral sites, o: octahedral sites

Lithium atoms in some of the tetrahedral sites deflect the local electric field and thus influence the ease of diffusion of lithium ions through the octahedral sites.

So lithium migration is significantly dependant on site occupancies and local *Li* arrangements. [45]

2. Experimental

2.1. Substitution in garnet-like materials

The idea behind substituting elements is that the variation of different parameters can lead to an increase of the lithium ionic conductivity in the material. Parameters that can be changed by substitution are:

- Lithium content and distribution on different sites
- Lattice parameter

The lithium content and thus the number of vacancies changes, when an element is replaced by another with a different oxidation number. As starting material in this work $Li_7La_3Zr_2O_{12}$ is used. Possible replacement positions are the eight-coordinated lanthanum position and the six-coordinated zirconium position. In principle each element can be used for substitution which tends to have the same coordination number as the just mentioned elements. Replacing the initial elements can also lead to a variation in lattice parameter depending on the ionic radius of the used elements.

2.1.1. Substitution elements and compositions

There is a huge range of possible elements for substitution in garnet-like materials. Due to insufficient investigation and a few promising results from the literature, the focus in this work is based on tantalum and the earth alkali elements calcium, strontium and barium. The purpose is to improve the lithium ionic conductivity by varying the composition and the lithium content, while the maximum number of lithium atoms per formula unit is seven.
Previous investigations made sure that exclusive replacement of lanthanum by earth alkali elements does not lead to phase-pure samples, which are thus not qualified as working material. This means that doping with calcium, strontium or barium has always to be carried out simultaneously with tantalum doping. The following graphs (Fig. 2.1.-2.4.) show the investigated compositions of this work.

2.1.1.1. Substitution of tantalum for zirconium

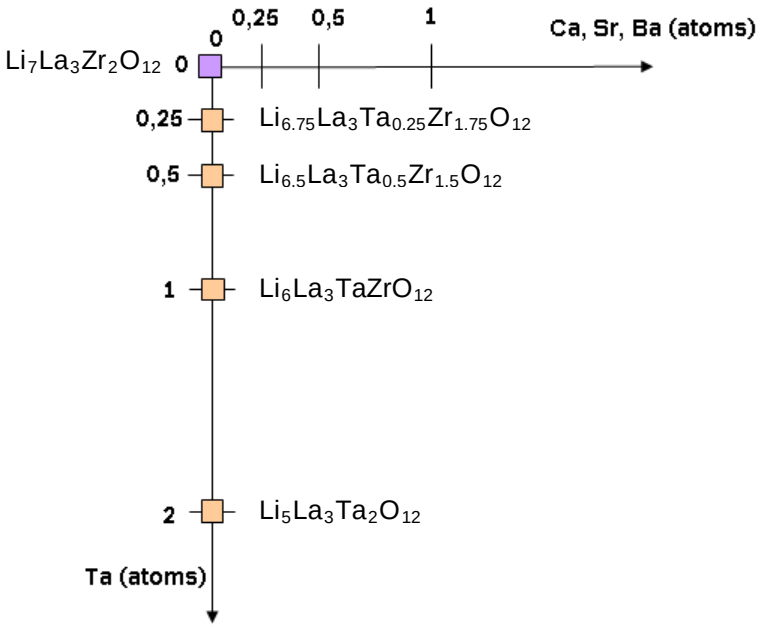

Fig.2.1: Compositions of investigated materials. Substitution of Ta for Zr

2.1.1.2. Substitution of calcium for lanthanum

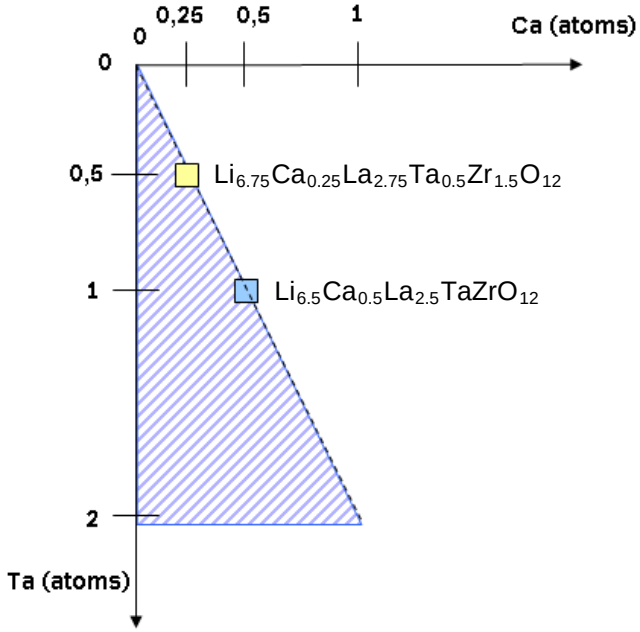

Fig.2.2: Compositions of investigated materials. Substitution of Ca for La

2.1.1.3. Substitution of strontium for lanthanum

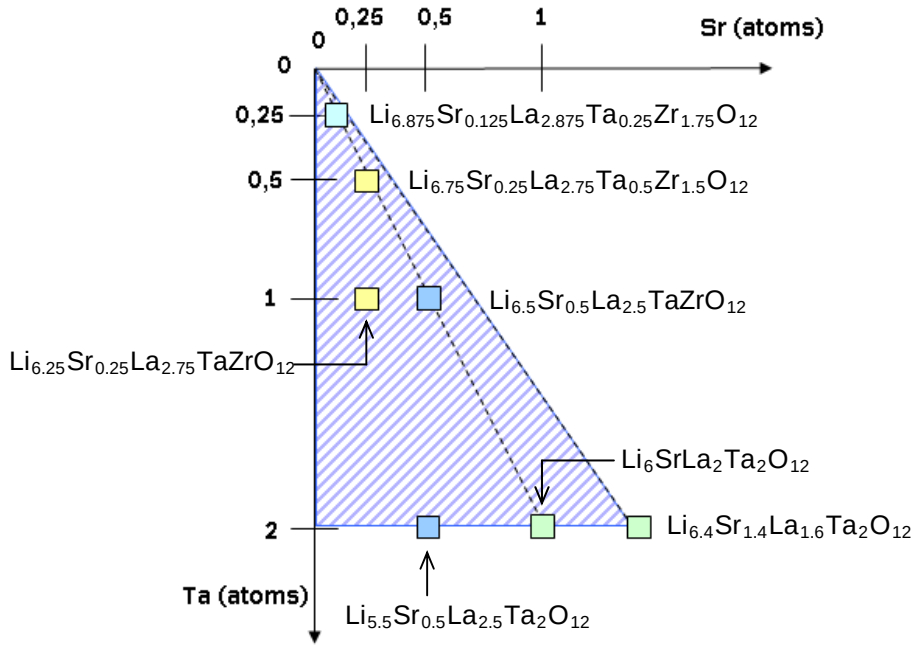

Fig.2.3: Compositions of investigated materials. Substitution of Sr for La

2.1.1.4. Substitution of barium for lanthanum

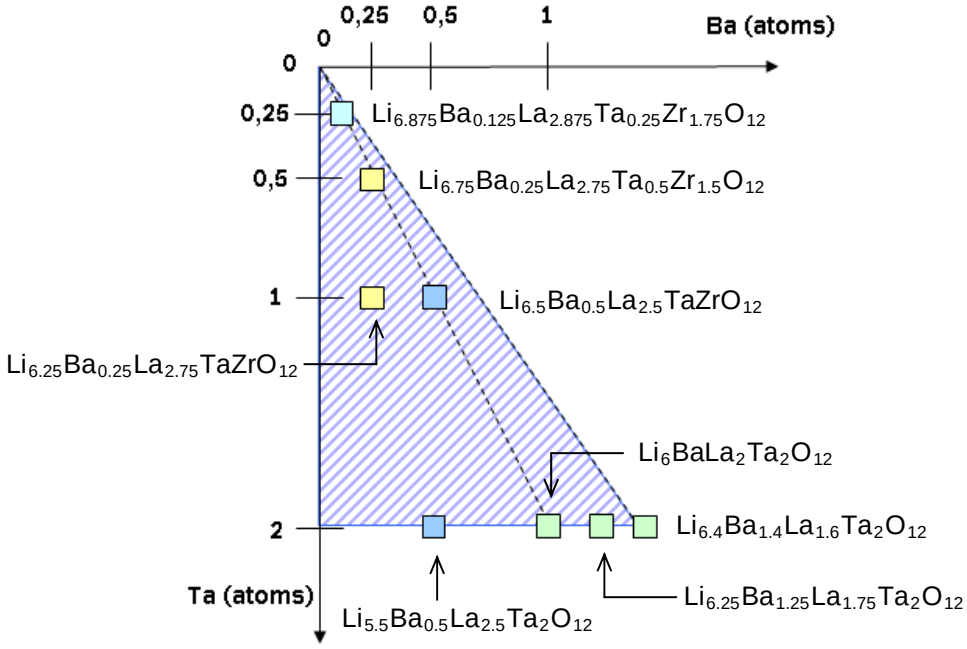

Fig.2.4: Compositions of investigated materials. Substitution of Ba for La

2.2. Sample preparation

2.2.1. Mixing of raw materials

All samples are prepared by a so called all-solid-state reaction. The raw materials are mixed in a bulb with water by means of a rotary evaporator at 100 °C for 2 hours. Under these conditions the reaction described in Equation 2.1. takes place.

$$La_2O_3 + H_2O \xrightarrow{2h,100°C} La(OH)_3 \qquad \text{Eq.(2.1.)}$$

Depending on the composition the following substances are used for the preparation of the various samples:

- *Lithium carbonate, ACS, 99.0 % min, Alfa Aesar*
- *Lithium nitrate, anhydrous, 99 %, Alfa Aesar (pre-dried for 12 hours at 120 °C)*
- *Zirconium(II)oxide, > 97 %, Saint Gobain (impurity: 2 % Hf)*
- *Tantalum(V)oxide, 99.85 % (metals basis), Alfa Aesar*
- *Lanthanum(III)oxide, REacton®, 99.99 % (REO), Alfa Aesar (pre-dried for 24 hours at 900 °C)*
- *Barium nitrate, ACS, 99+%, Alfa Aesar*
- *Strontium nitrate, ACS, 99.0 %min, Alfa Aesar*
- *Calcium nitrate tetrahydrate, ACS, 99.0-103.0 %, Alfa Aesar*

After mixing the raw materials the water is evaporated and the resulting powder is dried in the drying oven over night at 120 °C.

2.2.2. Calcination

The dried powder is ground in a mortar. Substances containing lithium nitrate are calcined at 850 °C, those which contain lithium carbonate at 900 °C with a heating rate of 180 K/h and 1 hour dwell. Because most of the common crucible materials are highly reactive towards lithium compounds (e.g. Li_2O, Li_2CO_3, $LiNO_3$, etc.) at elevated temperatures and due to its inertness, a gold crucible is used for calcination (see Figure 2.5.). The calcination is carried out in a muffle furnace *Nabertherm N11R* or *Linn VMK 1320* and during heat treatment, when the garnet forms, the crucible is covered with a MgO plate to avoid evaporation of material.

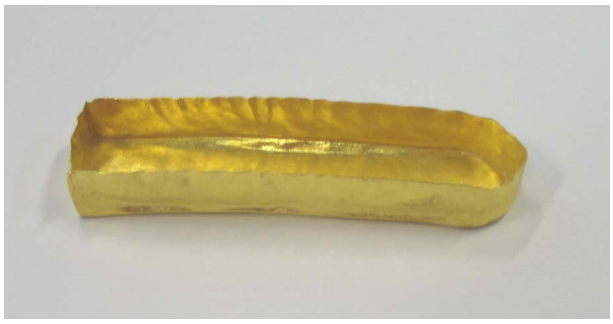

Fig.2.5: Gold crucible for calcination

2.2.3. Powder milling

After calcination, the powder is milled in a planetary ball mill *Retsch PM 400* for 1 hour with 200 revolutions per minute. Given amounts of material, solvent and zirconia-balls are introduced into a *Retsch* grinding jar made of ZrO_2 with a volume of 50 mL. To gain an optimum grinding capacity a defined ratio has to be considered. In order to avoid structural changes during milling cyclohexane is used as a non-polar solvent. The grinding jar rotates about its own axis and additionally in a circle. This performs lots of reaming contacts between the zirconia-balls and the combination of frictional and impact forces results in a pulverization. The centrifugal forces acting on the grinding jar wall initially carry the grinding balls in the direction in which the jar is rotating as shown in Figure 2.6.

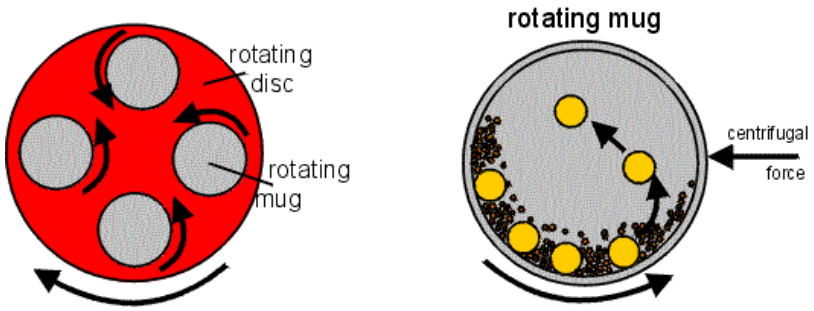

Fig.2.6: Principle of a planetary ball mill

After milling a solvent extraction with 2-propanol is done in a separating funnel to remove cyclohexane. Consequently 2-propanol is evaporated in the rotary evaporator and the obtained powder is dried again in the drying oven over night.

2.2.4. Pressing

Before sintering, the powder has to be brought into an suitable shape for electrical characterization. By aid of a pressing matrix, having a diameter of 10.0 mm, about 0.5 g of powder is pressed into a pellet in two steps.

The first pressing is done by means of a uniaxial electro-hydraulic powder press *P.O.Weber PW 5ED-EK* applying a force of 7000 N/10.0 mm and 10 s dwell. Afterwards the pellet is further compressed using an isostatic 4-pillarpress *P.O.Weber KIP 300EW* applying a force of 2500 kN/10.0 mm and 20 s dwell.

2.2.5. Sintering

Sintering is carried out in a muffle oven *Nabertherm L16/14*. An air-tight MgO box with reduced volume is used to maintain a high lithium oxide partial pressure around the sample. To avoid lithium evaporation during the heat treatment and to equilibrate the atmosphere around the sample, the pellet is positioned in the centre of a powder bed, which has always the same composition as the pellet. The MgO-boxes are positioned in a Al_2O_3-box to reduce again the possibility of air streaming in (see Figure 2.7).

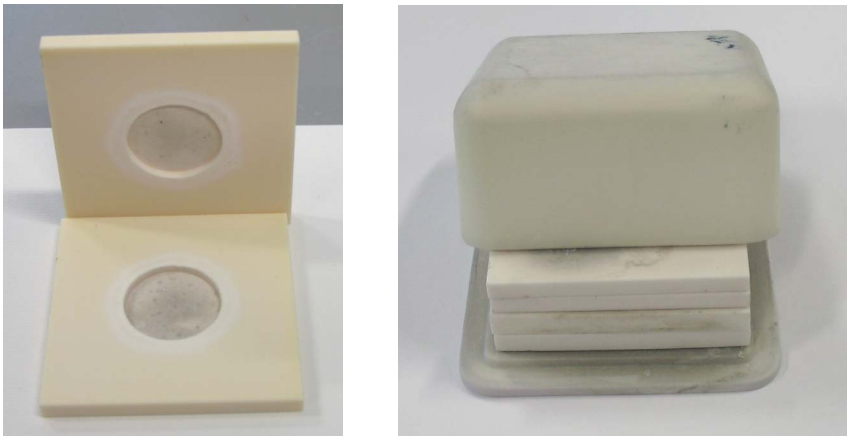

Fig.2.7: Left: MgO box, right: Al_2O_3-box

For sintering the temperature program shown in Figure 2.8. is applied.

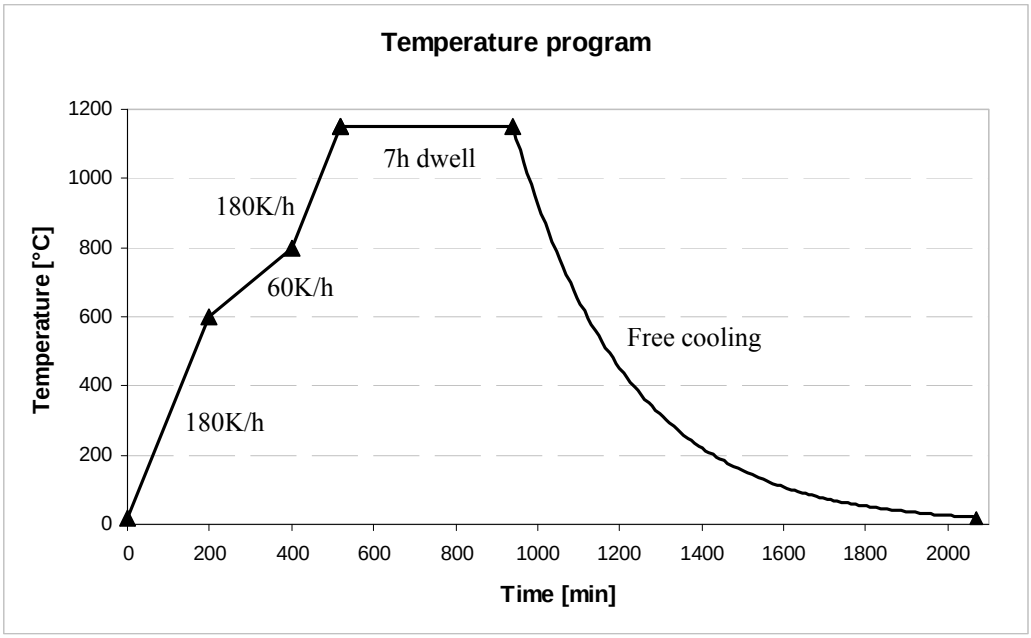

Fig.2.8: Temperature program for sintering

2.2.6. Estimation of density

After isostatic pressing and sintering the density of the samples is estimated by measuring the diameter, the thickness and the weight of the pellet. From the theoretical density ρ_t (Equation 2.2.) and the experimental density $\rho_{\exp}$ (Equation 2.3.), the relative density in percent $\rho_{\%}$ (Equation 2.4.) can be calculated.

$$\rho_t = \frac{\sum \frac{M_{element}}{N_A} \cdot x_{element}}{a^3} \qquad \text{Eq.(2.2.)}$$

$$\rho_{exp} = \frac{m}{D\frac{\pi}{4}d^2} \qquad \text{Eq.(2.3.)}$$

$$\rho_{\%} = \frac{\rho_t}{\rho_{rel}} \cdot 100 \qquad \text{Eq.(2.4.)}$$

$M_{element}$ is the molar mass of the contained elements, N_A is Avogadro's constant, $x_{element}$ is the number of Atoms of a certain element in the unit cell, a is the lattice parameter, m is the mass, D is the thickness and d is the diameter of the pellet.

2.2.7. Preparation for electrical characterization

For impedance spectroscopy two electrodes have to be applied onto the sample before electrical characterization. On each side of the sample a reinforcing ring with 5.5 mm in diameter is pasted to have a defined electrode area, which is important for the subsequent evaluation. In argon atmosphere three layers of gold are sputtered on each side by a *Cressington Sputter coater 108 auto* using a current of 40 mA for 150 seconds.
After sputtering the samples are heated at 260 °C for 2 hours in a muffle oven to make sure, that there is no reaction of the platinum rod with the electrode during impedance measurement.

2.3. Introduction to characterization methods for garnet-like materials

All samples are characterized after certain working steps to determine their most important properties. The following scheme (Fig. 2.9) illustrates all working steps and the inbetween accomplished characterizations.

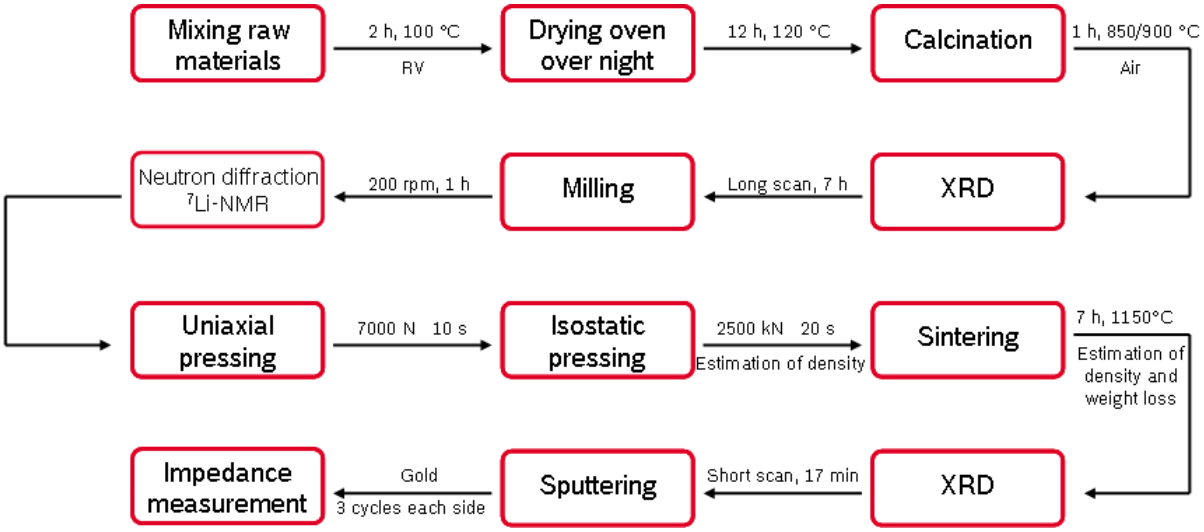

Fig.2.9: Schematic representation of all working steps and characterization methods

2.3.1. Structural characterization by X-ray diffraction analysis

In order to determine the structure and the lattice parameter, x-ray powder diffraction data were collected using a Bruker D8 advance. It is equipped with a copper tube and a monochromator emitting radiation with a wavelength of $CuK_{\alpha 1} = 1{,}5405$ Å. An aperture

pinhole with a gap length of 1 mm limits the irradiated area of the sample. A scattering beam pinhole shields the detector from scattered radiation.

A small amount of powder is pressed into the powder sample holder by aid of a glass plate to obtain a flat surface. Pellets are positioned onto a piece of plasticine so that the surface is parallel regarding the sample holder.

Each calcined garnet-powder is measured twice with a long scan program covering the diffraction-angle range $5 < \Theta < 188$ and having a duration of 7 hours corresponding to 4 seconds of measurement per degree.

Due to time and capacity reasons sintered pills are subjected just once to a short scan program which scans the diffraction-angle range $10 < \Theta < 60$ to make sure, that the product is the same after the heat treatment. This program has a duration of 17 minutes corresponding to 1 second per degree.

In the program TOPAZ (software of Bruker AXS) Rietveld refinement for structure determination was performed using the models of Cussen and Awaka (see Chapter 1.14.) for the cubic respectively the tetragonal phase. Secondary phase peaks were determined in the program EVA (database software of Bruker Axs) and the parameters of these substances are added to TOPAZ for Rietveld refinement.

2.3.2. Structural characterization by neutron diffraction

By aid of neutron diffraction it is possible to determine the atomic or magnetic structure of a material. Especially in combination with knowledge from X-ray diffraction data, it is possible to investigate atom positions of light elements when heavy scattering elements are present in the material. For neutron diffraction thermal neutrons are used exclusively. Contrary to X-rays, neutrons are diffracted by the core of the elements. The absorption of neutrons is relatively low compared to X-rays and can thus be neglected. As the wavelengths of thermal neutrons are in the same order of magnitude as the interatomic distances and as their magnetic moment may interact with those of the material, they are predestined for structural and magnetic research.

The scattering power of an element is indicated by the scattering length b, which is shown in Figure 2.10.

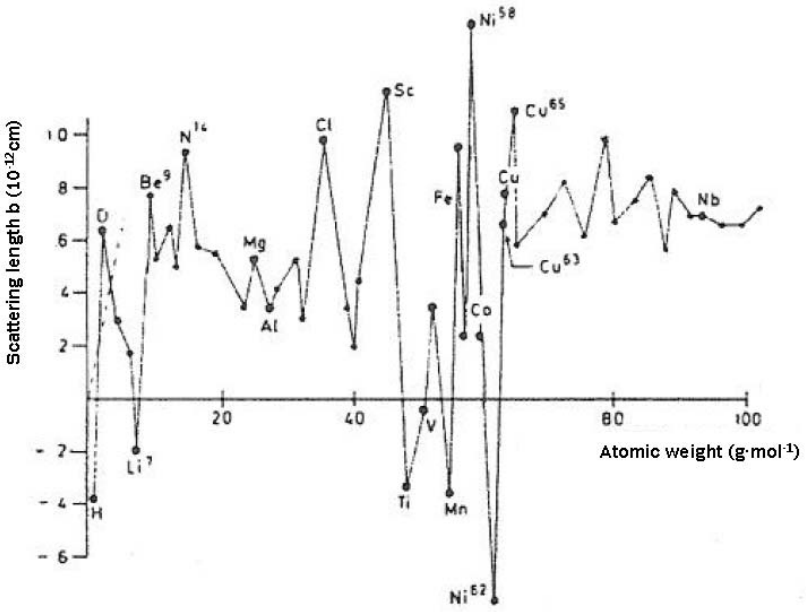

Fig.2.10: Scattering lengths of elements

Values of b vary non-systematically with the atomic weight, can be positive or negative and are specific for each nucleus and thus specific for each isotope. Due to the latter fact it is possible to determine atom positions within a structure in a more detailed manner.

As Bragg's law, Laue equations and Ewald sphere are also valid for neutron diffraction, it can be treated equal to X-ray diffraction. For profile refinement the Rietveld method is used. Neutron and X-ray diffraction are often used complementarily used for verification of the distribution of the cations. [13]

Because measuring time is expensive and limited just one promising sample was sent to Garching (Munich) for neutron diffraction. Evaluation of neutron diffraction data was carried out by Dr. Thomas Köhler (Bosch CR/ARA) and Dr. Helmut Ehrenberg (IFW Dresden).

2.3.3. Electrical characterization by impedance spectroscopy

Impedance spectroscopy is a powerful method to characterize electrical properties of materials. It is possible to investigate the dynamics of charge carriers within the bulk or grain boundary regions in solid materials. Within materials the following effects can appear: ionic, semiconducting, mixed electronic-ionic and electronic conduction. Before characterizing the sample, two identical electrodes have to be applied on both sides of the sample.

The general idea behind impedance spectroscopy is to apply an electrical stimulus, such as a known voltage or current, and to investigate the response of the sample. The electrical response includes the transport of charged particles through the material and the transfer at the

material-electrode interface. The flowrate of charged particles depends on the ohmic resistance of the material and the electrodes and on the reaction rates at the material-electrode interface. In impedance spectroscopy, the most common method is to measure the impedance directly in a certain frequency domain by determining the imaginary (Z'') and real (Z') part of the resulting current at that frequency. Thus the phase difference θ between the voltage and the current and the magnitude of the impedance $|Z|$ are gained as shown in Figure 2.11.

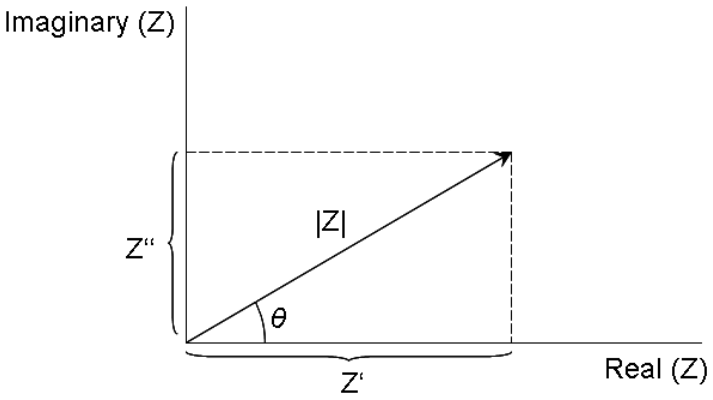

Fig.2.11: The impedance $|Z|$ plotted as a vector

The used impedance spectrometer (IS) is able to measure in frequency ranges between 32000 and 0.01 Hz. The employed impedance measuring station consists of several parts where the total arrangement is shown in Figure 2.12:

- Sample holder
- Oven
- Oven controller *HTM Reetz*
- Computer
- Datalogger for temperature detection *MV 100 Mobile Coder*
- Current generator *Solartron Dielectric Interface 1296*
- Analyzer *Solartron Impedance/Gain-Phase Analyzer SI 1260*

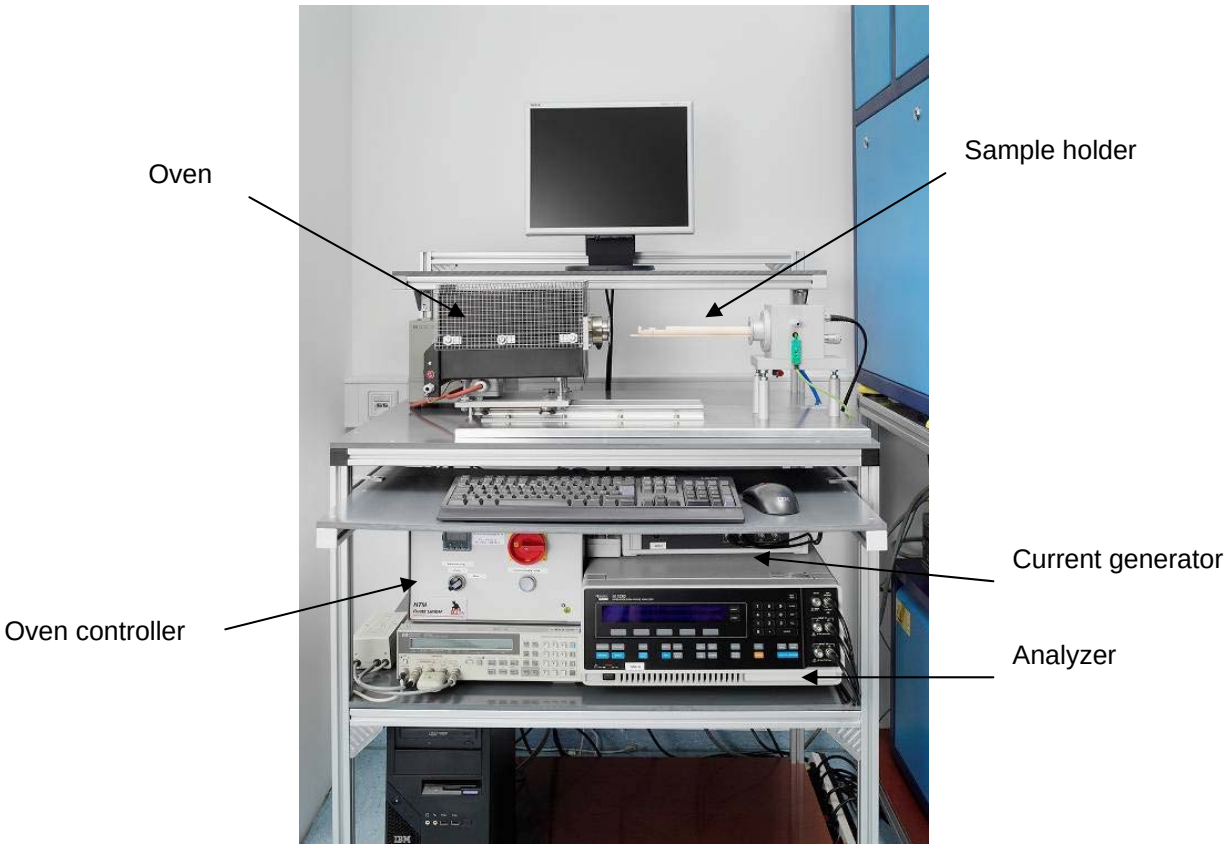

Fig.2.12: Impedance measuring station

Generally, the impedance is frequency-dependent, but conventional impedance spectrometry measures the impedance as a function of the angular frequency $Z(\omega)$.

A convenient representation of data is the so called Nyquist plot. Here, the real part of $Z(\omega)$ is plotted on the x-axis, while the imaginary part is plotted on a negative y-axis as shown in Figure 2.13.

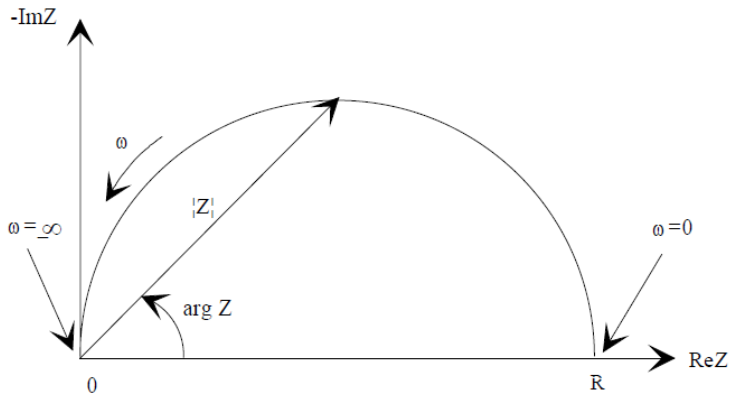

Fig.2.13: Nyquist plot

Each point on the Nyquist plot corresponds to a given frequency. For evaluation, the semicircle has to be described by an electrical circuit. It is very complicated to give a complete physicoelectrical model of all occurring processes, which might occur during the measurement. Usually the experimental impedance data are approximated by an equivalent circuit consisting of ideal resistors, capacitors and inductors. Normally it is not possible to model an electrochemical cell by using just a single equivalent circuit element and thus the elements are connected in parallel and series combinations.
The semicircle shown in Figure 2.13 is characteristic of a single time constant and can be described by a parallel combination of a capacitor and a resistor (see. Figure 2.14).

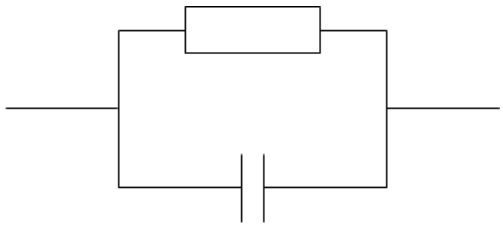

Fig.2.14: Equivalent circuit consisting of a capacitor and a resistor to describe a semicircle

Sometimes capacitors do not show ideal behavior during impedance measurements. Often a constant phase element (CPE) is used in a model in place of a capacitor to compensate these inhomogeneities in the system.
Diffusing charge carriers are creating an impedance called a Warburg impedance. Lower frequencies correspond to diffusion deeper into the material. If the material is thin, the low-frequency electric field will penetrate the entire thickness, creating a Finite Length Warburg element (W_S). If the material is thick enough so that the applied electric field of lowest frequencies does not fully penetrate the layer, it must be interpreted as infinite (W_O). [7, 14]

To measure the conductivity of the samples at room temperature normally a frequency between 32000 and 1 Hz is applied. For samples with higher resistivities frequencies up to 0.01 Hz are applied. The sample is clamped into the sample holder so that the two platinum rods are contacting the gold electrode. Impedance data are collected in the program “SMaRT” (software of Solartron). The evaluation of conductivity data is done by a graphical method in Excel. Therefore the negative imaginary impedance ($-Z_{imag}$) is plotted against the real impedance (Z_{real}) and the minimum value corresponding to the x-axis before the ion-blocking tail (see Figure 2.15) is inserted in Equation 2.5.

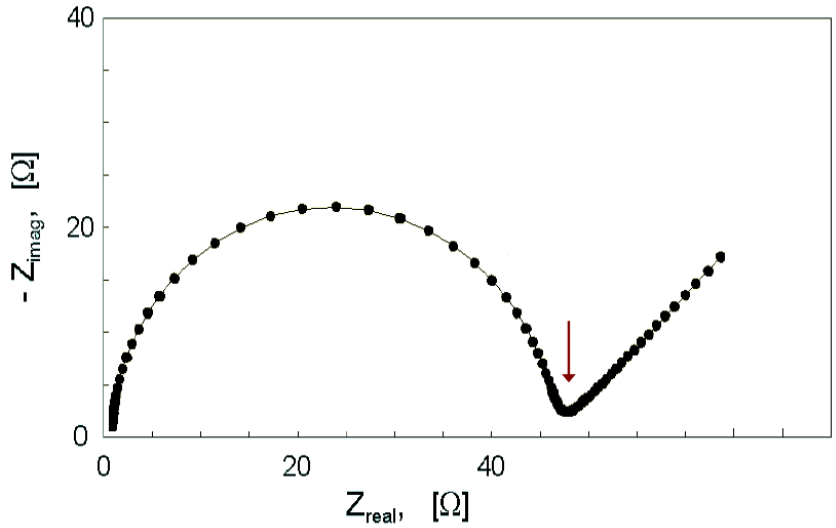

Fig.2.15: Graphical evaluation of conductivity data

$$\sigma = \frac{L}{\rho \cdot A} \qquad \text{Eq.(2.5)}$$

σ corresponds to the conductivity, L is the thickness of the sample, ρ is the resistance of the sample and A is the area of the sputtered electrodes.

To measure the activation energy, impedance data at different temperatures are required. Because the produced materials are good ionic conductors, it is not possible to obtain impedance data above 150°C because at higher temperatures no semicircles can be seen anymore. After fixing the sample in the sample holder as described before, the platinum radiation shield is closed and the sample holder is moved into the oven. Afterwards the oven and a program in SMaRT are started at the same time. The measuring program contains a 40 minutes delay, where the oven heats up to 150 °C in 20 min and stays there for another 20 min to get into equilibrium. Then the measuring station measures the impedance every eight minutes cooling down to room temperature. The system being measured should be in an equilibrated state throughout the time during the measurement. As it is difficult to achieve a short measuring time and an equilibrated state a cooling rate of 2.5 °C/min is applied.
There are two possibilities to evaluate the activation energy data. In each case Equation 1.16 (Chapter 1.10.1.) has to be used for the calculation.
The first possibility is to do the same graphical evaluation procedure as described for conductivity measurement for every different temperature curve. The resistance values obtained in this way are then plotted as $\ln\frac{T}{\rho}$ versus $\frac{1}{RT}$ as can be seen in Figure 2.16, where

T is the temperature in K, ρ is the resistance in Ω and R is the gas constant in $eV \cdot K^{-1} \cdot atom^{-1}$.

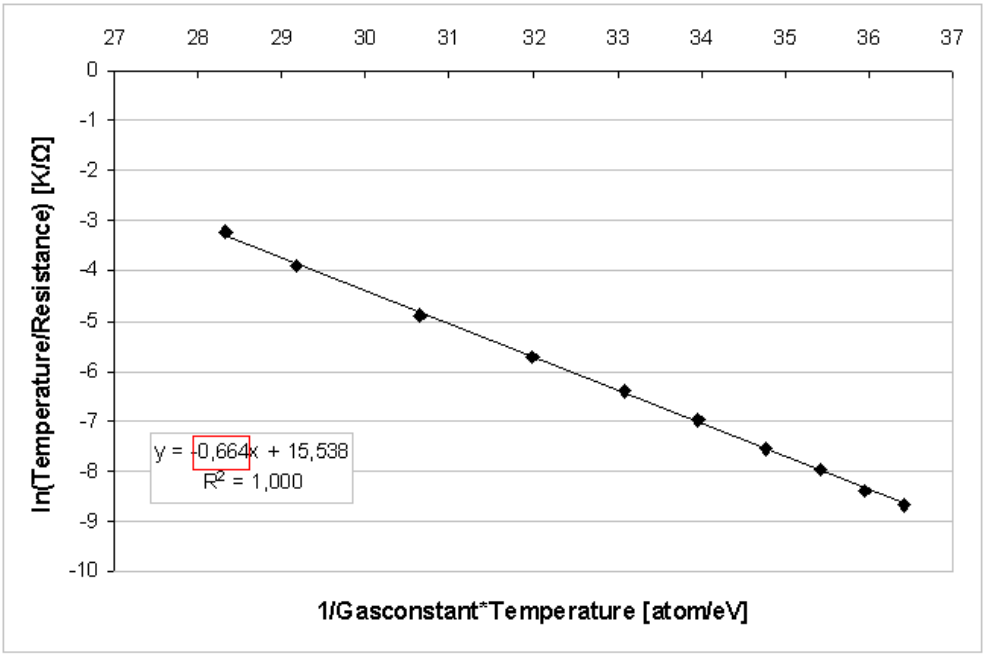

Fig.2.16: Resistance plotted as function of the temperature

The plotted data points can be connected by a straight line. From the corresponding slope the activation energy in eV can be read off easily.

The second method is by using a special evaluation software called "ZView" (software of Solartron). By means of this software it is possible to create an equivalent electrical circuit for each curve at each temperature. After inserting starting values for the different circuit elements, the program simulates the generated model and calculates a fit with the smallest errors for the various elements. The achieved resistance values are plotted as $\sigma \cdot T$ versus $\frac{1}{T}$ with a logarithmic scale on the y-axis. After combining the data points by an exponential curve, the activation energy can be calculated from the exponent of the linear equation.

As the difference between the first and the second method is negligible, in the following the evaluation was done exclusively according to the first method.

2.3.4. Microstructural investigation

After complete characterization of each sample the latter are investigated using light microscopy (*Zeiss Axioplan*), scanning electron microscope (SEM) and EDS to determine its microstructure.

The samples are embedded into epoxy resin, grinded and polished. After investigation with a bright field microscope the pellets are sputtered with graphite to get a conductive surface for the electron beam of the SEM in order to avoid accumulation of electrons and thus melting of the sample.

Within a SEM an electron beam is created, focused and accelerated towards the sample. Deflection coils move the electron beam which enables a scanning of the sample surface. Different signals, caused by interactions with the electrons of the sample are collected by appropriate detectors and used for illustration and analytical methods. For illustration the signal is amplified and converted into a video signal.

For the generation of an electron beam a filament is needed as cathode which acts as electron source. To accelerate the beam, a high voltage difference is applied between the anode and the cathode. Right after the filament cathode, a Wehnelt cylinder is located, focusing the electron beam. An overview about the most important parts of a SEM is given in Figure 2.17.

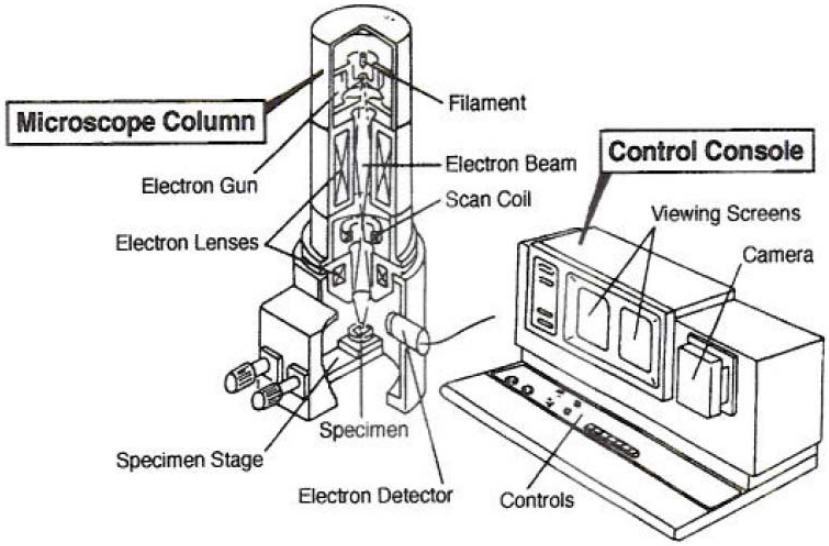

Fig.2.17: Assembly of a scanning electron microscope

As electrons cannot be focused by normal optical lenses, electromagnetic coils are applied as lenses.

When the primary electron beam is impacting the sample a number of different interactions take place. A certain part of the primary electrons are scattered elastically at the cores of the

atoms and are called back scattering electrons. The higher the atomic number the more electrons are interacting with the atom and the brighter the picture. High-energetic primary electrons are scattered inelastically at atomic shell electrons and loose their kinetic energy. By influence of this energy electrons of the outer shell can be released and are called secondary electrons (SE).

Besides back scattering electrons and secondary electrons X-ray radiation and Auger electrons can be generated. The generation of these electrons is shown in Figure 2.18.

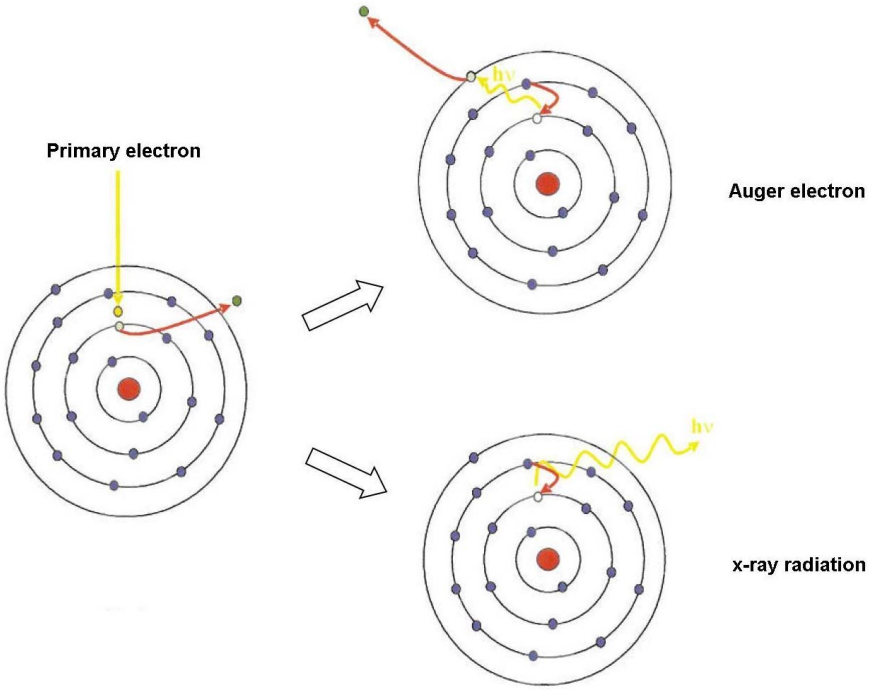

Fig.2.18: Generation of Auger electrons and X-ray radiation during SEM investigation

Primary electrons are decelerated by the negative charge of the shell electrons and are loosing energy, which is emitted as X-rays. If these X-rays are hitting another electron of the shell, an electron called Auger electron is emitted.

The X-ray energy is measured with a special detector and can be assigned exactly to one special electronic transition of an element. This is called energy dispersive X-ray spectroscopy (EDS) and is used for chemical analysis. [16]

The employed SEM was a *Zeiss Supra 55 VP* having an EDS of *Oxford Instruments type INCA Energy*. The samples were investigated with magnifications between 100 and 5000. REM pictures were made by applying an acceleration voltage of 10 kV, while EDS analysis was done with an acceleration voltage of 20kV to obtain a better resolution.

3. Results

In the following chapter the various characteristics of the prepared samples are listed. The tables containing structural characteristics show the “lattice parameter powder” which is the lattice parameter of the calcined powder and the “lattice parameter pellet” which is the lattice parameter of the sintered pressed pellet. All further particulars (“Cubic garnet”, “Secondary phases”, “Density”, “Shrinkage”, “Weight loss”) refer to the sintered pellet.
“Shrinkage” corresponds to the volume shrinkage of the sample which was determined by measuring the geometrical change in volume before and after sintering. Also the “weight loss” refers to the change in mass before and after sintering. The term “Number of semi-circles” stands for the number of observed semi-circles in the impedance plot for conductivity measurement. Furthermore figures will illustrate correlations between content of substitution elements and lattice parameter. The unit of substitution elements is [atoms], which has to be understood as number of replaced atoms per formula unit. In the following the conductivity is designated as σ and the activation energy as E_A. The errors for the error calculation are assumed to be 1.7 % for the thickness measurement, 0.2 % for the resistance measurement, 2.8 % for the reading error and 1.8 % for the area of the electrode.
The following chapters will show selected curves for conductivity, activation energy and pictures of light microscopy and SEM. All other curves and pictures of materialographic investigation are attached in Appendix 1 and 2.

3.1. $Li_7La_3Zr_2O_{12}$ garnet materials

Two pellets of $Li_7La_3Zr_2O_{12}$ with different weights were prepared. The Tables 3.1 and 3.2 show the structural and the electrical characteristics, respectively, of the prepared samples.
After sintering the lattice parameter decreased as compared to the calcined powder. Beside the main cubic garnet phase, only tetragonal garnet was found as secondary phase. The shrinkage of the sample as well as the weight loss is high after sintering. From Table 3.2 it can be seen that the conductivity before and after measurement of the activation energy decreases drastically. Figure 3.1 shows a typical XRD pattern of a tetragonal garnet. In this case it is the pattern of calcined $Li_7La_3Zr_2O_{12}$.

Composition	Mass [g]	Lattice parameter powder [Å]	Lattice parameter pellet [Å]	Cubic garnet [%]	Secondary phases	Density [%]	Shrinkage [%]	Weight loss [%]
$Li_7La_3Zr_2O_{12}$	0.7335	12.970(5)	12.984(3)	50	50% tetragonal garnet	79	33.58	10.62
$Li_7La_3Zr_2O_{12}$	0.5175	12.970(5)	12.980(4)	67	33% tetragonal garnet	73	27.97	10.18

Tab.3.1.: Structural properties of $Li_7La_3Zr_2O_{12}$ material

Sample name	σ before E_A measurement [S·cm^{-1}]	Number of semi-circles	σ after E_A measurement [S·cm^{-1}]	Activation energy [eV]	R-value of trend line
$Li_7La_3Zr_2O_{12}$_thick	$1.50 \cdot 10^{-5}$	1	$1.87 \cdot 10^{-6}$	0.73	0.999
$Li_7La_3Zr_2O_{12}$_thin	$3.47 \cdot 10^{-6}$	1	$1.38 \cdot 10^{-8}$	0.69	0.997

Tab.3.2.: Electrical properties of $Li_7La_3Zr_2O_{12}$ material

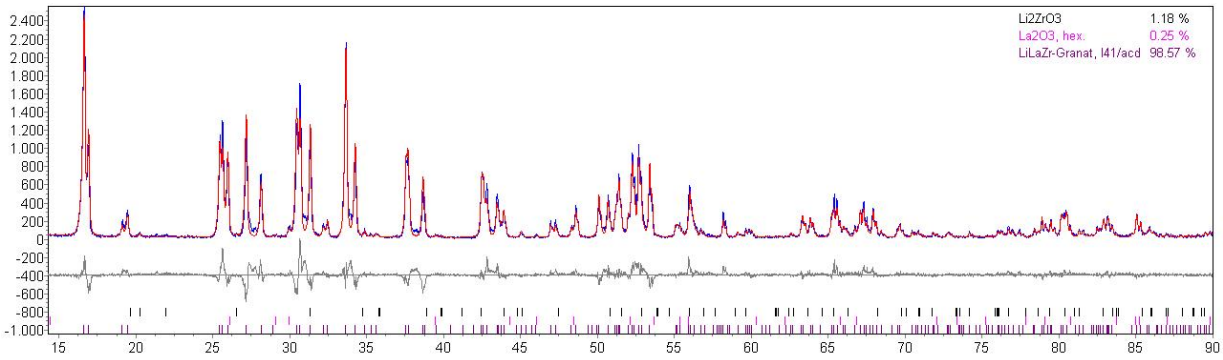

Fig.3.1: Typical XRD pattern for a tetragonal garnet, here $Li_7La_3Zr_2O_{12}$

Figure 3.2 illustrates the impedance plot for the conductivity measurement of $Li_7La_3Zr_2O_{12}$.The appearing semi-circle is typical for conducting materials, while the linear tail at low frequencies indicates that the conduction is of ionic nature. This straight line is effected by the Li^+ blocking gold electrode.

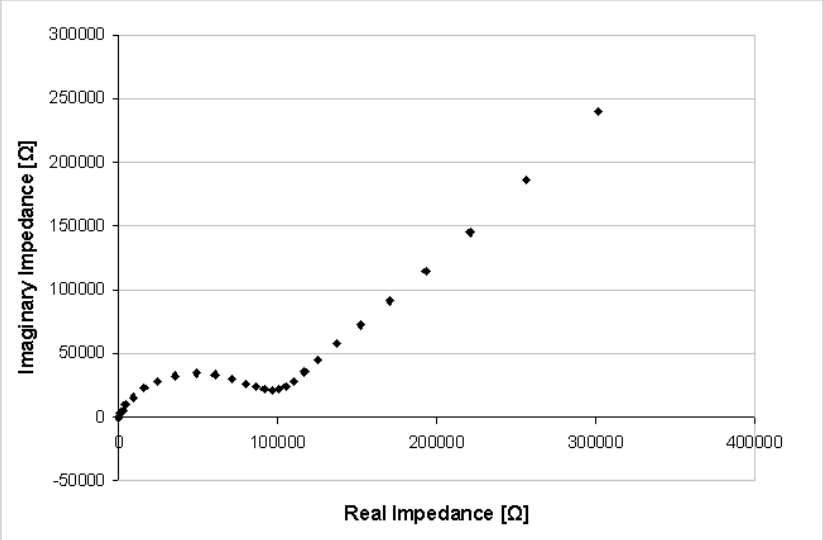

Fig.3.2: Impedance plot for conductivity measurement of $Li_7La_3Zr_2O_{12}$ *(thick pellet) at room temperature before measurement of activation energy*

Figure 3.3 shows the impedance plots for the determination of the activation energy of $Li_7La_3Zr_2O_{12}$ between 35 °C and 136 °C and the corresponding evaluation is given in Figure 3.4.

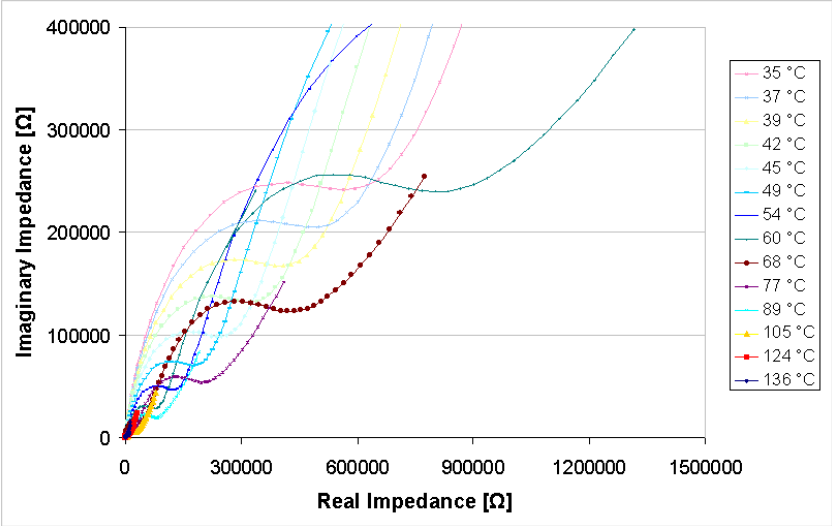

Fig.3.3: Impedance plot for activation energy measurement of $Li_7La_3Zr_2O_{12}$ (thick pellet) between 35 °C and 136 °C

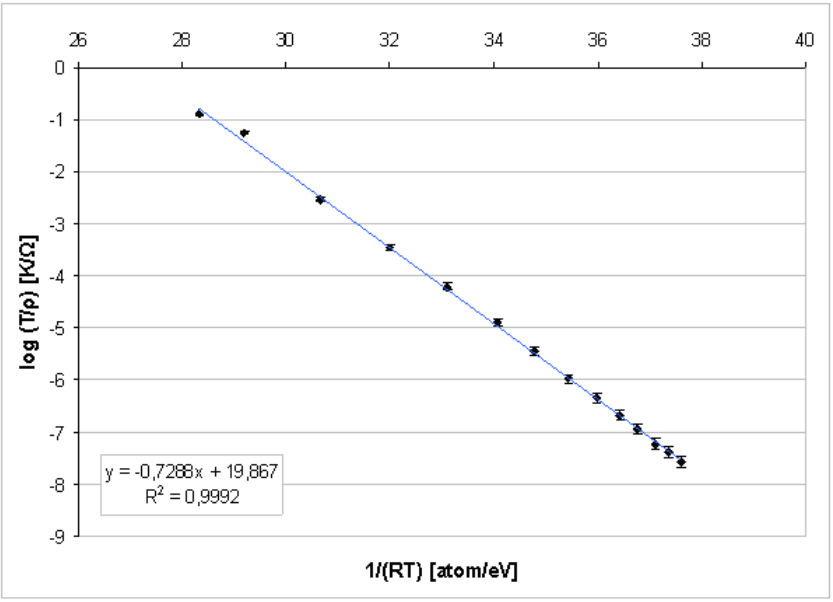

Fig.3.4: Arrhenius plot, log(T/ρ) vs. 1/(RT) of $Li_7La_3Zr_2O_{12}$ (thick pellet) between 35 °C and 136 °C. The slope of the line contains the activation energy.

Investigation by light microscopy showed, that there are two different regions inside the pellet. Figures 3.5 and 3.6 give the microstructure of the different regions of $Li_7La_3Zr_2O_{12}$ (thick pellet) with varying magnifications.

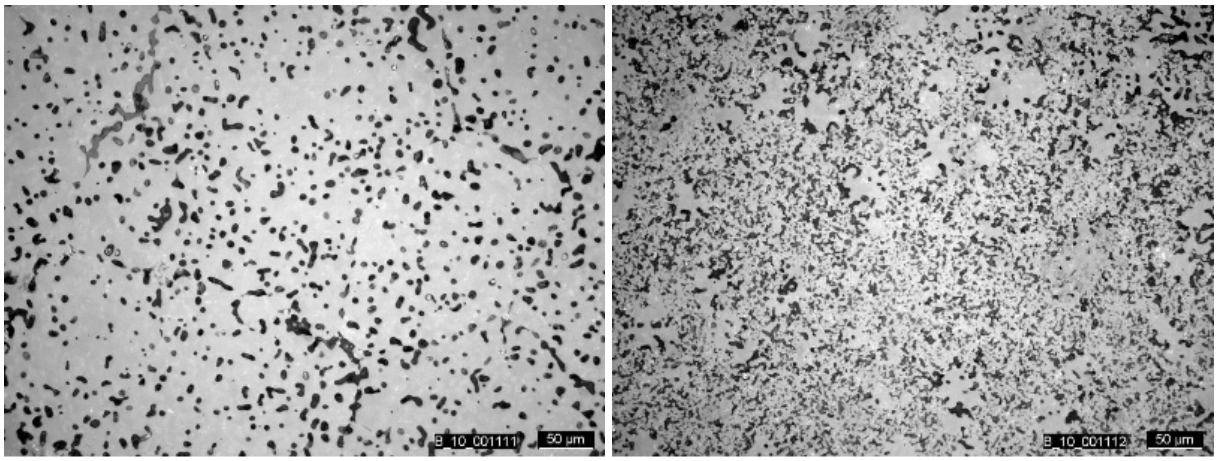

Fig.3.5: Microstructural investigation of $Li_7La_3Zr_2O_{12}$ (thick pellet) by light microscopy.

Left picture: edge, Right picture: middle.

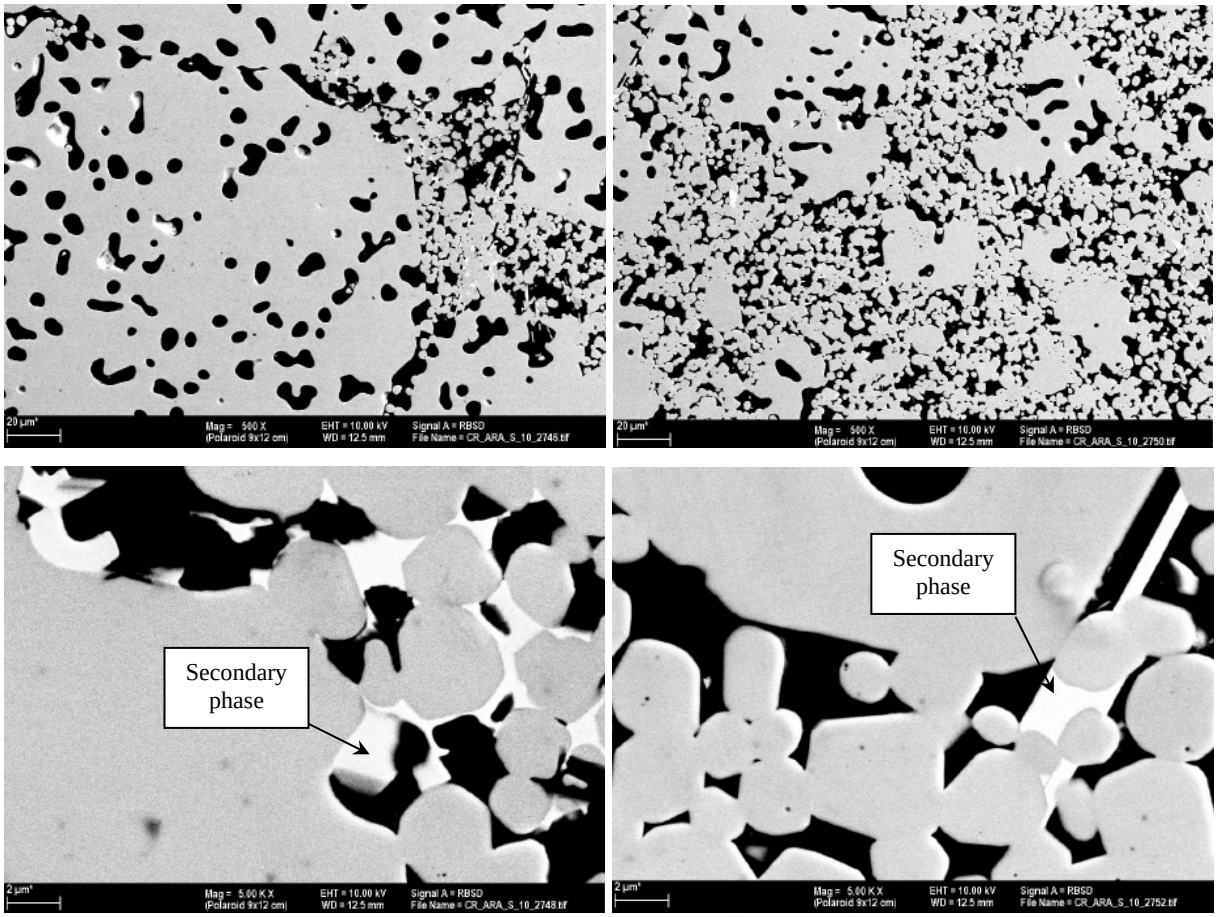

Fig.3.6: Microstructural investigation of $Li_7La_3Zr_2O_{12}$ (thick pellet) by SEM.

Left pictures: edge, Right pictures: middle

The pictures show huge crystals with large asymmetric pores and a white secondary phase. EDS investigation proved, that this secondary phase contains La, Al and O. The huge crystals having an angular shape were built by exaggerated grain growth.

3.2. $Li_{7-x}La_3Ta_xZr_{2-x}O_{12}$ garnet materials

Four different compositions were investigated where of each two samples with different weights were prepared. The Tables 3.3 and 3.4 summarize the structural and electrical properties of the samples. With the exception of $Li_{6.25}La_3Ta_{0.25}Zr_{1.75}O_{12}$, all samples could be prepared with a phase purity of the cubic garnet phase of 100%. The weight losses are comparable for all samples.

Figure 3.7 presents a typical XRD pattern for a cubic garnet, which is in this case for $Li_5La_3Ta_2O_{12}$. Other cubic garnets, having various substitutional elements, show similar patterns.

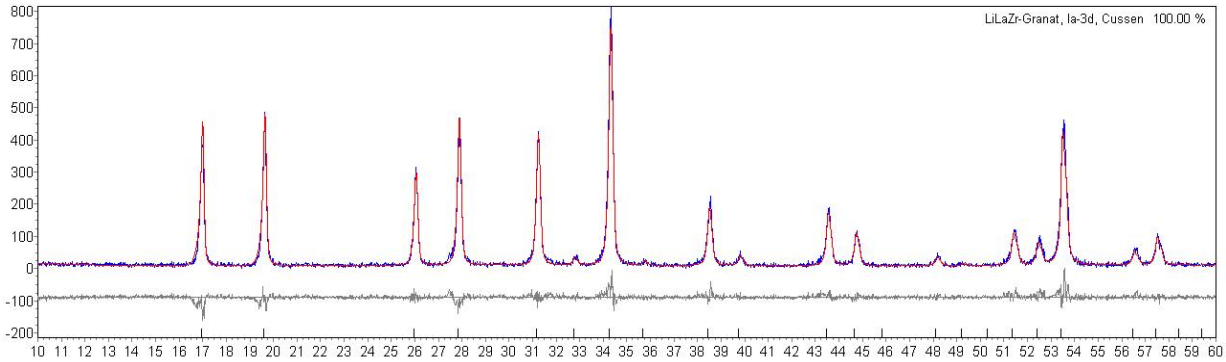

Fig.3.7: Typical cubic garnet pattern, here: $Li_5La_3Ta_2O_{12}$

Figure 3.8 shows the dependence of the lattice parameter on tantalum content of calcined powder. It can be seen that the lattice parameter is decreasing when the tantalum content is increased.

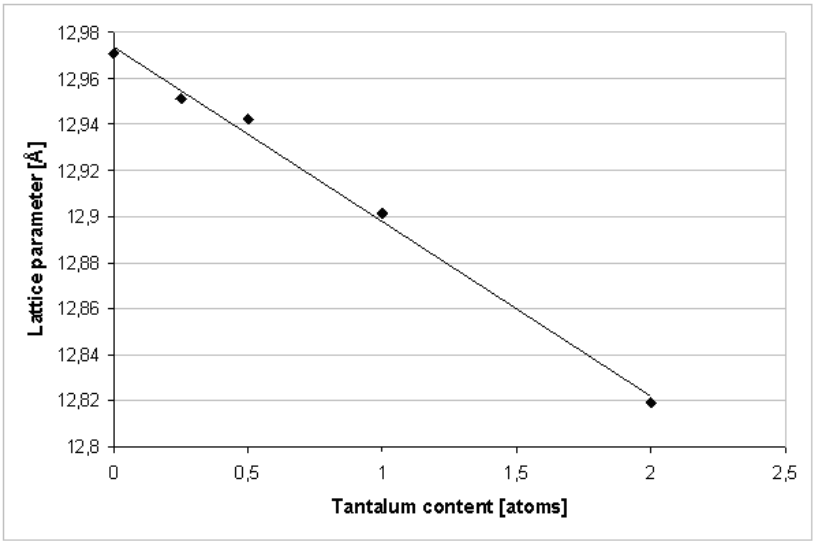

Fig.3.8: Dependence of lattice parameter on tantalum content.

Composition	Mass [g]	Lattice parameter powder [Å]	Lattice parameter pellet [Å]	Cubic garnet [%]	Secondary phases	Density [%]	Shrinkage [%]	Weight loss [%]
$Li_{6.75}La_3Ta_{0.25}Zr_{1.75}O_{12}$	0.8032	12.950(9)	12.968(0)	93	7% $La_2Zr_2O_7$	81	24.79	5.50
$Li_{6.75}La_3Ta_{0.25}Zr_{1.75}O_{12}$	0.5523	12.950(9)	12.966(6)	93	7% $La_2Zr_2O_7$	81	25.29	5.69
$Li_{6.5}La_3Ta_{0.5}Zr_{1.5}O_{12}$	0.6954	12.942(6)	12.947(9)	100	-	63	7.76	7.49
$Li_{6.5}La_3Ta_{0.5}Zr_{1.5}O_{12}$	0.5564	12.942(6)	12.949(7)	100	-	63	6.90	7.47
$Li_6La_3TaZrO_{12}$	0.7923	12.901(1)	12.901(2)	100	-	65	11.89	7.47
$Li_6La_3TaZrO_{12}$	0.5313	12.901(1)	12.899(6)	100	-	67	13.69	6.10
$Li_5La_3Ta_2O_{12}$	0.7571	12.819(2)	12.821(1)	100	-	84	26.07	3.46
$Li_5La_3Ta_2O_{12}$	0.5521	12.819(2)	12.822(1)	100	-	84	25.30	3.44

Tab.3.3.: Structural properties of $Li_{7-x}La_3Ta_xZr_{2-x}O_{12}$ materials

Sample name	σ before E_A measurement [S·cm^{-1}]	Number of semi-circles	σ after E_A measurement [S·cm^{-1}]	Activation energy [eV]	R-value of trend line
$Li_{6.75}La_3Ta_{0.25}Zr_{1.75}O_{12}$_thick	$7.17\cdot10^{-6}$	2	$1.10\cdot10^{-6}$	0.76	0.998
$Li_{6.75}La_3Ta_{0.25}Zr_{1.75}O_{12}$_thin	$1.16\cdot10^{-5}$	2	$3.61\cdot10^{-7}$	0.78	0.998
$Li_{6.5}La_3Ta_{0.5}Zr_{1.5}O_{12}$_thick	$3.34\cdot10^{-6}$	2	$4.00\cdot10^{-7}$	0.73	0.999
$Li_{6.5}La_3Ta_{0.5}Zr_{1.5}O_{12}$_thin	$7.32\cdot10^{-7}$	2	$5.25\cdot10^{-8}$	0.76	0.999
$Li_6La_3TaZrO_{12}$_thick	$6.91\cdot10^{-6}$	2	$3.35\cdot10^{-7}$	0.74	0.999
$Li_6La_3TaZrO_{12}$_thin	$1.15\cdot10^{-5}$	2	$1.32\cdot10^{-7}$	0.74	0.999
$Li_5La_3Ta_2O_{12}$_thick	$3.69\cdot10^{-6}$	1	$4.67\cdot10^{-6}$	0.65	0.999
$Li_5La_3Ta_2O_{12}$_thin	$2.78\cdot10^{-6}$	1	$3.29\cdot10^{-6}$	0.65	0.999

Tab.3.4.: Electrical properties of $Li_{7-x}La_3Ta_xZr_{2-x}O_{12}$ materials

Figure 3.9 shows the conductivity curve of $Li_{6.25}La_3Ta_{0.25}Zr_{1.75}O_{12}$ before measurement of the activation energy, while Figure 3.10 and Figure 3.11 show the activation energy plots between 34 °C and 136 °C and the corresponding evaluation. Observation of Figure 3.10 indicates two semi-circles where the second one is superposed on the Li^+ blocking gold electrode.

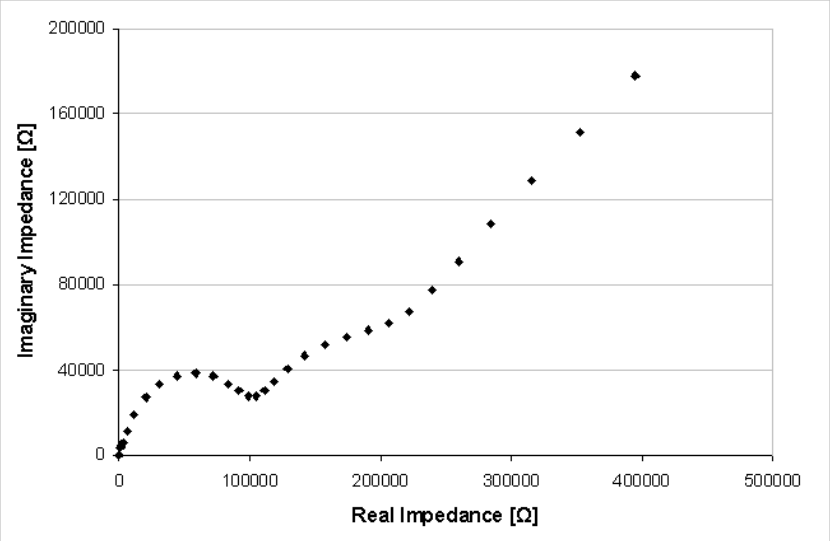

Fig.3.9: Impedance plot for conductivity measurement of $Li_{6.25}La_3Ta_{0.25}Zr_{1.75}O_{12}$ (thick pellet) at room temperature before measurement of activation energy

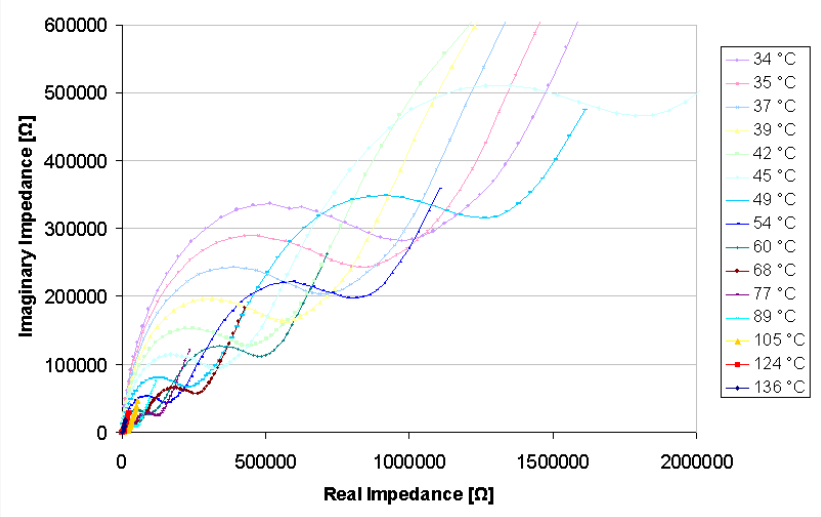

Fig.3.10: Impedance plot for activation energy measurement of $Li_{6.25}La_3Ta_{0.25}Zr_{1.75}O_{12}$ (thick pellet) between 34 °C and 136 °C

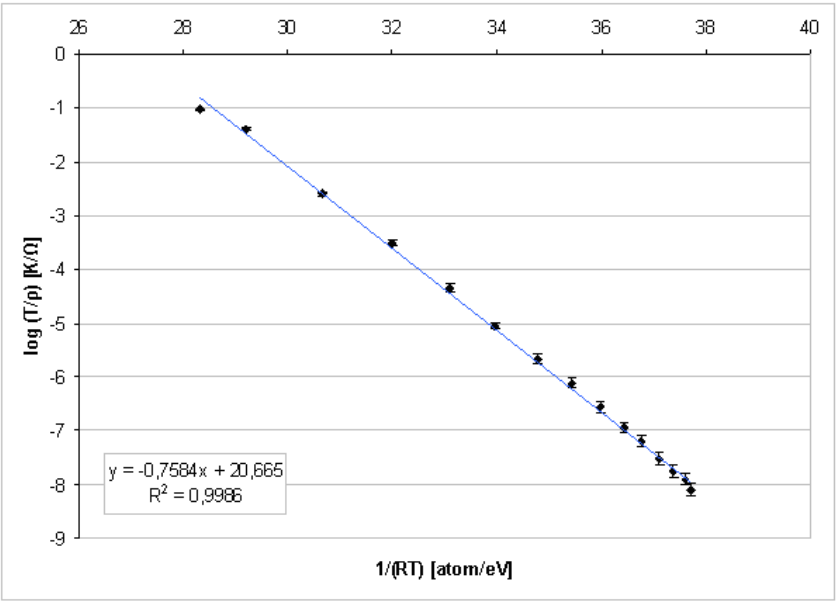

Fig.3.11: Arrhenius plot of log(T/ρ) vs. 1/(RT) of $Li_{6.25}La_3Ta_{0.25}Zr_{1.75}O_{12}$ *(thick pellet) between 34 °C and 136 °C. The slope of the line contains the activation energy*

Investigation of $Li_{6.25}La_3Ta_{0.25}Zr_{1.75}O_{12}$ (thick pellet) by light microscopy and SEM showed that the sample was very homogenous, shown in Figures 3.12 and 3.13.

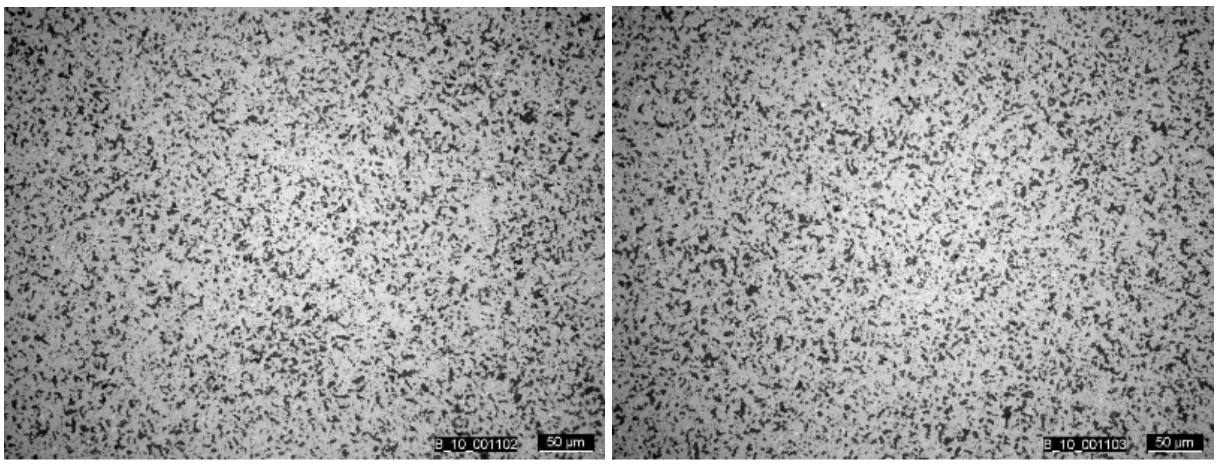

Fig.3.12: Microstructural investigation of $Li_{6.25}La_3Ta_{0.25}Zr_{1.75}O_{12}$ *(thick pellet) by light microscopy. Left picture: edge, Right picture: middle.*

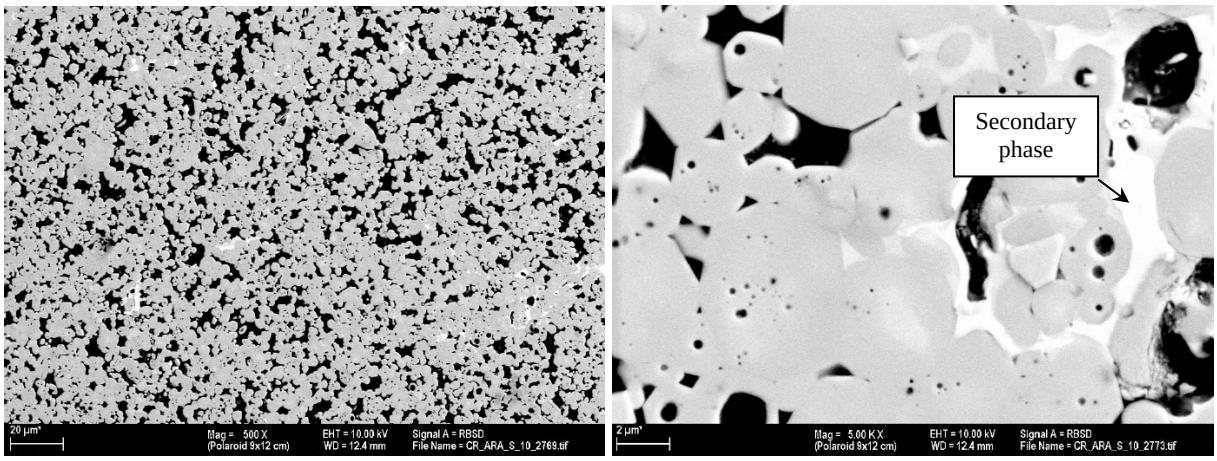

Fig.3.13: Microstructural investigation of $Li_{6.25}La_3Ta_{0.25}Zr_{1.75}O_{12}$ *(thick pellet-middle) by SEM*

After EDS investigation it was confirmed that a secondary phase (white region in right Figure 3.12) was a lanthanum and oxygen containing phase. As seen for $Li_7La_3Zr_2O_{12}$ the grains have an angular shape but contain small round pores.

Materialographic investigation of $Li_{6.5}La_3Ta_{0.5}Zr_{1.5}O_{12}$ and $Li_6La_3TaZrO_{12}$ (see Fig. 6.36., 6.37, 6.38 and 6.39 Chapter 6.2) indicated that $Li_{6.5}La_3Ta_{0.5}Zr_{1.5}O_{12}$ had a low density, no secondary phases and angular grains, while $Li_6La_3TaZrO_{12}$ consisted of two phases, where one phase had no Zr inside the grains. Dark gray regions in $Li_6La_3TaZrO_{12}$ are due to epoxy resin and are thus no further secondary phase. Light microscopy confirmed that $Li_5La_3Ta_2O_{12}$ (see Fig. 6.40, Chapter 6.2) was very homogeneous and dense.

$Li_{6.5}La_3Ta_{0.5}Zr_{1.5}O_{12}$ was investigated by neutron diffraction in Garching – Munich (see Figure 3.14). After applying Rietveld refinement, the following atom positions for Li could be found.

Li(1) occupies the 24d position, which corresponds to the tetrahedral site, with a probability of 0.48(2), while Li(3), sitting on one of the two 96h positions, corresponding to the distorted octahedral sites, has an occupation probability of 0.39(1). Only one of these two possible 96h positions can be occupied and thus the occupation probability has to be multiplied by two, which gives an occupation probability of 0.78(2) for the octahedral site. Hence the correct stoichiometric formula is $Li_{6.07}La_3Ta_{0.5}Zr_{1.5}O_{12}$. The deficiency of lithium can be ascribed to the presence of 2.5 wt% Li_2CO_3, which impoverishes the lithium content of the garnet phase.

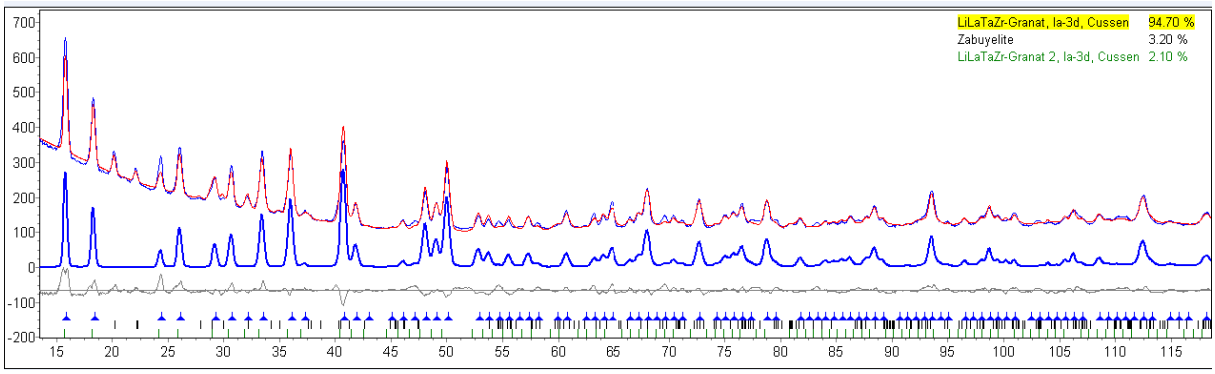

Fig.3.14: Fitted neutron diffraction pattern of $Li_{6.5}La_3Ta_{0.5}Zr_{1.5}O_{12}$

3.3. $Li_{7-x+y}Ca_yLa_{3-y}Ta_xZr_{2-x}O_{12}$ garnet materials

Two samples, replacing calcium for strontium and tantalum for zirconium were prepared with a phase purity of 100%, having different weights. The Tables 3.5 and 3.6 contain the structural and electrical characterizations of the materials.

The more calcium and tantalum is in the sample, the smaller is the lattice parameter. This corresponds to the fact that the ionic radii of calcium and tantalum are smaller than those of lanthanum and zirconium. The low density of $Li_{6.75}Ca_{0.25}La_{1.75}Ta_{0.5}Zr_{1.5}O_{12}$ correlates with the low shrinkage during the sintering process.

Figure 3.15 gives the conductivity curve of $Li_{6.25}La_3Ta_{0.25}Zr_{1.75}O_{12}$ before measurement of the activation energy.

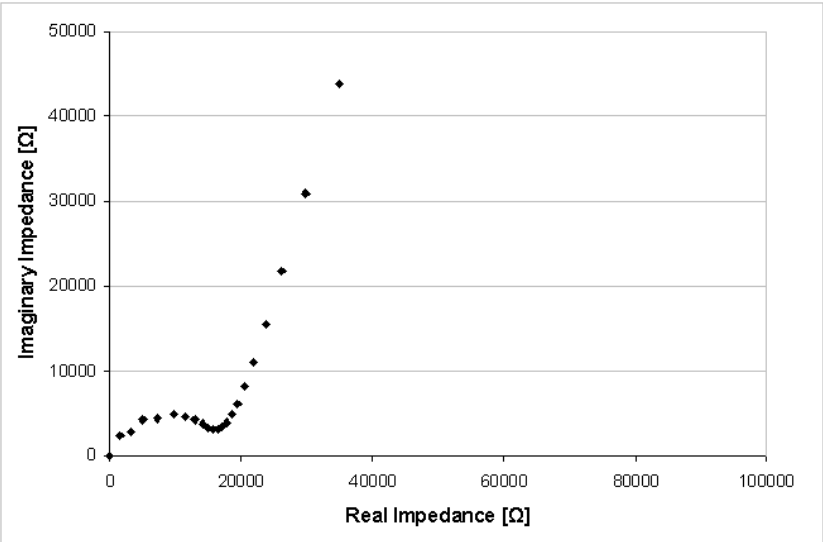

Fig. 3.15: Impedance plot for conductivity measurement of $Li_{6.5}Ca_{05}La_{1.75}TaZrO_{12}$ *(thick pellet) at room temperature before measurement of activation energy*

Composition	Mass [g]	Lattice parameter powder [Å]	Lattice parameter pellet [Å]	Cubic garnet [%]	Secondary phases	Density [%]	Shrinkage [%]	Weight loss [%]
$Li_{6.75}Ca_{0.25}La_{2.75}Ta_{0.5}Zr_{1.5}O_{12}$	0.7294	12.989(0)	12.942(5)	100	-	61	19.72	12.13
$Li_{6.75}Ca_{0.25}La_{2.75}Ta_{0.5}Zr_{1.5}O_{12}$	0.4437	12.989(0)	12.943(5)	100	-	60	12.24	14.27
$Li_{6.5}Ca_{0.5}La_{2.5}TaZrO_{12}$	0.7481	12.868(2)	12.866(3)	100	-	85	37.42	6.31
$Li_{6.5}Ca_{0.5}La_{2.5}TaZrO_{12}$	0.5351	12.868(2)	12.867(6)	100	-	78	40.38	11.65

Tab.3.5.: Structural properties of $Li_{7-x+y}Ca_yLa_{3-y}Ta_xZr_{2-x}O_{12}$ *materials*

Sample name	σ before E_A measurement [S·cm^{-1}]	Number of semi-circles	σ after E_A measurement [S·cm^{-1}]	Activation energy [eV]	R-value of trend line
$Li_{6.75}Ca_{0.25}La_{2.75}Ta_{0.5}Zr_{1.5}O_{12}$_thick	$7.85\cdot10^{-6}$	2	$7.85\cdot10^{-8}$	0.85	0.999
$Li_{6.75}Ca_{0.25}La_{2.75}Ta_{0.5}Zr_{1.5}O_{12}$_thin(2)	$8.74\cdot10^{-6}$	2	$9.39\cdot10^{-8}$	0.82	0.999
$Li_{6.5}Ca_{0.5}La_{2.5}TaZrO_{12}$_thick	$7.55\cdot10^{-5}$	1	$3.38\cdot10^{-6}$	0.67	0.999
$Li_{6.5}Ca_{0.5}La_{2.5}TaZrO_{12}$_thin	$3.85\cdot10^{-5}$	1	$3.30\cdot10^{-5}$	0.51	0.991

Tab.3.6.: Electrical properties of $Li_{7-x+y}Ca_yLa_{3-y}Ta_xZr_{2-x}O_{12}$ *materials*

Figures 3.16 and 3.17 show the activation energy plots between 34 °C and 136 °C and the corresponding evaluation.

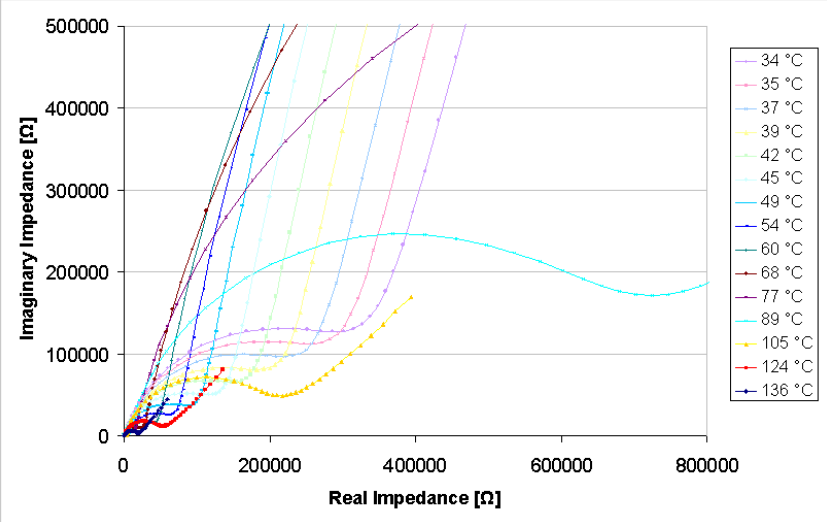

Fig.3.16: Impedance plot for activation energy measurement of $Li_{6.5}Ca_{05}La_{1.75}TaZrO_{12}$ *(thick pellet) between 34 °C and 136 °C*

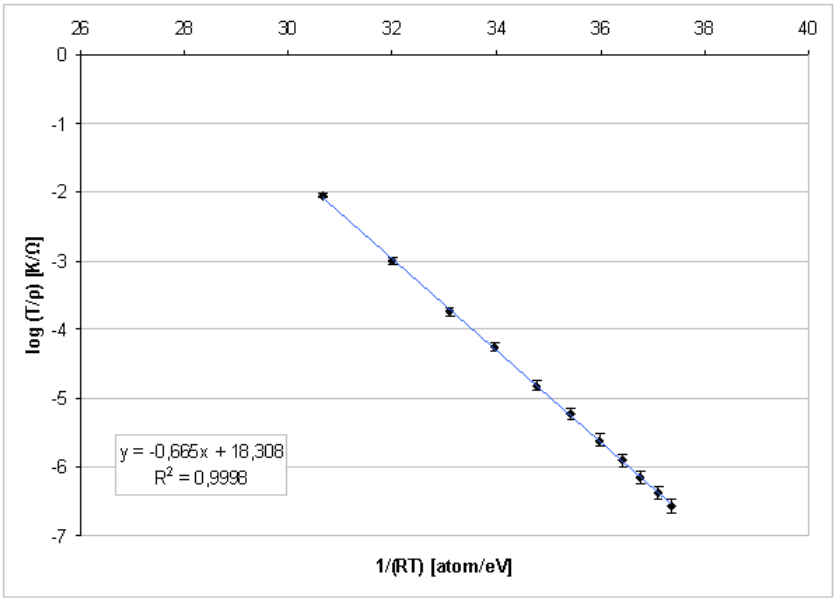

Fig.3.17: Arrhenius plot of log(T/ρ) vs. 1/(RT) of $Li_{6.5}Ca_{05}La_{1.75}TaZrO_{12}$ *(thick pellet) between 34 °C and 136 °C. The slope of the line contains the activation energy*

Investigation by light microscopy and SEM showed that there were two different regions inside the pellet. Figures 3.18 and 3.19 give the microstructure of the different regions with varying magnifications of $Li_{6.5}Ca_{0.5}La_{2.5}TaZrO_{12}$ (thick pellet). From the SEM pictures it can be seen, that the material is very homogenous, has a high density at the upper edge of the

sample and contains only low amounts of a secondary phase, which is poor in lanthanum. This secondary phase was not detectable by XRD, because its total amount is below the detection limit. There are hardly any pores inside the angular grains.

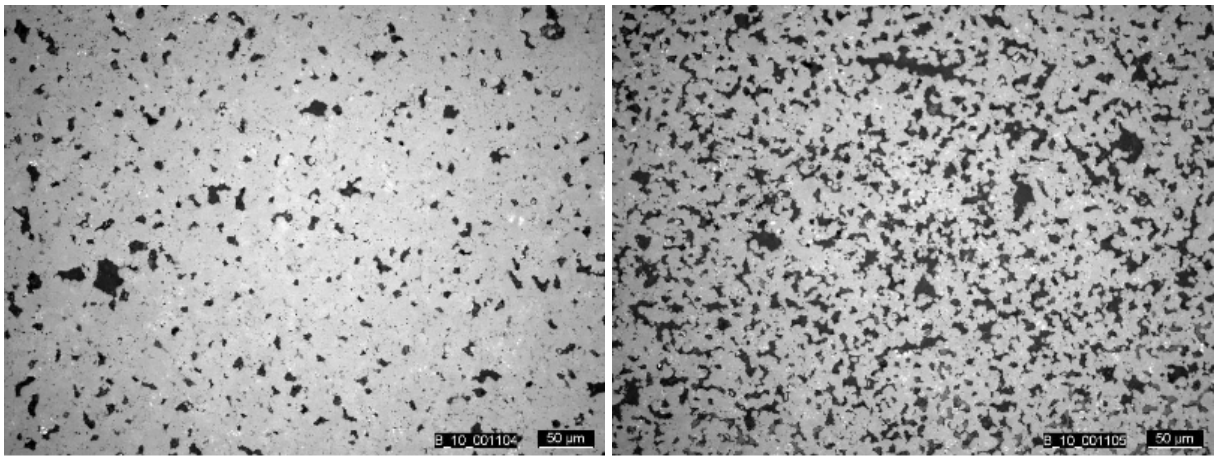

Fig.3.18: Microstructural investigation of $Li_{6.5}Ca_{0.5}La_{2.5}TaZrO_{12}$ (thick pellet) by light microscopy.

Left picture: upper edge, Right picture: lower edge.

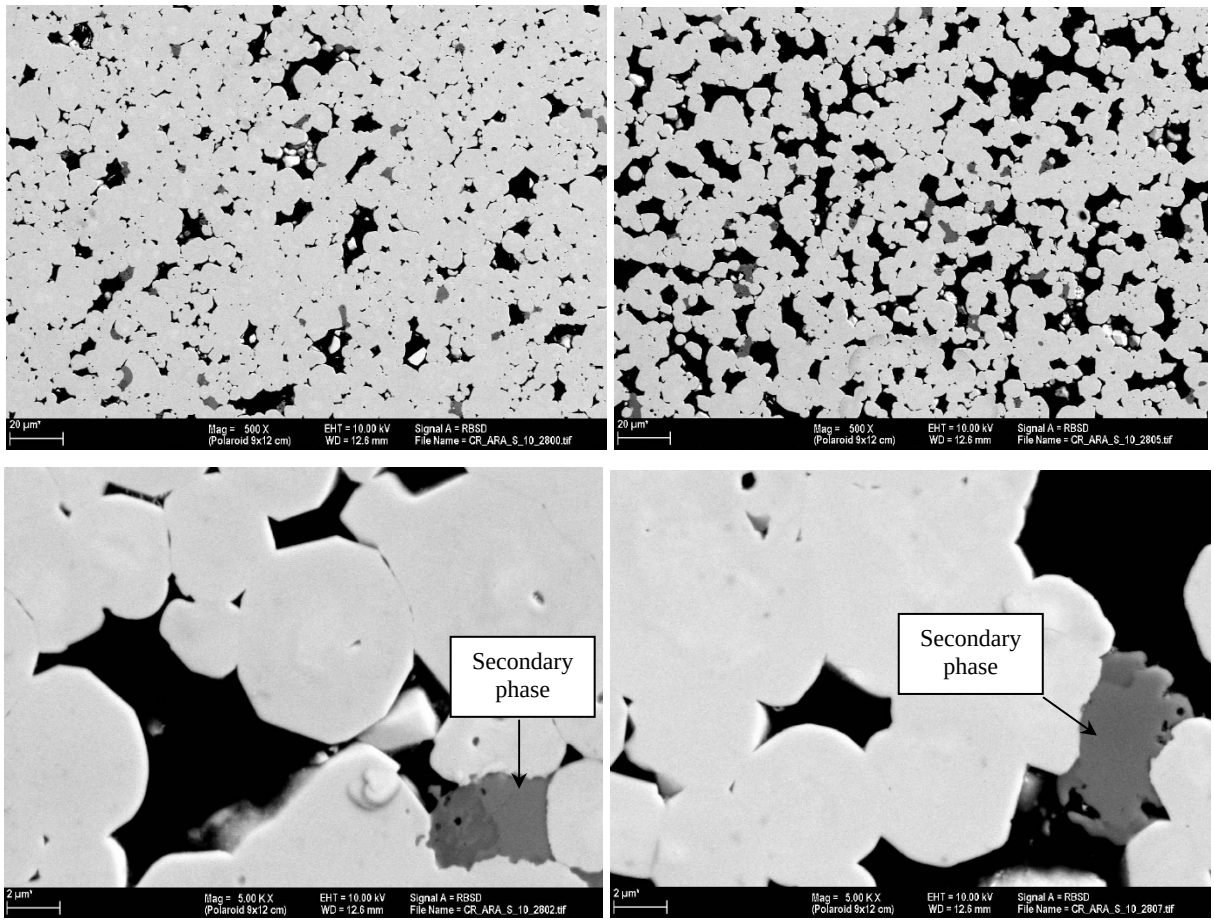

Fig.3.19: Microstructural investigation of $Li_{6.5}Ca_{0.5}La_{2.5}TaZrO_{12}$ (thick pellet) by SEM.

Left pictures: upper edge, Right pictures: lower edge

3.4. $Li_{7-x+y}Sr_yLa_{3-y}Ta_xZr_{2-x}O_{12}$ garnet materials

Seven compositions with substitution of strontium for lanthanum have been produced. Two pellets of each composition having different weights were investigated. Tables 3.7 and 3.8 include structural and electrical properties of the samples. Except for $Li_{6.5}Sr_{0.5}La_{2.5}TaZrO_{12}$ the pellets could be produced phase pure after sintering. It is rather surprising that the lattice parameters decrease after sintering.

Figure 3.20 shows the development of the lattice parameters in dependence on the strontium content at constant tantalum contents.

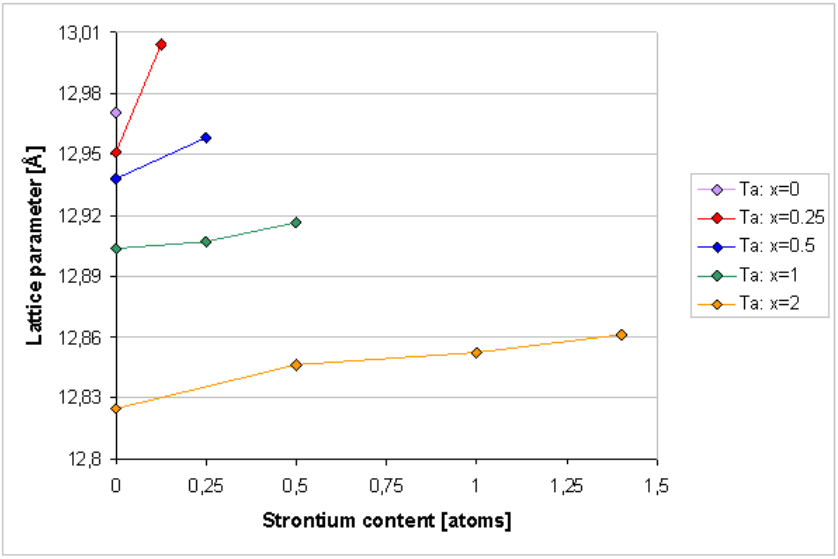

Fig. 3.20: Development of the lattice parameter with different strontium and tantalum contents

It can be seen that the lattice parameter is increasing with increasing strontium content within constant tantalum contents.

For most of the samples, the volume shrinkage is around 30 % which leads to quite high densities between 80 % and 90 %. With the exception of $Li_{6.75}Sr_{0.25}La_{2.75}Ta_{0.5}Zr_{1.5}O_{12}$ and $Li_{6.4}Sr_{1.4}La_{1.6}Ta_2O_{12}$ the activation energies for the thick and the thin pellet of the same composition are comparable.

Composition	Mass [g]	Lattice parameter powder [Å]	Lattice parameter pellet [Å]	Cubic garnet [%]	Secondary phases	Density [%]	Shrinkage [%]	Weight loss [%]
$Li_{6.875}Sr_{0.125}La_{2.875}Ta_{0.25}Zr_{1.5}O_{12}$	0.7866	13.003(8)	12.991(2)	98	2% $Li_2Zr_2O_3$	83	32.41	4.92
$Li_{6.875}Sr_{0.125}La_{2.875}Ta_{0.25}Zr_{1.5}O_{12}$	0.5050	13.003(8)	12.974(3)	100	-	65	16.89	7.80
$Li_{6.75}Sr_{0.25}La_{2.75}Ta_{0.5}Zr_{1.5}O_{12}$	0.7163	12.957(9)	12.946(8)	100	-	57	42.12	10.18
$Li_{6.75}Sr_{0.25}La_{2.75}Ta_{0.5}Zr_{1.5}O_{12}$	0.5332	12.957(9)	12.946(7)	100	-	58	13.12	15.98
$Li_{6.75}Sr_{0.25}La_{2.75}Ta_{0.5}Zr_{1.5}O_{12}$	0.7163	12.957(9)	12.946(5)	100	-	88	42.12	10.18
$Li_{6.25}Sr_{0.25}La_{2.75}TaZrO_{12}$	0.7577	12.906(9)	12.907(4)	98	2% $SrZrO_3$	56	2.00	10.08
$Li_{6.25}Sr_{0.25}La_{2.75}TaZrO_{12}$	0.4955	12.906(9)	12.909(6)	100	-	56	2.21	10.15
$Li_{6.5}Sr_{0.5}La_{2.5}TaZrO_{12}$	0.7550	12.916(6)	12.886(6)	96	4% $SrZrO_3$	60	7.32	11.73
$Li_{6.5}Sr_{0.5}La_{2.5}TaZrO_{12}$	0.4791	12.916(6)	12.886(2)	96	4% $SrZrO_3$	58	5.87	11.56
$Li_{5.5}Sr_{0.5}La_{2.5}Ta_2O_{12}$	0.6949	12.846(6)	12.850(2)	100	-	81	31.75	11.38
$Li_{5.5}Sr_{0.5}La_{2.5}Ta_2O_{12}$	0.5202	12.846(6)	12.823(3)	100	-	78	31.58	9.57
$Li_6SrLa_2Ta_2O_{12}$	0.7248	12.852(6)	12.840(9)	100	-	83	30.70	4.96
$Li_6SrLa_2Ta_2O_{12}$	0.5298	12.852(6)	12.841(8)	100	-	82	30.27	5.15
$Li_{6.4}Sr_{1.4}La_{1.6}Ta_2O_{12}$	0.7164	12.861(5)	12.857(9)	100	-	76	23.30	8.26
$Li_{6.4}Sr_{1.4}La_{1.6}Ta_2O_{12}$	0.5172	12.861(5)	12.864(1)	100	-	89	36.82	8.24

Tab.3.7.: Structural properties of $Li_{7-x+y}Sr_yLa_{3-y}Ta_xZr_{2-x}O_{12}$ *materials*

Sample name	σ before E_A measurement [S·cm^{-1}]	Number of semi-circles	σ after E_A measurement [S·cm^{-1}]	Activation energy [eV]	R-value of trend line
$Li_{6.875}Sr_{0.125}La_{2.875}Ta_{0.25}Zr_{1.5}O_{12}$_thick	$1.94 \cdot 10^{-5}$	2	$8.11 \cdot 10^{-7}$	0.79	0.999
$Li_{6.875}Sr_{0.125}La_{2.875}Ta_{0.25}Zr_{1.5}O_{12}$_thin	$6.59 \cdot 10^{-6}$	2	$4.49 \cdot 10^{-8}$	0.85	0.999
$Li_{6.75}Sr_{0.25}La_{2.75}Ta_{0.5}Zr_{1.5}O_{12}$_thick	$2.47 \cdot 10^{-6}$	2	$6.92 \cdot 10^{-7}$	0.64	0.999
$Li_{6.75}Sr_{0.25}La_{2.75}Ta_{0.5}Zr_{1.5}O_{12}$_thin(2)	$5.67 \cdot 10^{-8}$	1	$4.62 \cdot 10^{-8}$	0.82	0.991
$Li_{6.75}Sr_{0.25}La_{2.75}Ta_{0.5}Zr_{1.5}O_{12}$_thick(2)	$2.67 \cdot 10^{-4}$	1	$3.20 \cdot 10^{-4}$	0.42	0.997
$Li_{6.25}Sr_{0.25}La_{2.75}TaZrO_{12}$_thick	$2.22 \cdot 10^{-6}$	1	$2.71 \cdot 10^{-10}$	1.1	0.989
$Li_{6.25}Sr_{0.25}La_{2.75}TaZrO_{12}$_thin	-	-	-	-	-
$Li_{6.5}Sr_{0.5}La_{2.5}TaZrO_{12}$_thick	$1.43 \cdot 10^{-5}$	2	$4.24 \cdot 10^{-7}$	0.73	0.999
$Li_{6.5}Sr_{0.5}La_{2.5}TaZrO_{12}$_thin	$6.55 \cdot 10^{-6}$	2	$9.58 \cdot 10^{-8}$	0.73	0.999
$Li_{5.5}Sr_{0.5}La_{2.5}Ta_2O_{12}$_thick(2)	$5.51 \cdot 10^{-5}$	1	$1.37 \cdot 10^{-5}$	0.59	0.999
$Li_{5.5}Sr_{0.5}La_{2.5}Ta_2O_{12}$_thin(2)	$2.56 \cdot 10^{-5}$	1	$8.88 \cdot 10^{-6}$	0.59	0.998
$Li_6SrLa_2Ta_2O_{12}$_thick	$4.20 \cdot 10^{-5}$	1	$1.42 \cdot 10^{-6}$	0.69	0.999
$Li_6SrLa_2Ta_2O_{12}$_thin	$2.88 \cdot 10^{-5}$	1	$2.09 \cdot 10^{-6}$	0.70	0.999
$Li_{6.4}Sr_{1.4}La_{1.6}Ta_2O_{12}$_thick	$4.19 \cdot 10^{-5}$	1	$2.92 \cdot 10^{-7}$	0.74	0.998
$Li_{6.4}Sr_{1.4}La_{1.6}Ta_2O_{12}$_thin(2)	$3.82 \cdot 10^{-5}$	1	$5.73 \cdot 10^{-6}$	0.53	0.999

Tab.3.8.: Electrical properties of $Li_{7-x+y}Sr_yLa_{3-y}Ta_xZr_{2-x}O_{12}$ materials

Figure 3.21 depicts the conductivity curve of $Li_{6.75}Sr_{0.25}La_{2.75}Ta_{0.5}Zr_{1.5}O_{12}$ before measurement of the activation energy.

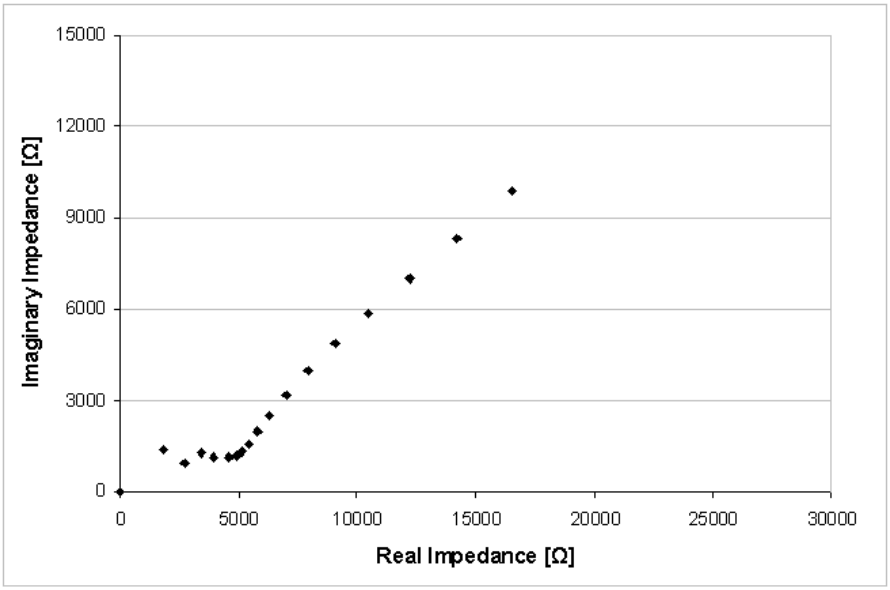

Fig.3.21: Impedance plot for conductivity measurement of $Li_{6.75}Sr_{0.25}La_{2.75}Ta_{0.5}Zr_{1.5}O_{12}$ (thick pellet) at room temperature before measurement of activation energy

Figure 3.22 and 3.23 show the corresponding activation energy plots between 34 °C and 136 °C and their evaluation.

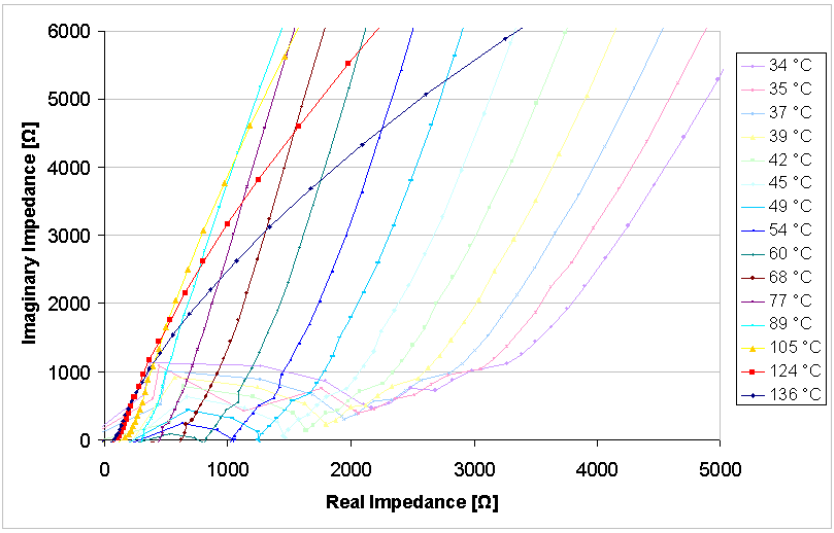

Fig.3.22: Impedance plot for activation energy measurement of $Li_{6.75}Sr_{0.25}La_{2.75}Ta_{0.5}Zr_{1.5}O_{12}$ (thick pellet) between 34 °C and 136 °C

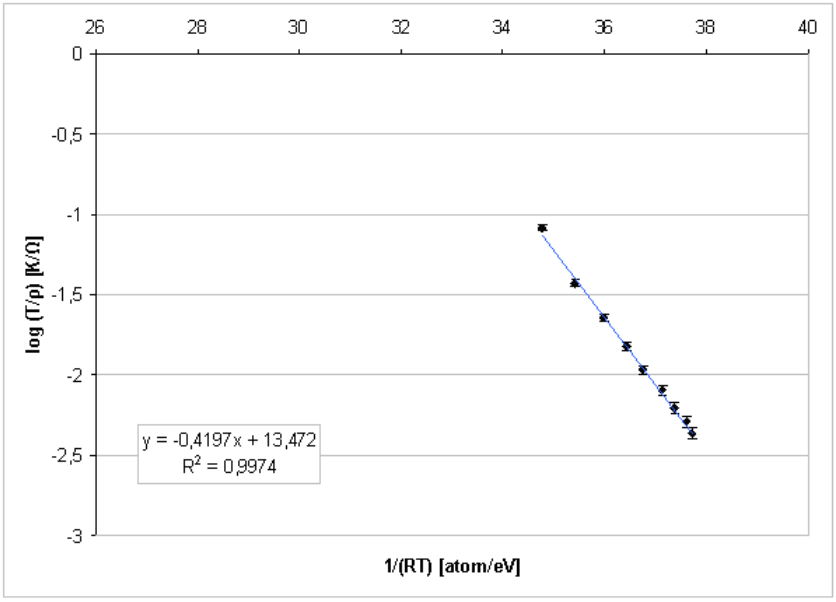

Fig.3.23: Arrhenius plot of log(T/ρ) vs. 1/(RT) of $Li_{6.75}Sr_{0.25}La_{2.75}Ta_{0.5}Zr_{1.5}O_{12}$ *(thick pellet) between 34 °C and 136 °C. The slope of the line contains the activation energy*

On closer inspection of $Li_{6.5}Sr_{0.5}La_{2.5}TaZrO_{12}$ by light microscopy it can be seen that the pellet is not dense, has a high porosity and partially large holes, but is homogenous (see Fig. 3.24). EDS analysis showed that the nearly totally round grains contained two phases inside the grain and a third secondary phase, which formed angular particles, as can be seen in Fig. 3.25. The third secondary phase contains Sr, La, O and hardly any Ta, while the main phase consists of a Sr, La, Ta, Zr-containing phase and a phase poor in La.

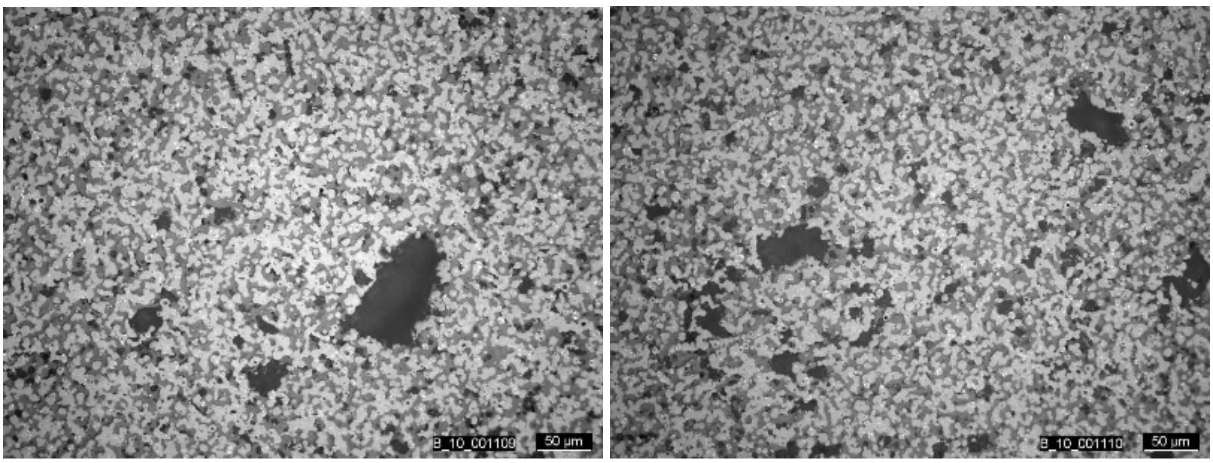

Fig.3.24: Microstructural investigation of $Li_{6.5}Sr_{0.5}La_{2.5}TaZrO_{12}$ *(thick pellet) by light microscopy. Left picture: edge, Right picture: middle*

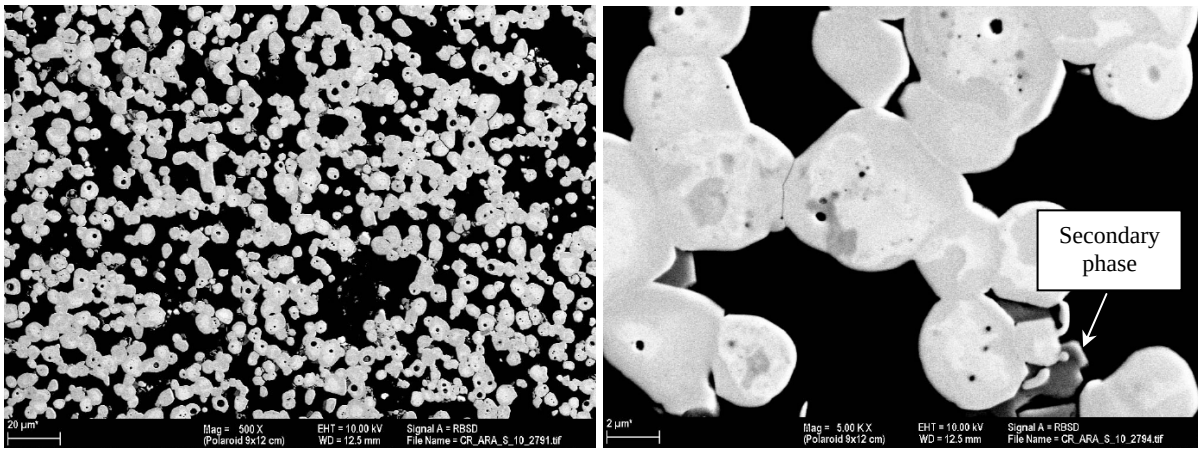

Fig.3.25: Microstructural investigation of $Li_{6.5}Sr_{0.5}La_{2.5}xTaZrO_{12}$ *(thick pellet-middle) by SEM*

Furthermore $Li_{6.75}Sr_{0.25}La_{2.5}Ta_{0.5}Zr_{1.5}O_{12}$, $Li_{5.5}Sr_{0.5}La_{2.5}Ta_2O_{12}$, $Li_6SrLa_2Ta_2O_{12}$ and $Li_{6.4}Sr_{1.4}La_{1.6}Ta_2O_{12}$ were investigated by light microscopy. $Li_{6.75}Sr_{0.25}La_{2.5}Ta_{0.5}Zr_{1.5}O_{12}$ in Fig. 6.41 (Chapter 6.2.) shows that the bright regions form a two-phase acicular shape of sintered grains with a secondary phase. $Li_{5.5}Sr_{0.5}La_{2.5}Ta_2O_{12}$ (Fig.6.42, Chapter 6.2) is an inhomogeneous phase pure material. White stains are due to subjacent pores, which create reflections when illuminating the sample with the light source of the microscope, while dark gray areas are formed by epoxy resin. $Li_6SrLa_2Ta_2O_{12}$ (Fig.6.43, Chapter 6.2) is a more than 80 % dense homogenous material having huge crystals up to 50 µm and unsymmetrical pores. $Li_{6.4}Sr_{1.4}La_{1.6}Ta_2O_{12}$ (Fig.6.44, Chapter 6.2) has a high porosity and is only sintered at the edge of the sample. Exaggerated grains of a dimension up to 100 µm appear, with lacerated grain boundary shapes.

3.5. $Li_{7-x+y}Ba_yLa_{3-y}Ta_xZr_{2-x}O_{12}$ garnet materials

Samples with eight different compositions and two different weights have been produced and investigated. The Tables 3.9 and 3.10 summarize their structural and electrical properties. Beside $Li_{5.5}Ba_{0.5}La_{2.5}Ta_2O_{12}$ and $Li_6BaLa_2Ta_2O_{12}$ non of the compositions could be produced with a phase purity of 100 % but they show secondary phases such as $BaZrO_3$, La_2O_3, $La_2Zr_2O_7$, $BaCO_3$, Li_2CO_3 and $Ba_2Ta_2O_7$. As already observed in previous chapters, the lattice parameters show a drastic decrease after sintering and low densities correspond to low volume shrinkage. For $Li_{6.25}Ba_{1.25}La_{1.75}Ta_2O_{12}$ it was not possible to determine the density, the shrinkage, the weight loss and the electrical properties, because a

Composition	Mass [g]	Lattice parameter powder [Å]	Lattice parameter pellet [Å]	Cubic garnet [%]	Secondary phases	Density [%]	Shrinkage [%]	Weight loss [%]
$Li_{6.875}Ba_{0.125}La_{2.875}Ta_{0.25}Zr_{1.75}O_{12}$	0.7544	12.984(2)	12.979(6)	97	2.2%$BaZrO_3$ 0.8% La_2O_3	79	29.27	5.02
$Li_{6.875}Ba_{0.125}La_{2.875}Ta_{0.25}Zr_{1.75}O_{12}$	0.5474	12.984(2)	12.986(5)	96	3.2% $BaZrO_3$ 1.34% La_2O_3	66	15.27	5.04
$Li_{6.75}Ba_{0.25}La_{2.75}Ta_{0.5}Zr_{1.5}O_{12}$	0.7247	12.975(7)	12.939(9)	89	11% $BaZrO_3$	69	22.67	11.91
$Li_{6.75}Ba_{0.25}La_{2.75}Ta_{0.5}Zr_{1.5}O_{12}$	0.5363	12.975(7)	12.940(9)	90	10% $BaZrO_3$	61	12.76	12.83
$Li_{6.25}Ba_{0.25}La_{2.75}TaZrO_{12}$	0.7140	12.952(8)	12.898(2)	91	2.8% $La_2Zr_2O_7$ 2.4%$BaCO_3$ 3.8%$BaZrO_3$	62	13.16	10.27
$Li_{6.25}Ba_{0.25}La_{2.75}TaZrO_{12}$	0.5338	12.952(8)	12.899(5)	94	2.5% $BaCO_3$ 3.5% $BaZrO_3$	56	5.88	7.34
$Li_{6.5}Ba_{0.5}La_{2.5}TaZrO_{12}$	0.8153	12.973(4)	12.899(8)	74	1.5% $BaCO_3$ 8.7% $BaZrO_3$ 15.8% Li_2CO_3	79	25.93	6.14
$Li_{6.5}Ba_{0.5}La_{2.5}TaZrO_{12}$	0.5230	12.973(4)	12.902(5)	79	1.1% $BaCO_3$ 10.3% $BaZrO_3$ 9.6% Li_2CO_3	80	25.78	6.16
$Li_{5.5}Ba_{0.5}La_{2.5}Ta_2O_{12}$	0.7219	12.915(5)	12.888(8)	100	-	83	28.55	4.84
$Li_{5.5}Ba_{0.5}La_{2.5}Ta_2O_{12}$	0.4981	12.915(5)	12.888(3)	100	-	80	25.03	5.72
$Li_6BaLa_2Ta_2O_{12}$	0.7206	12.982(3)	12.890(4)	100	-	87	33.88	13.02
$Li_6BaLa_2Ta_2O_{12}$	0.5159	12.982(3)	12.886(5)	99	1% La_2O_3	90	32.77	12.83
$Li_{6.25}Ba_{1.25}La_{1.75}Ta_2O_{12}$	0.6875	13.062(0)	12.925(7)	88	4.3% $BaCO_3$ 7.7% $Ba_2Ta_2O_7$	-	-	-
$Li_{6.25}Ba_{1.25}La_{1.75}Ta_2O_{12}$	0.5291	13.062(0)	12.922(1)	93	2.5% $BaCO_3$ 4.5% La_2O_3	-	-	-
$Li_{6.4}Ba_{1.4}La_{1.6}Ta_2O_{12}$	0.6889	13.065(2)	12.932(9)	55	3.7% $BaCO_3$ 18.8% $Ba_2Ta_2O_7$ 6.3% La_2O_3 16.2% Li_2CO_3	81	32.03	15.31
$Li_{6.4}Ba_{1.4}La_{1.6}Ta_2O_{12}$	0.4763	13.065(2)	12.933(8)	58	4.9% $BaCO_3$ 16.4% $Ba_2Ta_2O_7$ 7.4% La_2O_3 13.3% Li_2CO_3	84	32.42	14.40

Tab.3.9.: Structural properties of $Li_{7-x+y}Ba_yLa_{3-y}Ta_xZr_{2-x}O_{12}$ materials

Sample name	σ before E_A measurement [S·cm^{-1}]	Number of semi-circles	σ after E_A measurement [S·cm^{-1}]	Activation energy [eV]	R-value of trend line
$Li_{6.875}Ba_{0.125}La_{2.875}Ta_{0.25}Zr_{1.75}O_{12}$_thick	$7.68 \cdot 10^{-5}$	1	$2.92 \cdot 10^{-7}$	0.84	0.999
$Li_{6.875}Ba_{0.125}La_{2.875}Ta_{0.25}Zr_{1.75}O_{12}$_thin	$>10^{-8}$ *	- *	$>10^{-10}$ *	1.00	0.999
$Li_{6.75}Ba_{0.25}La_{2.75}Ta_{0.5}Zr_{1.5}O_{12}$_thick	-	-	-	-	-
$Li_{6.75}Ba_{0.25}La_{2.75}Ta_{0.5}Zr_{1.5}O_{12}$_thin	-	-	-	-	-
$Li_{6.25}Ba_{0.25}La_{2.75}TaZrO_{12}$_thick	-	- *	$2.98 \cdot 10^{-6}$	0.66	0.999
$Li_{6.25}Ba_{0.25}La_{2.75}TaZrO_{12}$_thin	$2.41 \cdot 10^{-6}$	- *	$1.30 \cdot 10^{-8}$	0.89	0.999
$Li_{6.5}Ba_{0.5}La_{2.5}TaZrO_{12}$_thick	$4.95 \cdot 10^{-6}$	1	$2.11 \cdot 10^{-5}$	0.74	0.999
$Li_{6.5}Ba_{0.5}La_{2.5}TaZrO_{12}$_thin	$3.60 \cdot 10^{-7}$	1	$2.21 \cdot 10^{-8}$	0.85	0.999
$Li_{5.5}Ba_{0.5}La_{2.5}Ta_2O_{12}$_thick	$5.72 \cdot 10^{-5}$	1	$4.60 \cdot 10^{-5}$	0.56	0.999
$Li_{5.5}Ba_{0.5}La_{2.5}Ta_2O_{12}$_thin	$3.16 \cdot 10^{-5}$	1	$7.09 \cdot 10^{-7}$	0.73	0.999
$Li_6BaLa_2Ta_2O_{12}$_thick	$2.11 \cdot 10^{-5}$	1	$7.96 \cdot 10^{-6}$	0.64	0.999
$Li_6BaLa_2Ta_2O_{12}$_thin(2)	$1.47 \cdot 10^{-5}$	1	$4.21 \cdot 10^{-7}$	0.63	0.999
$Li_{6.25}Ba_{1.25}La_{1.75}Ta_2O_{12}$_thick	-	-	-	-	-
$Li_{6.25}Ba_{1.25}La_{1.75}Ta_2O_{12}$_thin	-	-	-	-	-
$Li_{6.4}Ba_{1.4}La_{1.6}Ta_2O_{12}$_thick	$6.83 \cdot 10^{-7}$	1	$2.62 \cdot 10^{-7}$	0.68	0.999
$Li_{6.4}Ba_{1.4}La_{1.6}Ta_2O_{12}$_thin	$2.61 \cdot 10^{-7}$	1	$3.33 \cdot 10^{-7}$	0.68	0.999

Tab.3.10.: Electrical properties of $Li_{7-x+y}Ba_yLa_{3-y}Ta_xZr_{2-x}O_{12}$ materials

* Sample was highly resistant and it was not possible to measure the conductivity because the region of ion-blocking tail was not reached until the end of the frequency range which is possible to measure.

foam-like structure was formed and the powder bed stuck on all sides of the sample. After a few days of storing $Li_{6.75}Ba_{0.25}La_{2.5}Ta_{0.5}Zr_{1.5}O_{12}$ on air, the samples decomposed and it was not possible to measure the electrical properties. The conductivities of the samples decrease strongly after measurement of the activation energy.

Figure 3.26 depicts the development of the lattice parameter at constant tantalum content and changing barium content. It can be seen that the lattice parameter increases with increasing barium content.

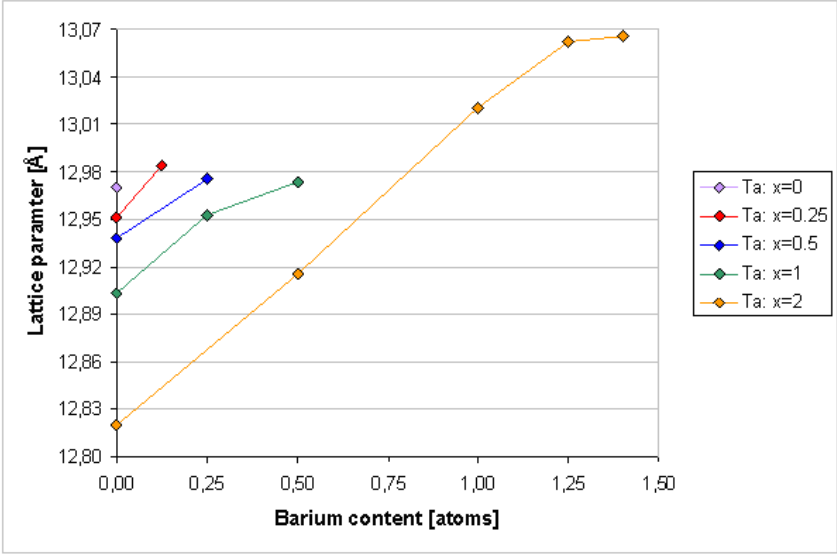

Fig.3.26: Development of the lattice parameter with different barium and tantalum contents

Figure 3.27 illustrates the impedance plot for the conductivity measurement before measurement of the activation energy of $Li_{5.5}Ba_{0.5}La_{2.5}Ta_2O_{12}$. Subsequently the Figures 3.28 and 3.29 show the activation energy plots between 34 °C and 136 °C and the corresponding evaluation.

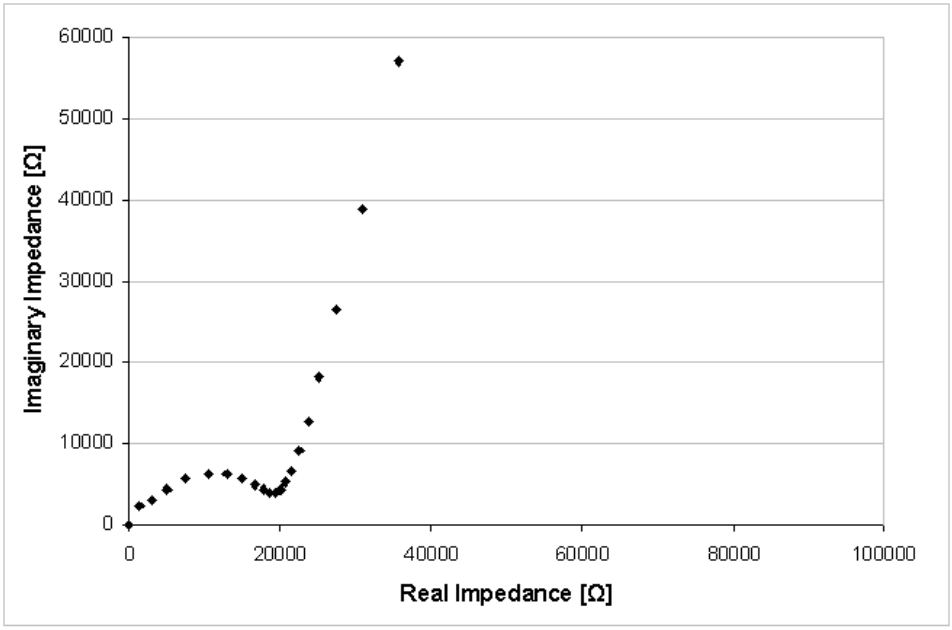

Fig.3.27: Impedance plot for conductivity measurement of $Li_{5.5}Ba_{0.5}La_{2.5}Ta_2O_{12}$ (thick pellet) at room temperature before measurement of activation energy

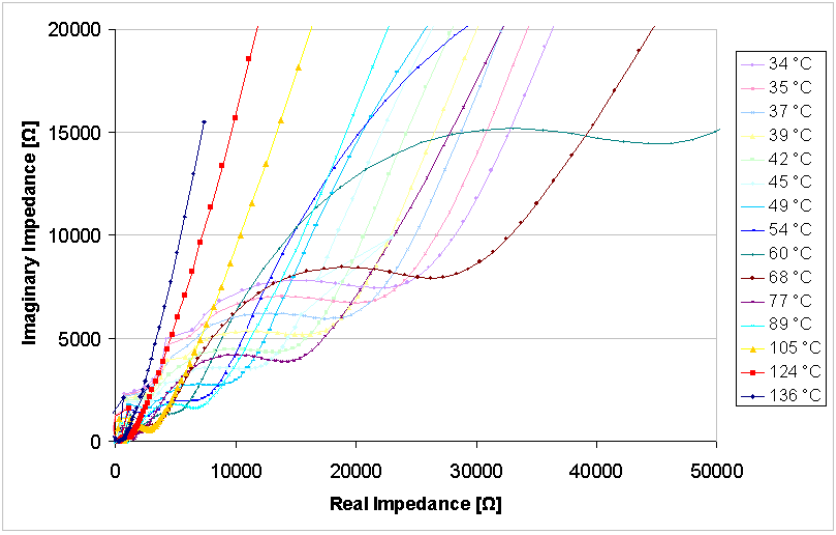

Fig. 3.28: Impedance plot for activation energy measurement of $Li_{5.5}Ba_{0.5}La_{2.5}Ta_2O_{12}$ (thick pellet) between 34 °C and 136 °C

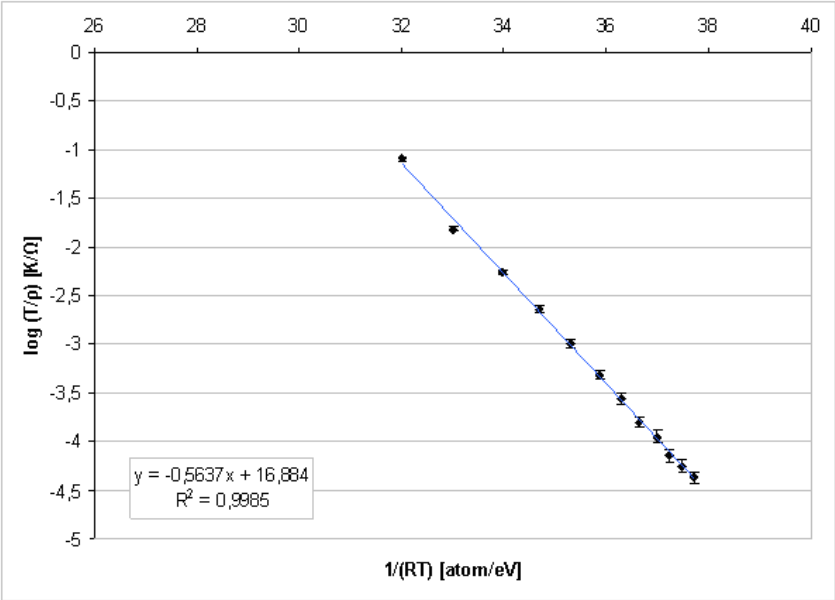

Fig.3.29: Arrhenius plot of log(T/ρ) vs. 1/(RT) of $Li_{5.5}Ba_{0.5}La_{2.5}Ta_2O_{12}$ *(thick pellet) between 34 °C and 136 °C. The slope of the line contains the activation energy*

Analysis of $Li_{5.5}Ba_{0.5}La_{2.5}Ta_2O_{12}$ (thick pellet) by light microscopy proves, that the pellet is homogenous and dense (see Figure 3.30). Investigation by SEM and EDS (Figure 3.31) showed that the grains exhibit an angular shape with small spherical pores and that the sample had only a low amount of a secondary phase. The secondary phase is a tantalum-poor and lanthanum-rich phase.

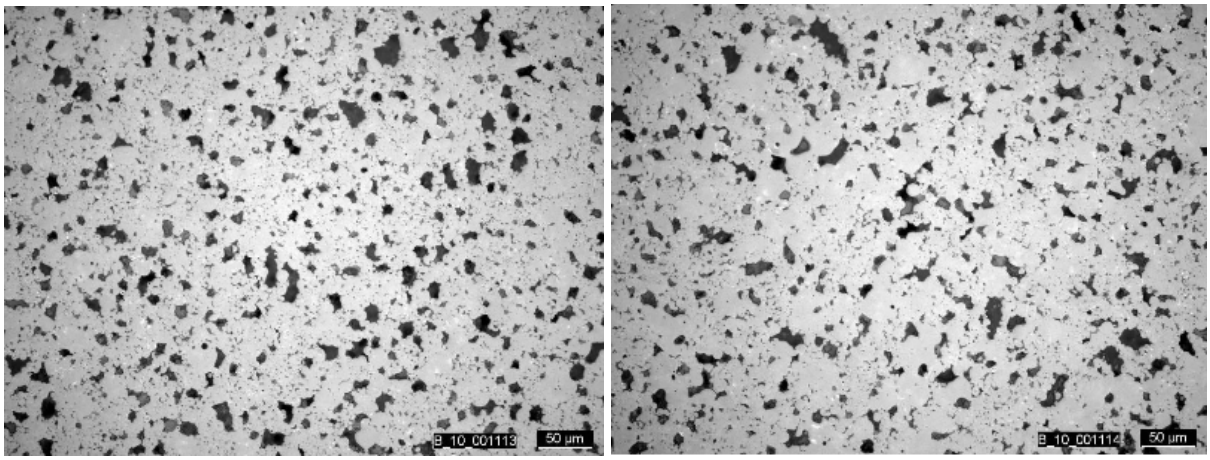

Fig.3.30: Microstructural investigation of $Li_{5.5}Ba_{0.5}La_{2.5}Ta_2O_{12}$ *(thick pellet) by light microscopy. Left picture: edge, Right picture: middle*

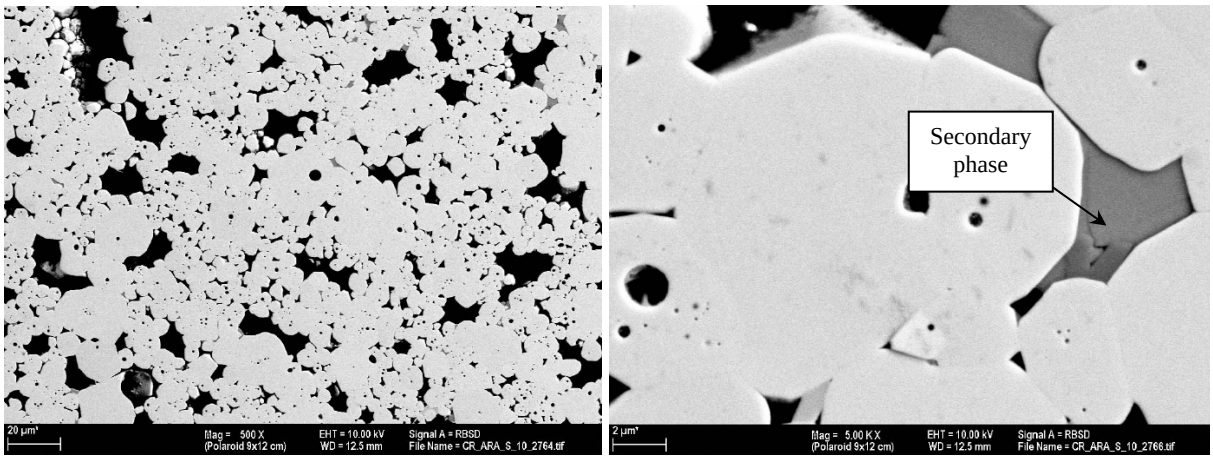

Fig.3.31: Microstructural investigation of $Li_{5.5}Ba_{0.5}La_{2.5}Ta_2O_{12}$ *(thick pellet-middle) by SEM*

Furthermore $Li_{6.875}Ba_{0.125}La_{2.875}Ta_{0.25}Zr_{1.75}O_{12}$ and $Li_{6.25}Ba_{0.25}La_{2.75}TaZrO_{12}$ were investigated. $Li_{6.875}Ba_{0.125}La_{2.875}Ta_{0.25}Zr_{1.75}O_{12}$ (see Fig. 6.46 and 6.47, Chapter 6.2) has a non-homogenous microstructure, a high density and consists, additionally to the main phase, of two secondary phases, where one is contains Zr and O and the other one Ba, La and O.

$Li_{6.25}Ba_{0.25}La_{2.75}TaZrO_{12}$ (Fig. 6.45., Chapter 6.2) is only sintered at the edges of the sample and shows a high porosity and huge holes.

4. Discussion

4.1. Structural features

Before interpreting the obtained electrochemical data it is important to examine in details the various structural parameters.

4.1.1. $Li_7La_3Zr_2O_{12}$ and influence of tantalum on garnet-like materials

XRD investigation of sintered $Li_7La_3Zr_2O_{12}$ shows that the main phase is cubic although pure $Li_7La_3Zr_2O_{12}$ is tetragonal. EDS proved that there is some aluminium in the sample. Even though no aluminium was added during preparation of the samples, it is possible that aluminium comes from the aluminium-containing walls of the oven. Aluminium could be the reason that the sample is mainly cubic, due to the stabilizing effect of substitutional elements.
The exceedingly large pores, visible in picture 3.6, Chapter 3, could arise from a fast kinetic reaction. During sintering, the pores were not able to be filled fast enough and were "overgrown" by the rest of the material.

The graph in Figure 3.8 clearly shows the decrease of the lattice parameter with increasing tantalum content. As Ta^{5+} has a smaller ionic radius than Zr^{4+} the lattice parameter decreases when substituting Ta for Zr.
Considering the SEM pictures it is striking that the angle between two grains is very low (smaller than 60 °), which indicates that the grain boundary energy is much higher than the energy of the surface. As the grains tend to stay in this shape, sintering is thus hampered.
The low density of $Li_{6.5}La_3Ta_{0.5}Zr_{1.5}O_{12}$ could be explained by the preferred form of the grains. It was often mentioned that the grains show an angular shape. During isostatic pressing the grains are compressed and deformed to spheres. Normally a density of around 60 to 65 % is achieved after isostatic pressing. While heating up to sintering temperature the grains tend to return to their preferred shape and recede from each other, which does not lead to an increase in density.

Exaggerated grain growth only appears for $Li_7La_3Zr_2O_{12}$ itself. As soon as zirconium is substituted by tantalum, the huge grains disappear. Further increase in tantalum content leads to a reduction in density. The more elements have to be transported the slower the diffusion, which is responsible for low densities and makes sintering difficult. It can be concluded that exclusive occupation of zirconium or tantalum on B-positions in the garnet contributes to a dense material.

4.1.1.1. Lithium coordination of $Li_{6.5}La_3Ta_{0.5}Zr_{1.5}O_{12}$

The number of lithium cations in octahedral and tetrahedral sites per formula unit for different lithium contents was already shown in Figure 1.15 (see Chapter 1). Figure 4.15 summarizes the relative lithium occupation probabilities for octahedral and tetrahedral sites of various compositions from the literature data.

In Chapter 3.2. it was mentioned that the correct stoichiometric formula for the nominal composition $Li_{6.5}La_3Ta_{0.5}Zr_{1.5}O_{12}$ is $Li_{6.07}La_3Ta_{0.5}Zr_{1.5}O_{12}$.

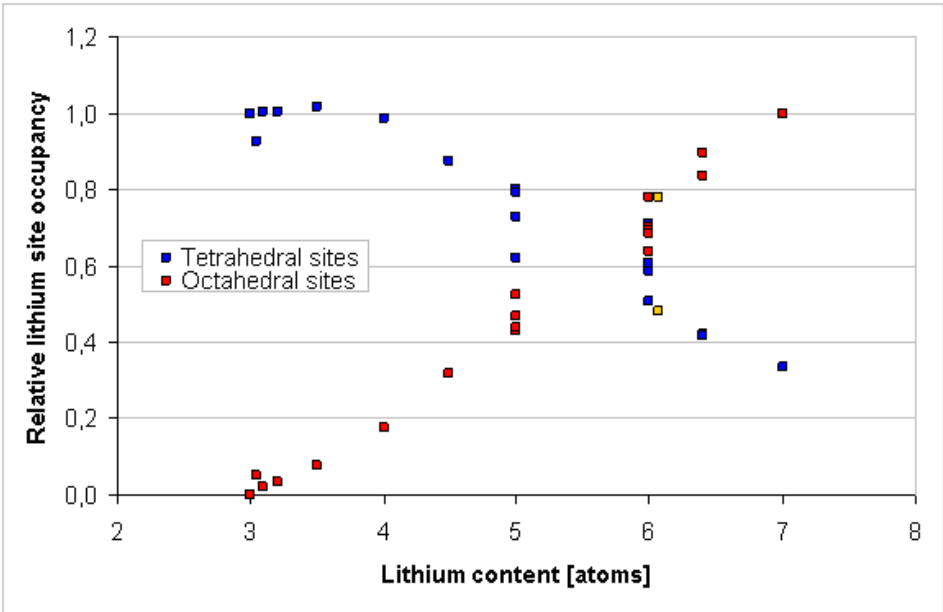

Fig.4.1: Relative lithium occupation probability for octahedral and tetrahedral sites

Comparing the calculated occupancy values of 48.2 % for tetrahedral and 78.2 % for octahedral sites (yellow boxes in Figure 4.1) with the literature data shows a good agreement with the trend.

4.1.2. Influence of strontium on the microstructure of garnet-like materials

The clear dependency of increasing lattice parameter with an increase in substitutional elements can be seen in Figure 3.20 (Chapter 3.4). The colored lines correspond to constant tantalum contents. Strontium has a larger ionic radius than lanthanum and thus increases the lattice parameter. The slopes of the various "iso-tantalum content" lines slightly decrease, which should not be the case as the substitution step of strontium for lanthanum is equal for all tantalum contents.

The lacerated grain boundary shape of $Li_{6.4}Sr_{1.4}La_{1.6}Ta_2O_{12}$ (thick pellet) (Figure 6.44, Chapter 6.2) could be generated by outward moving pores after formation of the grain. Contrary to tantalum substituted compounds, strontium substituted compounds form round and also larger grains.

Based on the densities and the microstructural investigations it is possible to define an area of poor densification, shown in Figure 4.2.

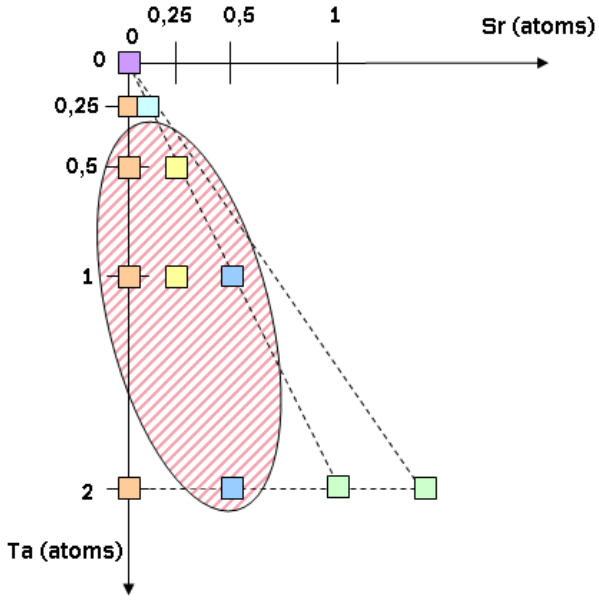

Fig.4.2: Area of poor densification of strontium / tantalum substituted samples

4.1.3. Influence of barium on the microstructure of garnet-like materials

The increase of the lattice parameter of barium substituted compounds is even higher than that of strontium for the same compositions. Because the ionic radius of barium is larger than the one of strontium, the lattice parameter increases strongly (see Figure 3.26, Chapter 3.5). Due to kinks appearing in the yellow and the green curve and the appearance of secondary phases even before sintering, it can be assumed that these compositions are not any more in the

solubility domain of barium in the garnet structure. Figure 4.3 shows the probable solubility limit for barium / tantalum substitution.

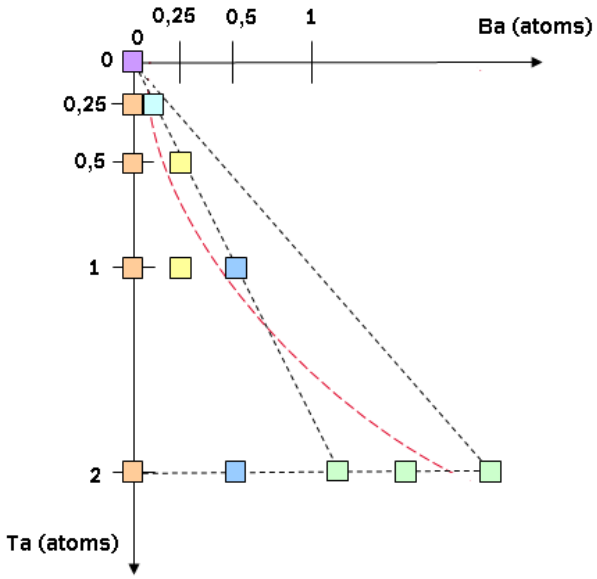

Fig.4.3: Solubility limit (red dashed line) for barium / tantalum substitution

It is conspicuous that inhomogeneities (see Figure 6.49 (right), Chapter 6.2) are always along a straight line, which could be a crystallographic plane where segregation preferentially takes place. One of the secondary phases seems to have formed a liquid phase during sintering. This idea is supported by the phase diagram of $BaCO_3$ and Li_2CO_3, shown in Figure 4.4. Barium carbonate and lithium carbonate form a liquid phase at temperatures > 609 °C which are reached during the sintering process.

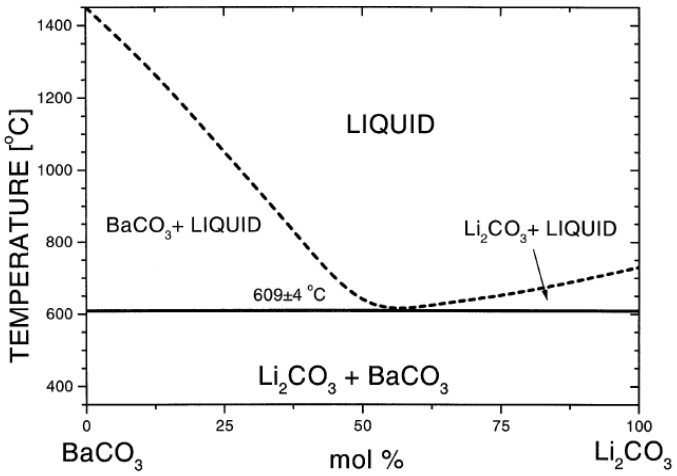

Fig.4.4: Phase diagram of $BaCO_3$ and Li_2CO_3 (according to Ref 49)

When liquid phases are created in all parts of the sample, very high densities up to 90 % can be reached. Hence sintering is favored by liquid phases.

From microstructural investigation it can be observed that barium containing compounds exhibit, like strontium compounds, round grains. Additionally barium containing compounds form larger grains than the pure tantalum compounds.

4.1.4. Comparison between substitution of lanthanum by calcium, strontium and barium

Comparison of $Li_{6.5}Ca_{0.5}La_{2.5}TaZrO_{12}$, $Li_{6.5}Sr_{0.5}La_{2.5}TaZrO_{12}$ and $Li_{6.5}Ba_{0.5}La_{2.5}TaZrO_{12}$ indicates a clear dependence of the lattice parameter (see Figure 4.5).

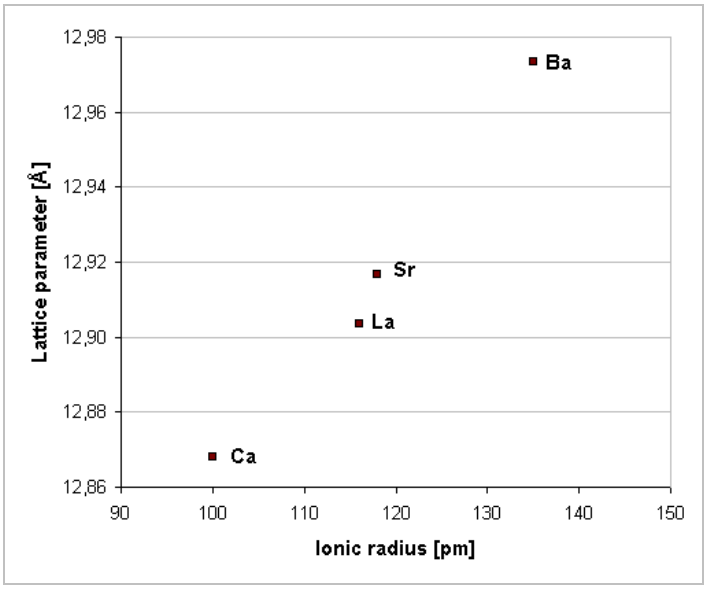

Fig.4.5: Influence of the ionic radius on the lattice parameter of $Li_{6.5}A_{0.5}La_{2.5}TaZrO_{12}$ $(A = Ca, Sr, Ba)$

Calcium, which possesses a slightly smaller ionic radius than lanthanum, possesses the smallest lattice parameter of all three samples with the same nominal composition, while barium marks the top of the line in Figure 4.4.

A few samples, which do not show any trend concerning composition or substitutional elements, exhibit a very characteristic yellow color. A possible explanation could be the presence of oxygen vacancies in the lattice, which might result in so-called color centers. The missing charges are neutralized by electrons, which are able to absorb electromagnetic radiation.

As a conclusion it can be said, that exclusive occupation of zirconium or tantalum on B-positions, together with occupation of strontium or barium on A-positions in the garnet, is likely to create dense samples due to their tendency to form round grains, liquid phases and the advantage of a fast diffusion to different lattice sites. Effectively, data from Tables 3.3, 3.5 and 3.7 report that $Li_5La_3Ta_2O_{12}$, $Li_{6.4}Sr_{1.4}La_{1.6}Ta_2O_{12}$ and $Li_6BaLa_2Ta_2O_{12}$ show the highest densities for tantalum substituted, strontium substituted and barium substituted samples, respectively.

4.2. Electrochemical features

4.2.1. Electrochemical properties of $Li_7La_3Zr_2O_{12}$

In general tetragonal garnets are moderate ion conductors as can be found in the literature. $Li_7La_3Zr_2O_{12}$ samples show a conductivity value at the same order of magnitude as reported in the literature. As the conductivity is dependent on the density of the pellet, the thick pellet shows a much higher conductivity than the thin pellet. Additionally there is a difference in the phase composition, which may have an influence on the conductivity as well.
Table 4.1. contains the values for conductivity and activation energy and the values found in the literature for $Li_7La_3Zr_2O_{12}$. The conductivity value of the cubic material of the literature shows a higher conductivity, while the tetragonal garnet is about the same order of magnitude.

BOSCH			Literature			
Compound	**σ_{total} [S/cm] (°C)^2**	**E_A [eV]**	**Compound**	**σ_{total} [S/cm] (°C)^2**	**E_A [eV]**	**Ref.**
$Li_7La_3Zr_2O_{12}$ (thick) $Li_7La_3Zr_2O_{12}$ (thin)	$1.87 \cdot 10^{-6}$ (23) $1.38 \cdot 10^{-8}$ (23)	0.73 0.69	$Li_7La_3Zr_2O_{12}$ cubic	$3.0 \cdot 10^{-4}$ (25)	0.32	21
			$Li_7La_3Zr_2O_{12}$ tetragonal	$2.19 \cdot 10^{-6}$ (23)	0.54	24

Tab.4.1.: Comparison of conductivity and activation energy of $Li_7La_3Zr_2O_{12}$ with the literature

It is striking is that all activation energy data, independent of composition, show a large difference compared to literature data.
It has to be mentioned that, although the conductivity is dependent on the density, none of the reported literature data contained any information about the density. On closer examination of

the literature it is apparent that all calcination and sintering steps were carried out in an Al_2O_3 boat or crucible respectively. At elevated temperatures alumina forms a liquid phase together with lithium oxide. This was proved by a video controlled sintering process, where droplets accumulated at the transparent sapphire panel, which means that aluminium is likely to enter the structure leading to an unintended and unnoticed substitution in the crystal lattice

Differences in activation energy may have different reasons which are valid for all prepared compositions. As the thin and thick pellet of one and the same material are sintered together in the MgO box, the thicker one might experience a higher pressure on its upper side, due to the weight of the powder bed and the MgO cover plate, than the thin pellet. During sintering, Li_2CO_3 decomposes into Li_2O and CO_2, which means that the sintering process is done in a CO_2 atmosphere. If the top is covered by the powder bed and the cover plate, a gas phase reaction with the surface of the material can occur only at the rims of the sample. On the contrary, the thin pellet, which is just slightly covered by the powder bed, has a much higher surface to react with CO_2. A secondary phase and a density gradient can be formed. Due to such inhomogeneities, differences in the activation energy may occur. The other possibility is that secondary phases influence the activation energy. In general secondary phases do not have any influence on the activation energy if they form individual grains, but as soon as the secondary phase affects the lithium ion conduction pathway it can lead to a change in activation energy. As it was not possible to carry out microstructural investigations for all produced samples, it is hard to say which explanation fits best.
The column “Number of semi-circles” in Chapter 3 gives the devolution of the conductivity curve. The impedance plot can be assembled by different contributions, which could be resistance of the bulk material, the grain boundaries and diffusion. If two semi-circles are observed, they may be due to contributions from bulk material and grain boundaries. Until now it is not fully resolved which semi-circles belongs to which contribution.

4.2.2. Influence of tantalum on electrochemical properties

Figure 4.6 illustrates a plot of the conductivity and the activation energy against tantalum content. Generally high conductivity values correlate with low activation energy values. The best conductivity value is reported for $Li_5La_3Ta_{0.25}Zr_{1.75}O_{12}$. Comparing the values for thick and thin pellets shows comparable values.

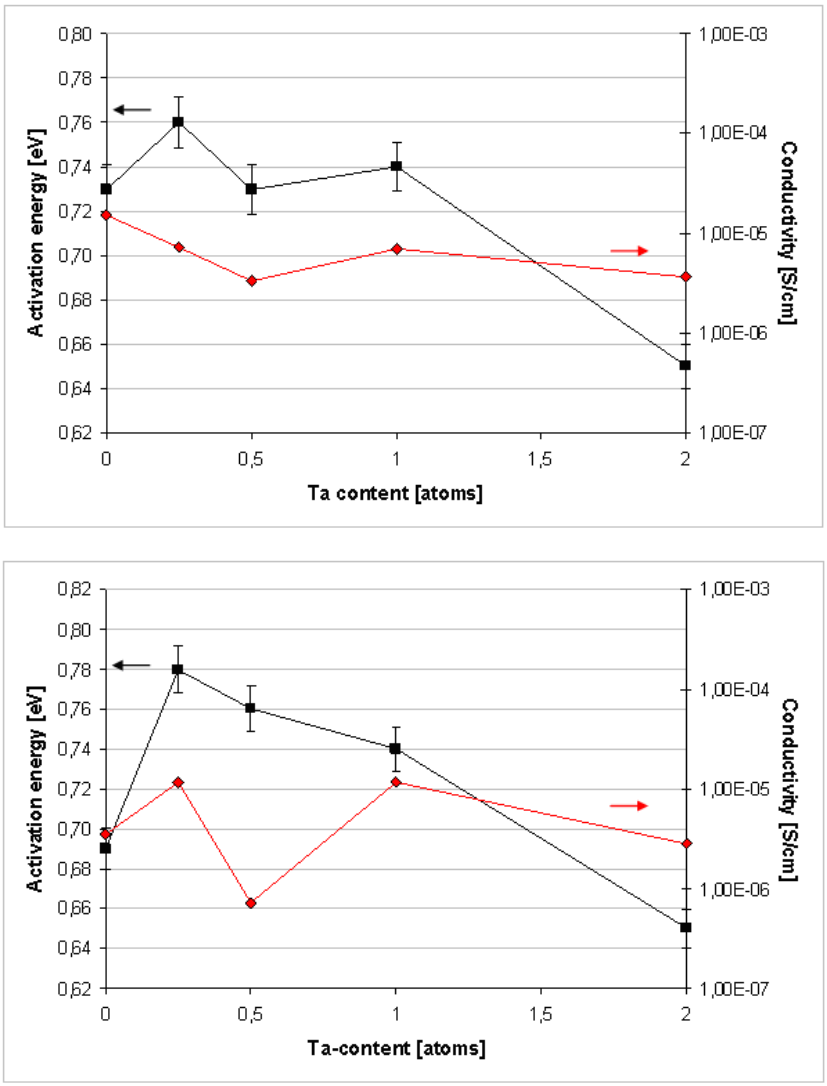

Fig.4.6: Dependence of conductivity and activation energy on tantalum content.
Upper picture: values thick pellets, lower picture: values thin pellets

Table 4.2. contains the values for conductivity and activation energy determined here and the values found in the literature for $Li_5La_3Ta_2O_{12}$. The conductivity value for $Li_5La_3Ta_2O_{12}$ is nearly identical to the literature value but shows a much higher activation energy.

BOSCH			Literature			
Compound	**σ_{total} [S/cm] (°C)^2**	**E_A [eV]**	**Compound**	**σ_{total} [S/cm] (°C)^2**	**E_A [eV]**	**Ref.**
$Li_5La_3Ta_2O_{12}$ (thick) $Li_5La_3Ta_2O_{12}$ (thin)	$3.69 \cdot 10^{-6}$ (23) $2.78 \cdot 10^{-6}$ (23)	0.65 0.65	$Li_5La_3Ta_2O_{12}$	10^{-6} (22)	0.43	39

Tab.4.2.: Comparison of conductivity and activation energy of $Li_5La_3Ta_2O_{12}$ with the literature

4.2.3. Influence of strontium on electrochemical properties

Figure 4.7 shows the dependence of conductivity on the strontium content at different constant tantalum contents.

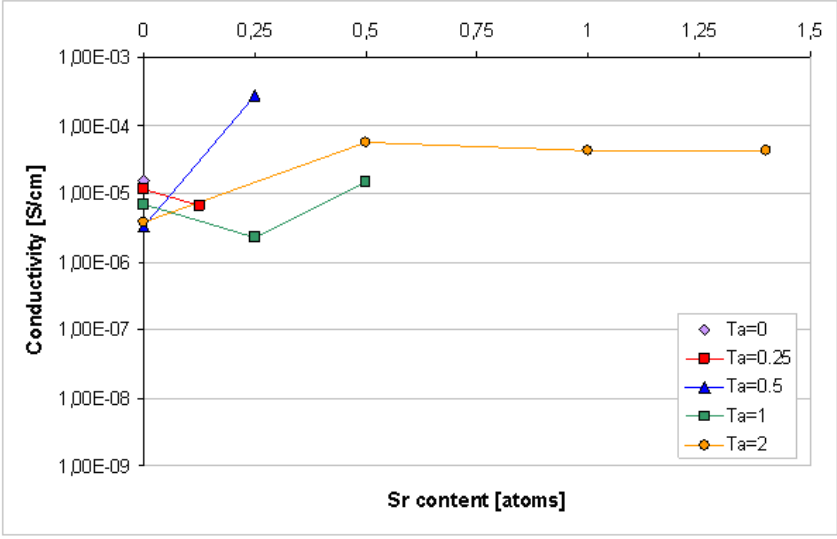

Fig.4.7: Dependence of conductivity on the strontium content at different constant tantalum contents for thick pellets

The curves of conductivity and activation energy for compositions without zirconium (Ta=2) are shown in Figure 4.8. The minimum of the curve is observed for $Li_{5.5}Sr_{0.5}La_{2.5}Ta_2O_{12}$.

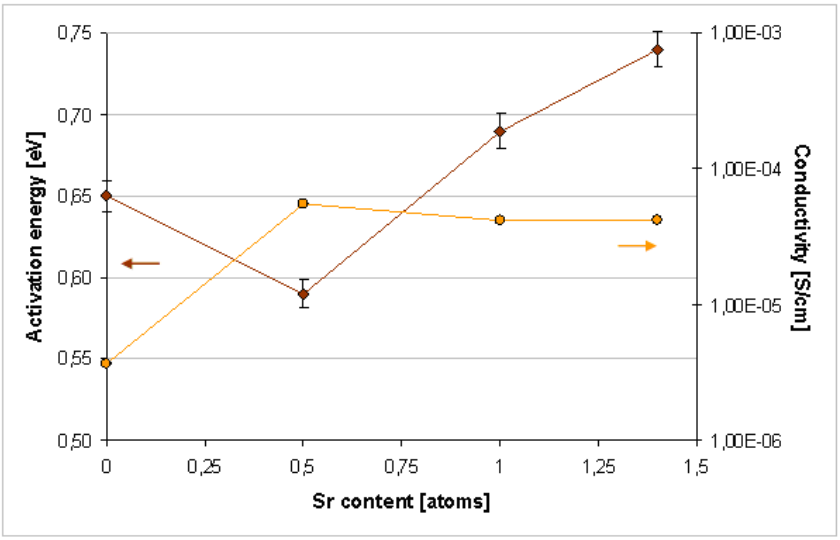

Fig.4.8: Dependence of conductivity and activation energy on strontium content at constant tantalum content (Ta=2) for thick pellets

Together with the fact that the density is best when only a few different elements have to be transported at the same time, compositions similar to $Li_{5.5}Sr_{0.5}La_{2.5}Ta_2O_{12}$ could be promising candidates.

The comparison of conductivity values before and after measurement of the activation energy shows that the conductivity after activation energy measurement decreases (dashed line in Figure 4.9).

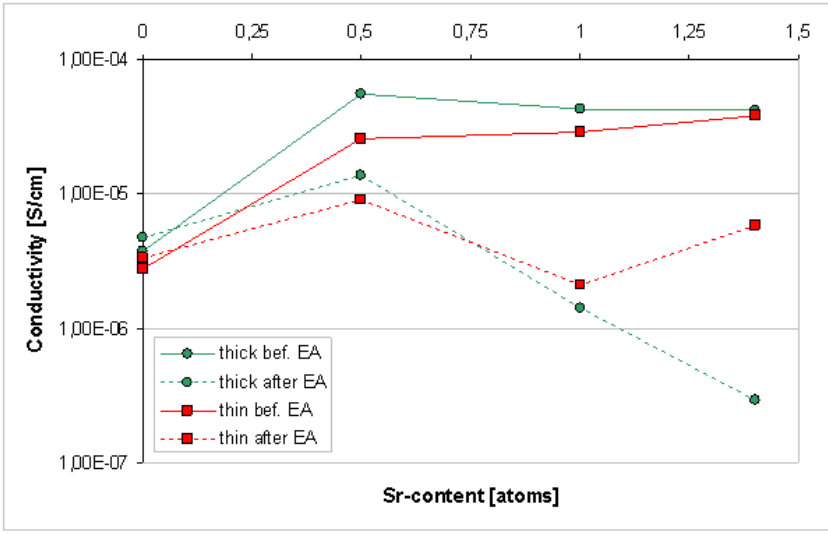

Fig.4.9: Comparison of conductivity values before and after measurement of activation energy for thick and thin pellets of the same composition

An outstanding composition ($Li_{6.75}Sr_{0.25}La_{2.75}Ta_{0.5}Zr_{1.5}O_{12}$) could be found having a total conductivity of $3.20 \cdot 10^{-4}$ S·cm^{-1}, which is higher than the best reported garnet-like compounds in the literature. It is also interesting that the conductivity does not change after activation energy measurement for this sample. This is probably referable to the very high shrinkage of 42 % and the high resulting density of 88 %.

The following Table 4.3. contains the values for conductivity and activation energy and the values found in the literature for $Li_6SrLa_2Ta_2O_{12}$, for which a much better conductivity value could be achieved.

BOSCH			Literature			
Compound	**σ_{total} [S/cm] (°C)^2**	**E_A [eV]**	**Compound**	**σ_{total} [S/cm] (°C)^2**	**E_A [eV]**	**Ref.**
$Li_6SrLa_2Ta_2O_{12}$ (thick) $Li_6SrLa_2Ta_2O_{12}$ (thin)	$4.20 \cdot 10^{-5}$ (23) $2.88 \cdot 10^{-5}$ (23)	0.69 0.70	$Li_6SrLa_2Ta_2O_{12}$	$7.00 \cdot 10^{-6}$ (22)	0.50	29
			$Li_6SrLa_2Ta_2O_{12}$	$9.33 \cdot 10^{-6}$ (33)	0.45	16
			$Li_6SrLa_2Ta_2O_{12}$	$1.18 \cdot 10^{-5}$ (33)	0.45	16
			$Li_6SrLa_2Ta_2O_{12}$	$7.00 \cdot 10^{-6}$ (22)	0.50	25

Tab.4.3.: Comparison of conductivity and activation energy of $Li_6SrLa_2Ta_2O_{12}$ with the literature

When measuring the activation energy another large semi-circle appears at low frequency ranges (see Fig.3.22, Chapter 3.4.) showing a high resistance at the order of 10^7 Ω. This effect is not specific for certain compositions or substitutional elements and appears for tantalum, calcium, strontium and barium substituted samples. As this effect is observable for nearly every composition, it is possible that this stems from the gold electrode.

4.2.4. Influence of barium on electrochemical properties

For the first general overview, Figure 4.10 illustrates the dependence of the conductivity on the barium content at constant tantalum contents.

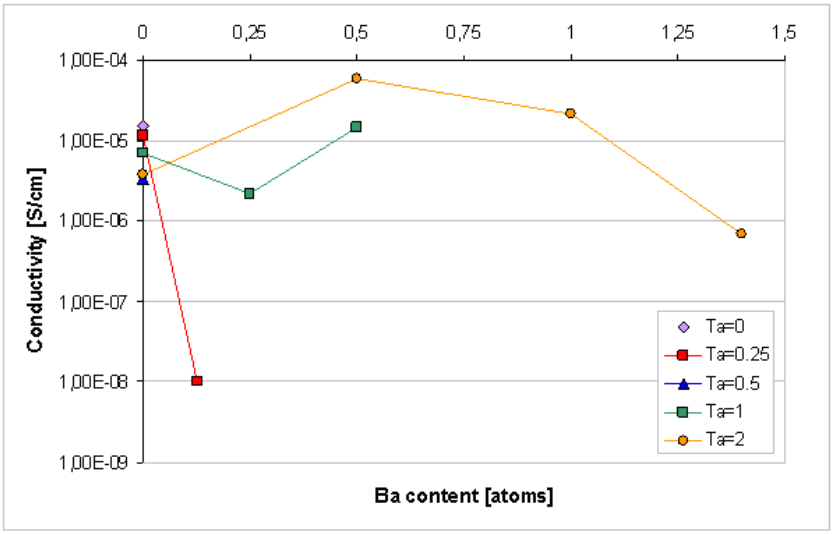

Fig.4.10: Dependence of conductivity on barium content at constant tantalum contents for thick pellets

As in the case of tantalum/strontium substituted samples it is striking that the best conductivity value is reported for a composition $Li_{5.5}Ba_{0.5}La_{2.5}Ta_2O_{12}$.

Figure 4.11 exclusively shows the development of conductivity and activation energy for barium at Ta=2. It can be seen, that high conductivity values correlate with low activation energy values.

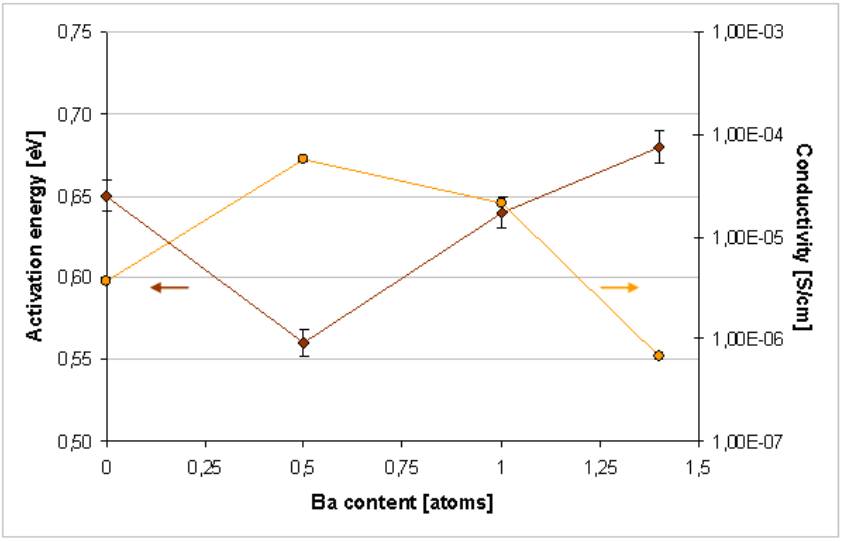

Fig.4.11: Dependence of conductivity and activation energy on barium content at constant tantalum content (Ta=2) for thick pellets

Excluding the red dashed line in Figure 4.12, which shows the comparison of conductivity values before and after measurement of activation energy, all other curves show a similar trend.

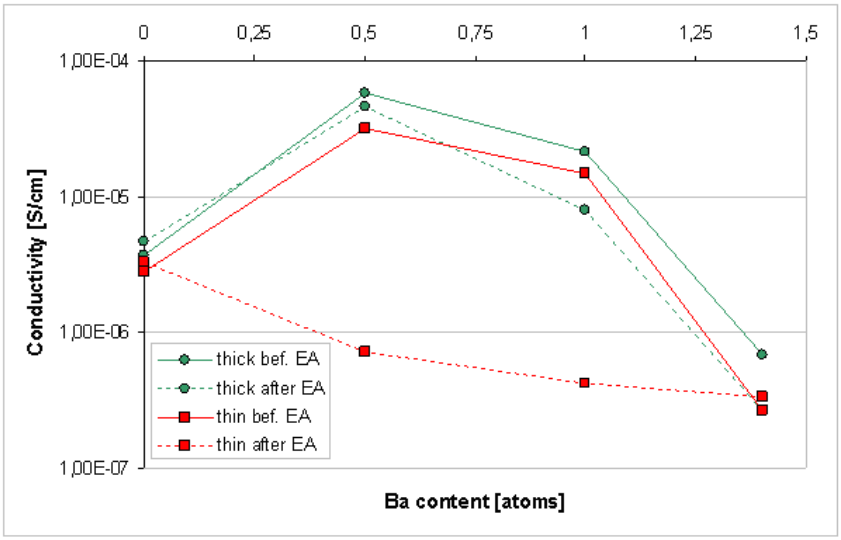

Fig.4.12: Comparison of conductivity values before and after measurement of activation energy for thick and thin pellets of the same composition

It can be clearly seen that the conductivity slightly decreases for the thick pellet after measurement of activation energy and drastically decreases for the thin pellet.

Lattice parameters of sintered barium and tantalum substituted samples hardly show any difference. Taking into account the high amount of secondary phases leads to the assumption that CO_2 partially takes barium out of the structure during the sintering process. Pure barium carbonate is indeed a very stable compound up to 1300 °C

The values for conductivity and activation energy and the values found in the literature for the same compositions are contained in Table 4.4. The conductivity value for $Li_6BaLa_2Ta_2O_{12}$ is nearly identical to literature value, while $Li_{6.5}Ba_{0.5}La_{2.5}TaZrO_{12}$ showed a lower conductivity in the present study. It is noteworthy that the activation energy data show a large difference compared to the literature data.

BOSCH			Literature			
Compound	**σ_{total} [S/cm] (°C)^2**	**E_A [eV]**	**Compound**	**σ_{total} [S/cm] (°C)^2**	**E_A [eV]**	**Ref.**
$Li_6BaLa_2Ta_2O_{12}$ (thick) $Li_6BaLa_2Ta_2O_{12}$ (thin)	$2.11 \cdot 10^{-5}$ (23) $1.47 \cdot 10^{-5}$ (23)	0.64 0.63	$Li_6BaLa_2Ta_2O_{12}$	$4.00 \cdot 10^{-5}$ (22)	0.40	29
			$Li_6BaLa_2Ta_2O_{12}$	$1.78 \cdot 10^{-5}$ (17)	0.42	16
			$Li_6BaLa_2Ta_2O_{12}$	$1.22 \cdot 10^{-5}$ (17)	0.42	16
			$Li_6BaLa_2Ta_2O_{12}$	$1.51 \cdot 10^{-4}$ (50)	0.42	13
			$Li_6BaLa_2Ta_2O_{12}$	$5 \cdot 10^{-5}$ (33)	0.42	32
$Li_{5,5}Ba_{0,5}La_{2,5}Ta_2O_{12}$ (thick) $Li_{5,5}Ba_{0,5}La_{2,5}Ta_2O_{12}$ (thin)	$5.72 \cdot 10^{-5}$ (23) $3.16 \cdot 10^{-5}$ (23)	0.56 0.73	$Li_{5,5}Ba_{0,5}La_{2,5}Ta_2O_{12}$	$1.9 \cdot 10^{-5}$ (33)	0.46	32
$Li_{6,5}Ba_{0,5}La_{2,5}TaZrO_{12}$ (thick) $Li_{6,5}Ba_{0,5}La_{2,5}TaZrO_{12}$ (thin)	$4.95 \cdot 10^{-6}$ (23) $3.60 \cdot 10^{-7}$ (23)	0.74 0.85	$Li_{6,5}Ba_{0,5}La_{2,5}TaZrO_{12}$	$2.00 \cdot 10^{-4}$ (23)	0.31	14

Tab.4.4.: Comparison of conductivity and activation energy of $Li_{6.5}Ba_{0.5}La_{2.5}TaZrO_{12}$ and $Li_6BaLa_2Ta_2O_{12}$ with the literature

Figure 4.13 summarizes the conductivities for the various substitutional elements independent of their composition. Besides the very high conductivity value for the strontium composition there is a general trend that the conductivities increase from tantalum substituted to barium substituted samples. Because barium has a larger ionic radius, the lattice parameter increases also.

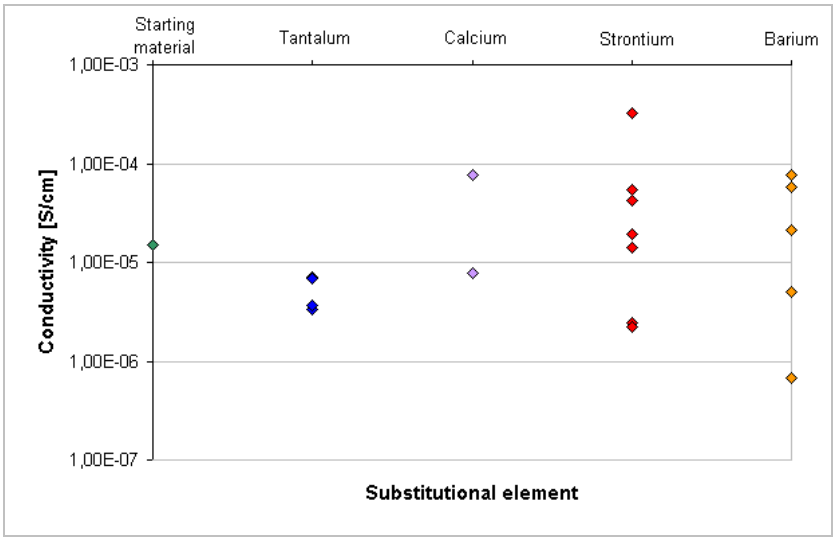

Fig.4.13: Conductivities for various substitutional elements (for thick pellets)

A similar plot can be done as well for the conductivity and the activation energy for different compounds as a function of the lithium content see Figures 4.14 and 4.15 below.

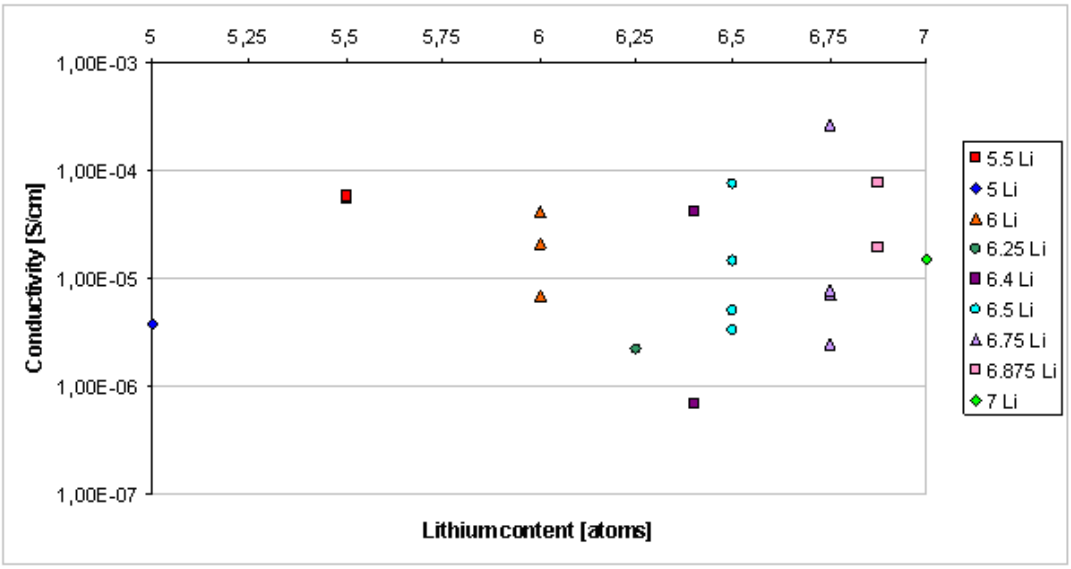

Fig.4.14: Conductivities in dependence of lithium content (for thick pellets)

In Figure 4.14. it can be clearly seen, that the activation energy is increasing with increasing lithium content after the minimum values at 5.5 lithium ions per formula unit.

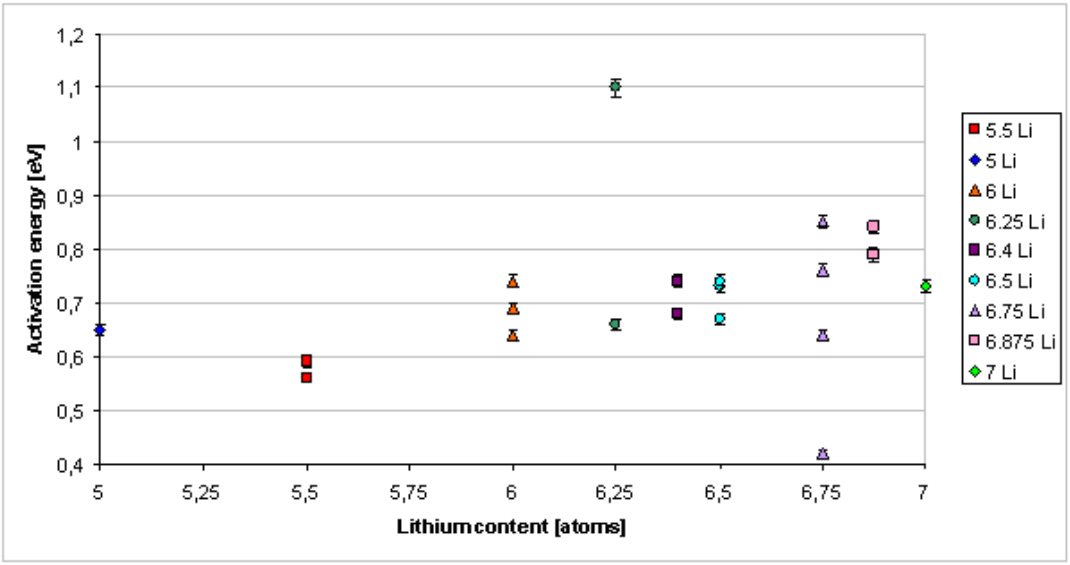

Fig.4.15: Activation energies in dependence of lithium content (for thick pellets)

4.3. Influence of the measuring method on the conductivity

As already listed in Chapter 3 and mentioned in Chapter 4.2.1 – 4.2.4, all samples, regardless of composition and substitutional elements, show a decrease in conductivity before and after measurement of the activation energy. The following Figure 4.16 shows the corresponding change in conductivity for the various substitutional classes. In some cases drastic changes in conductivity can be observed, especially for calcium and strontium substituted samples.

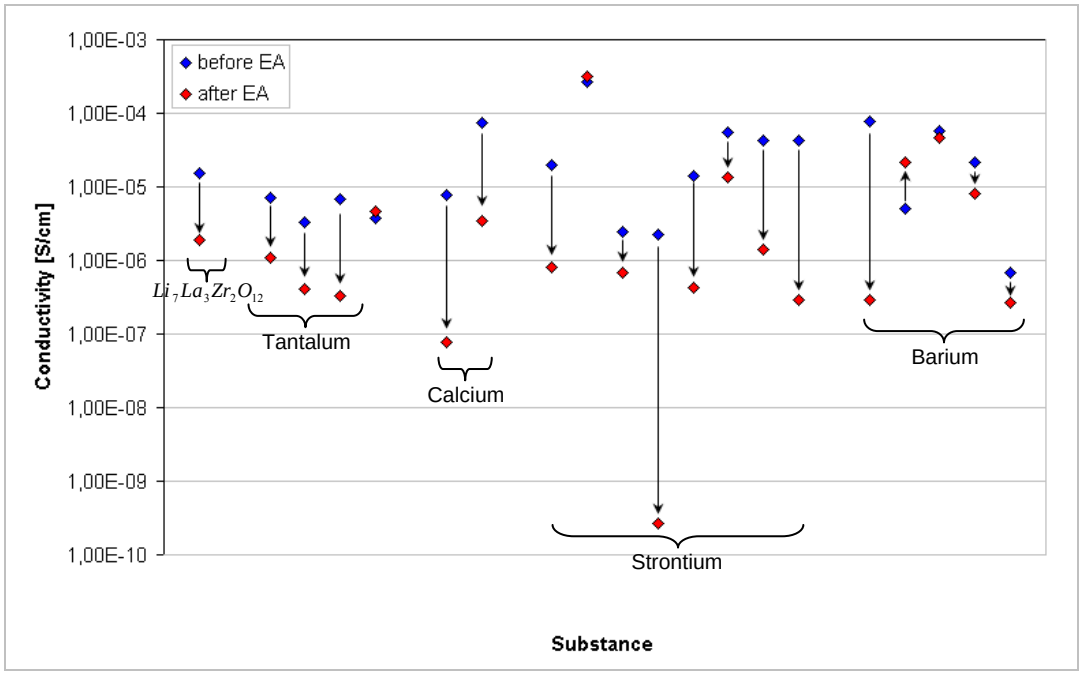

Fig.4.16: Change in conductivity after measurement of activation energy (for thick pellets)

As this effect is not observed when measuring the conductivity repeatedly at room temperature and also after heat treatment in the oven at 260 °C, the change in conductivity could be due to simultaneous influence of the electrical field and heat. If the density is around 93 %, the percolation limit is reached, which means that the pores are enclosed and do not form channels any more. As most of the samples have a much lower density than 93 %, air can circulate through the pores of the sample and CO_2 may react with the lithium content of the garnet to form Li_2CO_3. This Li_2CO_3, which is non-conducting, would accumulate at the surface of the grains, forming blocking grain boundaries and thus leading to a decrease in conductivity (see Figure 4.17).

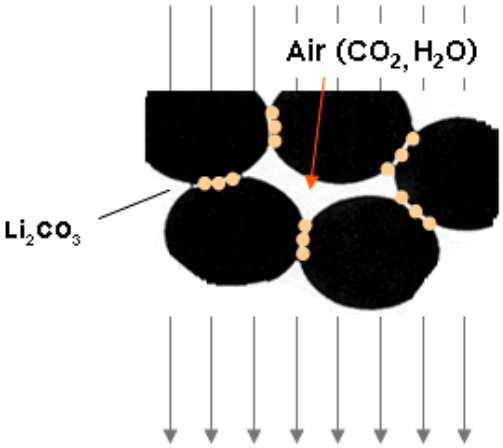

Fig.4.17: Blocking grain boundaries formed under influence of an electrical field and heat

It still has to be investigated if the formation of Li_2CO_3 and of blocking grain boundaries is reversible when heating up the sample to 700 °C (decomposition temperature of Li_2CO_3).

4.4. Future prospects

At the end of this work a few materials having aluminium as substitutional element have been produced showing high conductivity and low activation energies. Considering the phase diagram of Li_2CO_3 and Al_2O_3 it can be seen that liquid phases are occurring at the applied sintering temperatures, which favors the formation of dense samples and a characteristic yellow color. In Figure 4.18 the phase diagram of Li_2O and Al_2O_3 is shown. The melting temperatures in the actual phase diagram of Li_2CO_3 and Al_2O_3 are shifted to lower temperatures.

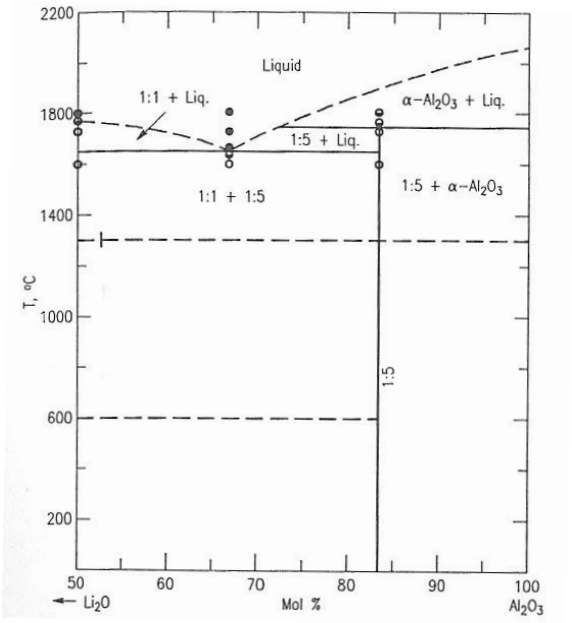

Fig.4.18: Phase diagram of Li_2O and Al_2O_3 (according to Ref. 50)

Molecular simulations proved that Al^{3+} occupies tetrahedral lattice sites and hence displaces enough charge carriers and vacancies to the octahedral positions, which might lead to an increase in conductivity.

5. Conclusion

5.1. Summary

Garnet-like materials are promising candidates as fast lithium ion conducting solid electrolyte. As only very few literature data are available, the field of tantalum and earth alkali substituted $Li_7La_3Zr_2O_{12}$ garnet-like material was investigated extensively in this work. In total twenty-two compositions have been prepared by all-solid-state reaction. All tantalum, calcium and strontium substituted garnet compounds show high phase purity before and after sintering. For barium substituted samples a possible solubility domain was defined.

It could be observed that the microstructure is strongly dependent on the composition and that most of the samples are not dense. Microstructural investigations proved that most of the samples, independent of the composition, have huge pores and inhomogeneities over their entire thickness.

Nearly all samples exhibit strong fluctuations in ionic conductivity before and after the measurement of electrochemical properties, which is probably caused by the application of an electrical field and heat at the same time. This effect is ascribed to the formation of blocking grain boundaries with very low ionic conductivity. As the various samples show different densities and as the ionic conductivity depends on the density, conductivity values cannot be directly compared.

However, beside $Li_{6.75}Sr_{0.25}La_{2.75}Ta_{0.5}Zr_{1.5}O_{12}$, all samples show a conductivity between 10^{-5} and 10^{-7} S·cm^{-1}, which is far to low too be employed as solid state electrolyte in electrical devices.

The validity of all reported literature data, where Al_2O_3 crucibles were used for sample preparation is questionable, as unintended substitution by aluminium might influence the data. Contrarily to most published values, all compounds in the present study were prepared without utilization of Al_2O_3. It was possible to increase the conductivity to $3.2 \cdot 10^{-4}$ S·cm^{-1}, which is higher than all reported conductivities of garnet-like materials before. Hence it is necessary to further investigate $Li_{6.75}Sr_{0.25}La_{2.75}Ta_{0.5}Zr_{1.5}O_{12}$ to understand the mechanism of ionic conduction in this material and to prove its applicability as solid state ceramic electrolyte.

5.2. Zusammenfassung

Granatähnliche Materialien sind eine entwicklungsfähige Substanzklasse für zukünftige Festkörperelektrolyte, die eine schnelle Lithiumionenleitung aufweisen. Da es nur wenig Literatur auf dem Gebiet der tantal- und erdalkalisubstituierten $Li_7La_3Zr_2O_{12}$ Materialien gibt, wurde gerade dieses Feld intensiv untersucht. Insgesamt wurden zweiundzwanzig Zusammensetzungen durch eine reine Festkörper-Reaktion hergestellt und mittels verschiedenster Methoden charakterisiert. Alle tantal-, calcium- und strontiumsubstituierten Granatverbindungen weisen eine sehr hohe Phasenreinheit, sowohl vor als auch nach dem Sinterprozess, auf. Für bariumsubstituierte Substanzen konnte eine mögliche Löslichkeitsgrenze gefunden werden.

Es zeigte sich deutlich, dass das Gefüge stark von der Zusammensetzung abhängig ist und die meisten Proben nicht dicht sind. Gefügeuntersuchungen belegten, dass ein Großteil der Proben, unabhängig von der Zusammensetzung, riesige Poren und Inhomogenitäten über ihren gesamten Dickenbereich aufweisen.

Nahezu alle Proben unterliegen einer starken Schwankung in der ionischen Leitfähigkeit, verglichen vor und nach der Messung der elektrischen Eigenschaften, die eine Applikation eines elektrischen Feldes und Hitze impliziert. Der auftretende Effekt der Änderung der Leitfähigkeit kann auf die Ausbildung von blockierenden Korngrenzen mit niedriger Lithiumionenleitfähigkeit zurückgeführt werden. Proben unterschiedlicher Dichte können auf Grund der Dichteabhängigkeit der Leitfähigkeit nicht verglichen werden.

Alle hergestellten Proben, mit Ausnahme von $Li_{6,75}Sr_{0,25}La_{2,75}Ta_{0,5}Zr_{1,5}O_{12}$, zeigen eine Leitfähigkeit zwischen 10^{-5} und 10^{-7} S·cm^{-1}, was zu niedrig ist um diese Materialien als Festkörperelektrolyte in Elektrogeräten zu verwenden.

Die Aussagekraft von publizierten Daten, in denen bei der Herstellung Al_2O_3-Tiegel verwendet wurden, ist stark gemindert, da durch eine unbewusste Substitution eine Verfälschung der Daten auftreten könnte.

Im Gegensatz zu den meisten veröffentlichten Werten, wurden alle Materialien in der vorliegenden Arbeit ohne Verwendung von Al_2O_3 oder Al_2O_3-haltigen Tiegeln hergestellt. Es war möglich die Leitfähigkeit auf $3{,}2 \cdot 10^{-4}$ S·cm^{-1} zu steigern, was höher als alle bisher publizierten Leitfähigkeiten granatähnlicher Materialien ist. Daher ist es unerlässlich $Li_{6,75}Sr_{0,25}La_{2,75}Ta_{0,5}Zr_{1,5}O_{12}$ weiteren Untersuchungen zu unterwerfen, um den Mechanismus der Lithiumionenleitung zu verstehen und die Einsetzbarkeit als Festkörperelektrolyten zu validieren.

6. Appendix

6.1. Appendix 1 – Electrical characterization of garnet-like materials

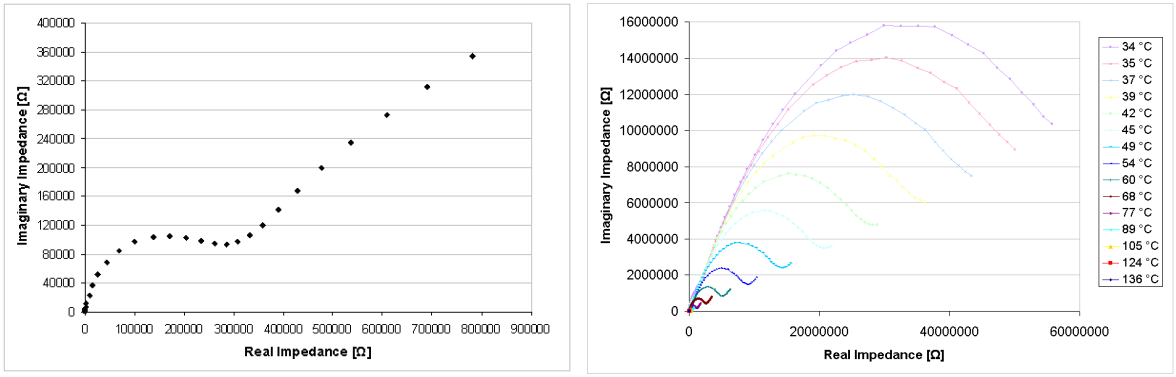

Fig. 6.1: Impedance plot for conductivity measurement at room temperature before activation energy measurement (left) and activation energy measurement between 34 °C and 136 °C (right) of $Li_7La_3Zr_2O_{12}$ *(thin pellet)*

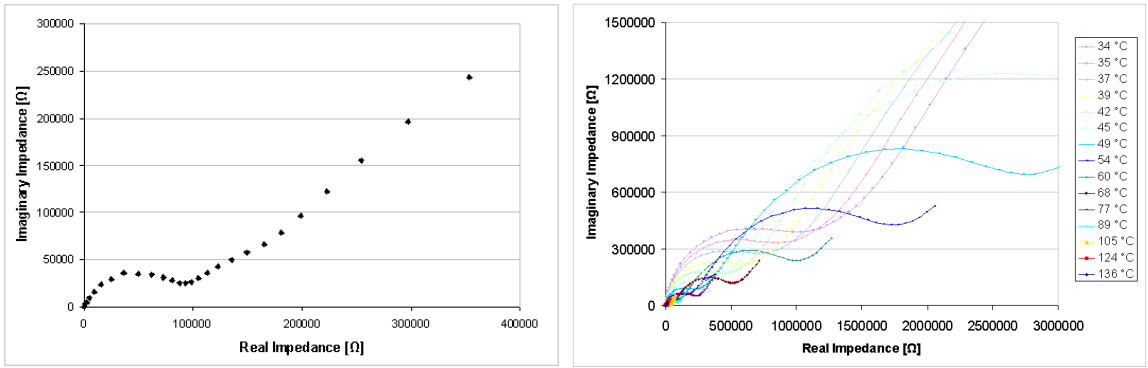

Fig. 6.2: Impedance plot for conductivity measurement at room temperature before activation energy measurement (left) and activation energy measurement between 34 °C and 136 °C (right) of $Li_{6.75}La_3Ta_{0.25}Zr_{1.75}O_{12}$ *(thin pellet)*

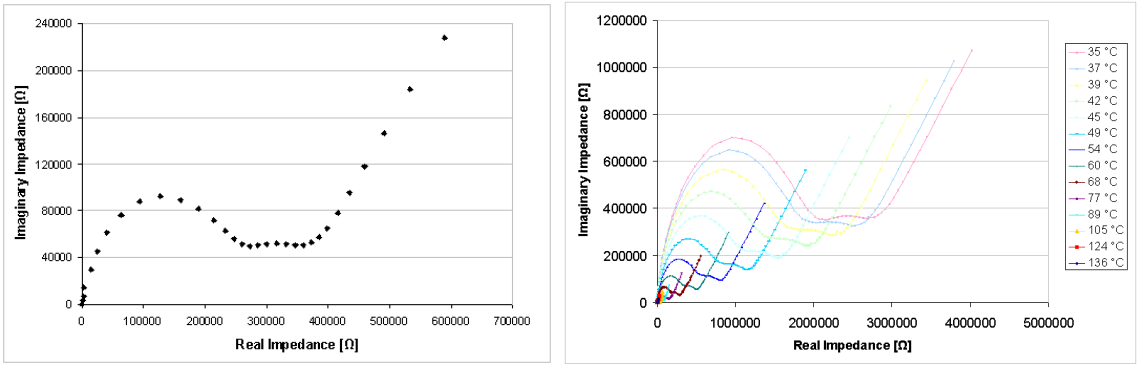

Fig. 6.3: Impedance plot for conductivity measurement at room temperature before activation energy measurement (left) and activation energy measurement between 35 °C and 136 °C (right) of $Li_{6.5}La_3Ta_{0.5}Zr_{1.5}O_{12}$ *(thick pellet)*

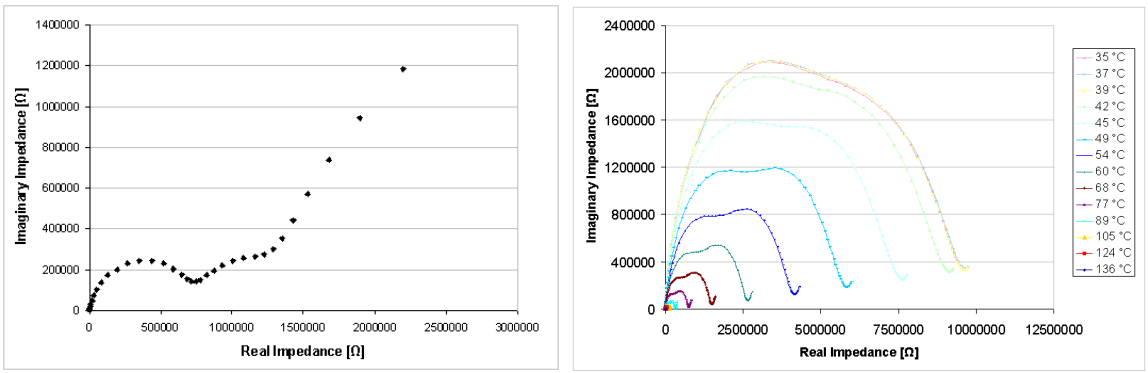

Fig. 6.4: Impedance plot for conductivity measurement at room temperature before activation energy measurement (left) and activation energy measurement between 35 °C and 136 °C (right) of $Li_{6.5}La_3Ta_{0.5}Zr_{1.5}O_{12}$ *(thin pellet)*

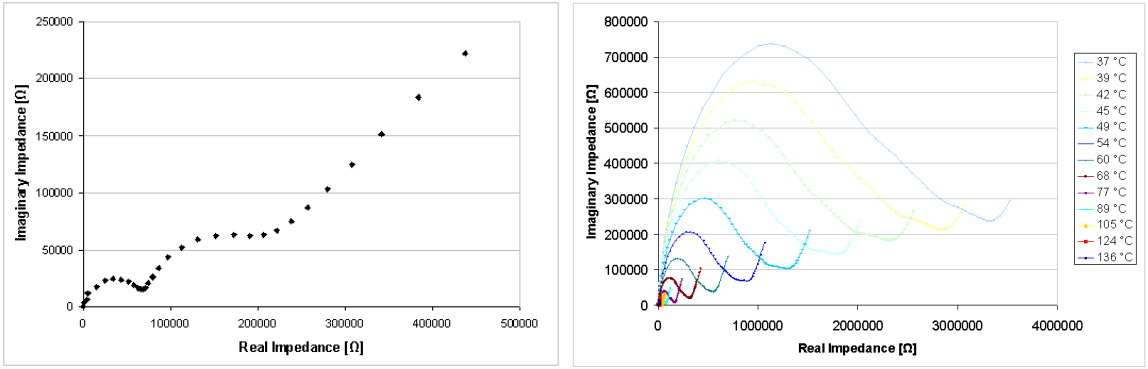

Fig. 6.5: Impedance plot for conductivity measurement at room temperature before activation energy measurement (left) and activation energy measurement between 37 °C and 136 °C (right) of $Li_6La_3TaZrO_{12}$ *(thick pellet)*

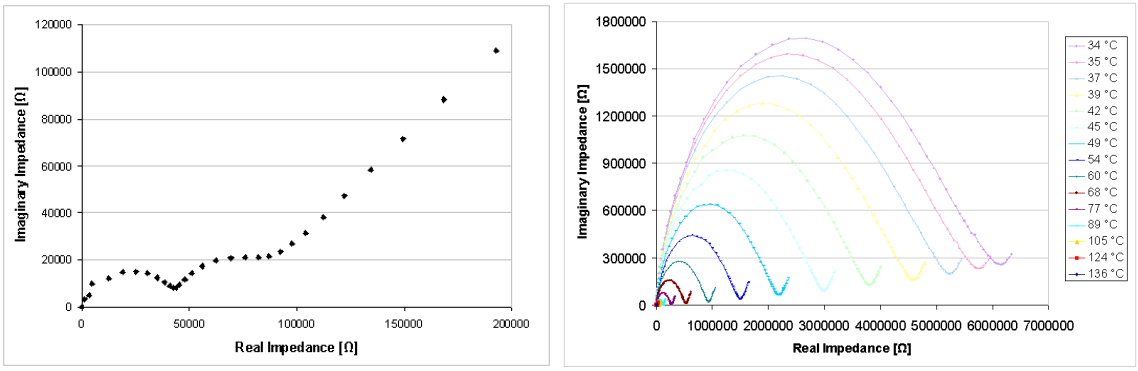

Fig. 6.6: Impedance plot for conductivity measurement at room temperature before activation energy measurement (left) and activation energy measurement between 34 °C and 136 °C (right) of $Li_6La_3TaZrO_{12}$ *(thin pellet)*

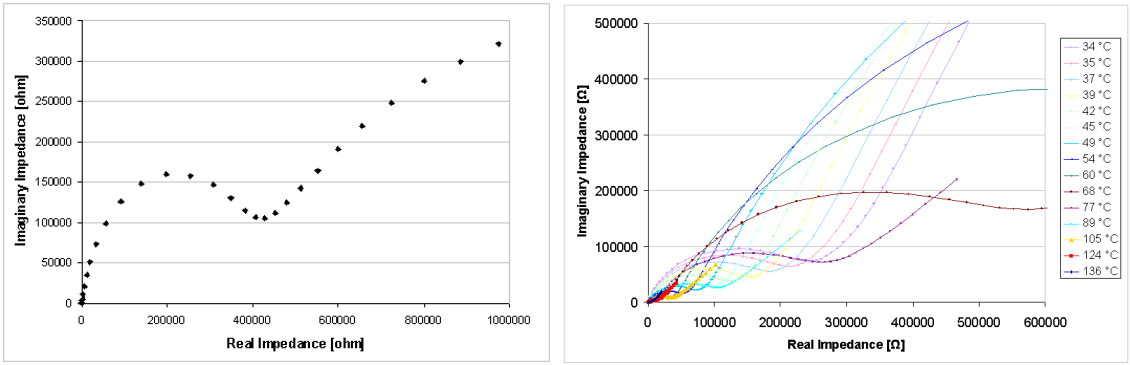

Fig. 6.7: Impedance plot for conductivity measurement at room temperature before activation energy measurement (left) and activation energy measurement between 34 °C and 136 °C (right) of $Li_5La_3Ta_2O_{12}$ *(thick pellet)*

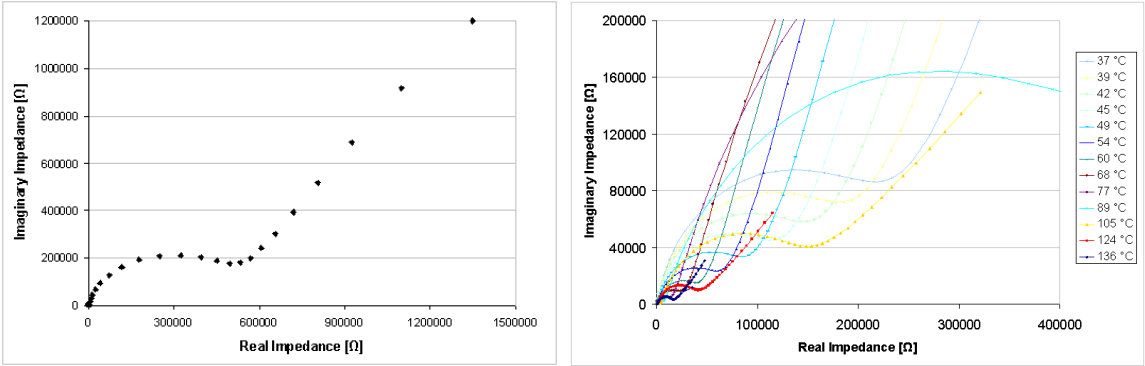

Fig. 6.8: Impedance plot for conductivity measurement at room temperature before activation energy measurement (left) and activation energy measurement between 37 °C and 136 °C (right) of $Li_5La_3Ta_2O_{12}$ *(thin pellet)*

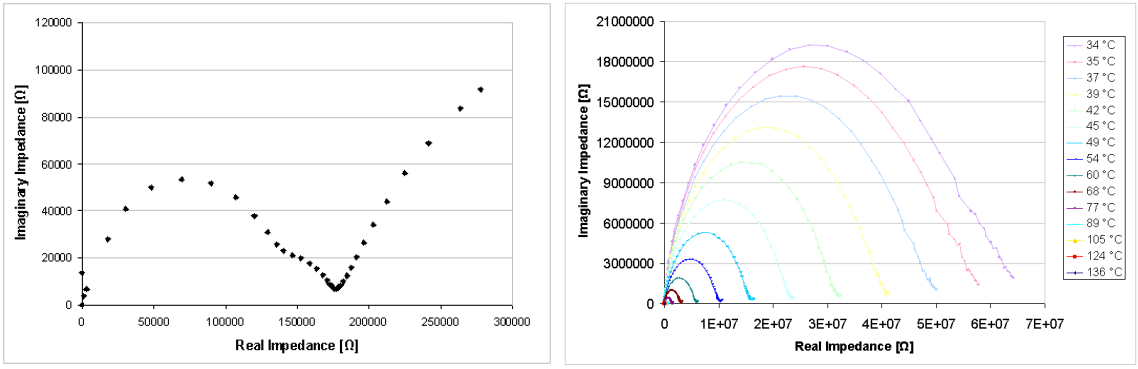

Fig. 6.9: Impedance plot for conductivity measurement at room temperature before activation energy measurement (left) and activation energy measurement between 34 °C and 136 °C (right) of $Li_{6.75}Ca_{025}La_{1.75}Ta_{0.5}Zr_{1.5}O_{12}$ *(thick pellet)*

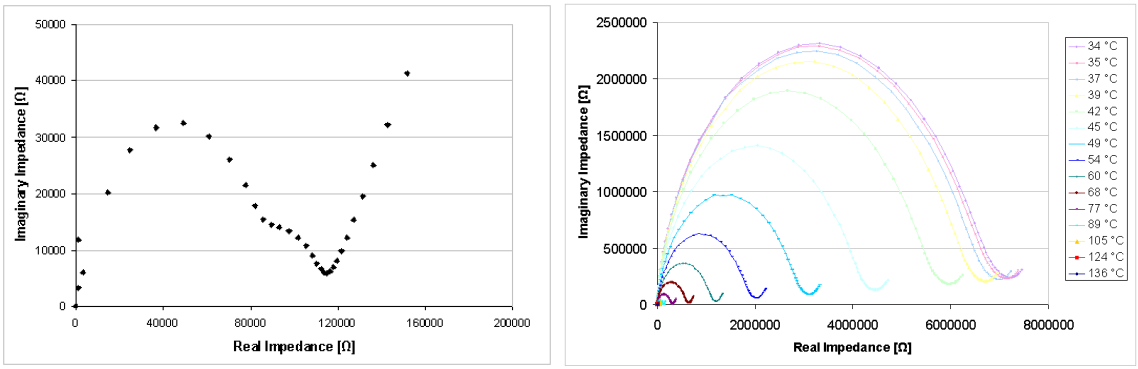

Fig. 6.10: Impedance plot for conductivity measurement at room temperature before activation energy measurement (left) and activation energy measurement between 34 °C and 136 °C (right) of $Li_{6.75}Ca_{025}La_{1.75}Ta_{0.5}Zr_{1.5}O_{12}$ *(thin pellet)*

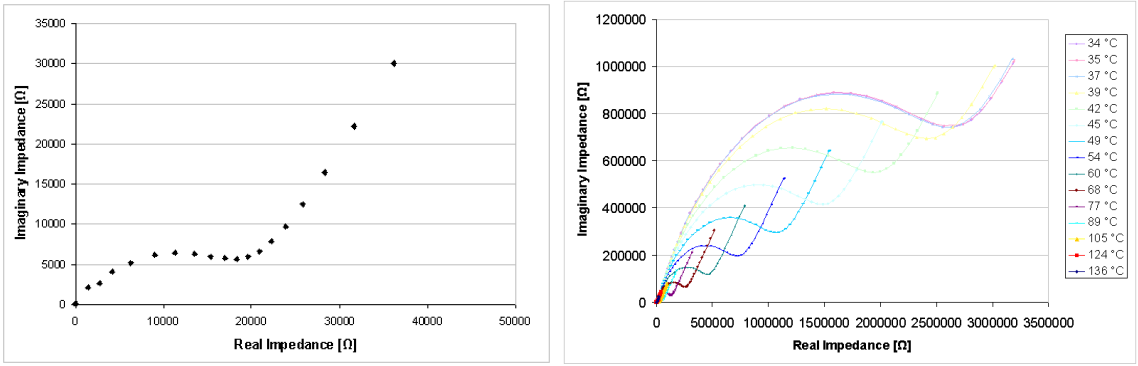

Fig. 6.11: Impedance plot for conductivity measurement at room temperature before activation energy measurement (left) and activation energy measurement between 34 °C and 136 °C (right) of $Li_{6.5}Ca_{0.5}La_{1.75}TaZrO_{12}$ *(thin pellet)*

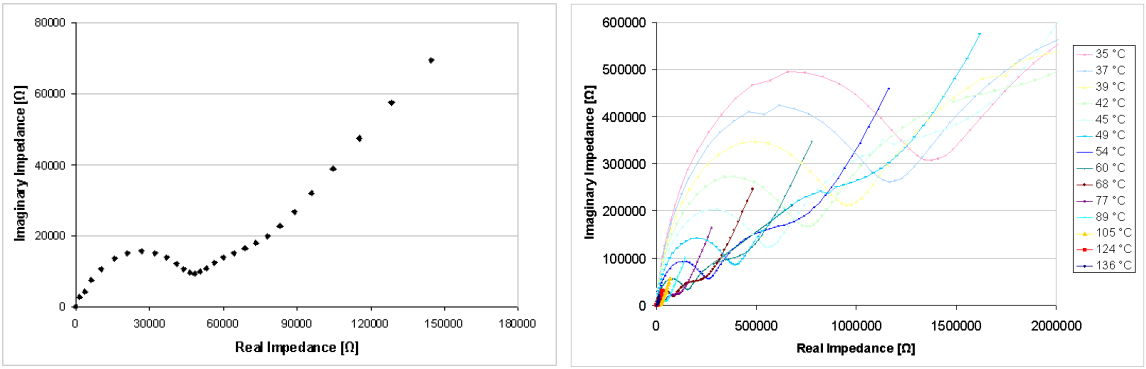

Fig. 6.12: Impedance plot for conductivity measurement at room temperature before activation energy measurement (left) and activation energy measurement between 35 °C and 136 °C (right) of $Li_{6.875}Sr_{0.125}La_{2.875}Ta_{0.25}Zr_{1.75}O_{12}$ *(thick pellet)*

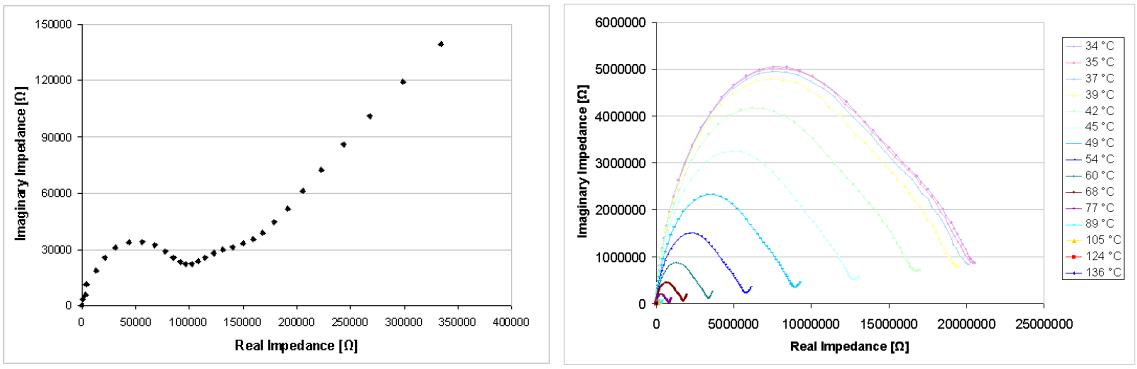

Fig. 6.13: Impedance plot for conductivity measurement at room temperature before activation energy measurement (left) and activation energy measurement between 34 °C and 136 °C (right) of $Li_{6.875}Sr_{0.125}La_{2.875}Ta_{0.25}Zr_{1.75}O_{12}$ *(thin pellet)*

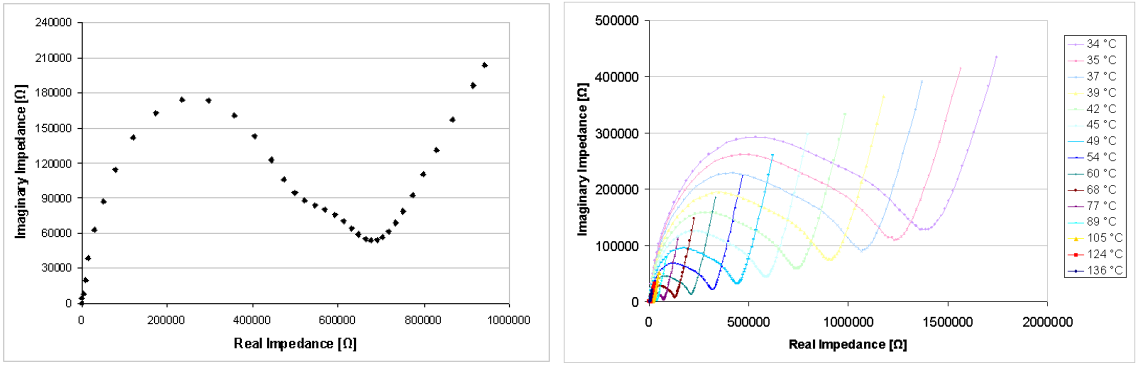

Fig. 6.14: Impedance plot for conductivity measurement at room temperature before activation energy measurement (left) and activation energy measurement between 34 °C and 136 °C (right) of $Li_{6.75}Sr_{0.25}La_{2.75}Ta_{0.5}Zr_{1.5}O_{12}$ *(thick pellet)*

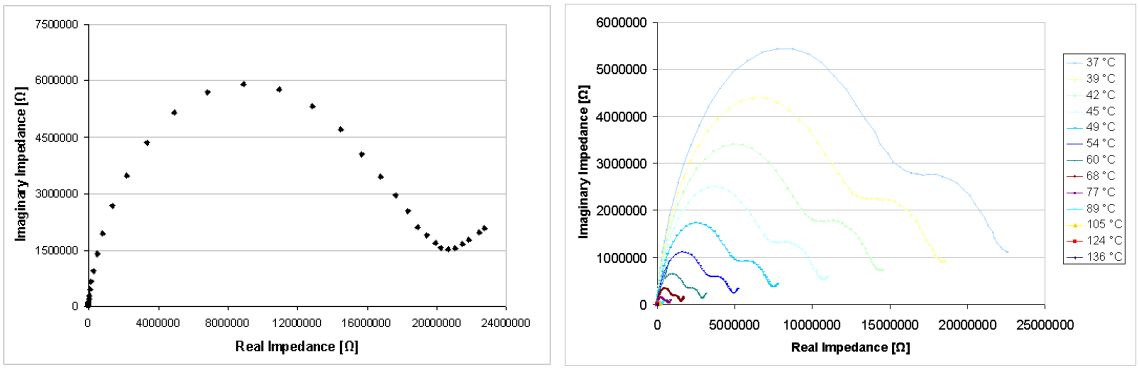

Fig. 6.15: Impedance plot for conductivity measurement at room temperature before activation energy measurement (left) and activation energy measurement between 37 °C and 136 °C (right) of $Li_{6.75}Sr_{0.25}La_{2.75}Ta_{0.5}Zr_{1.5}O_{12}$ *(thin pellet)*

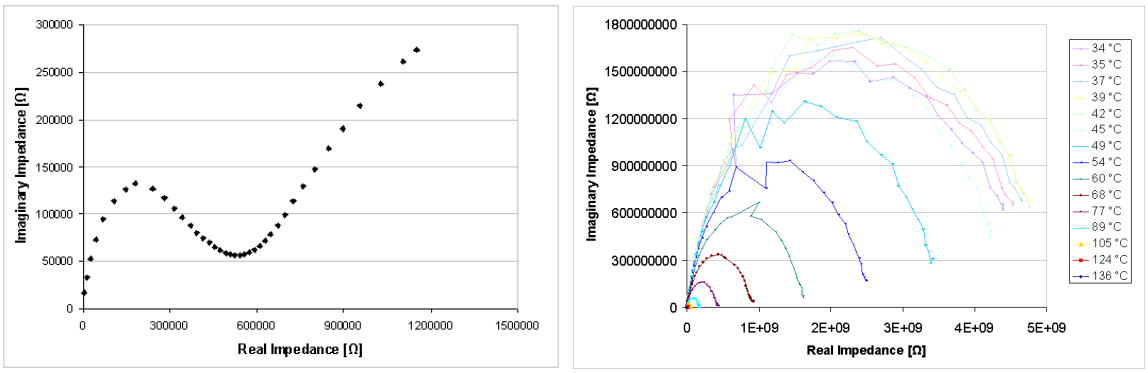

Fig. 6.16: Impedance plot for conductivity measurement at room temperature before activation energy measurement (left) and activation energy measurement between 34 °C and 136 °C (right) of $Li_{6.25}Sr_{0.25}La_{2.75}TaZrO_{12}$ *(thick pellet)*

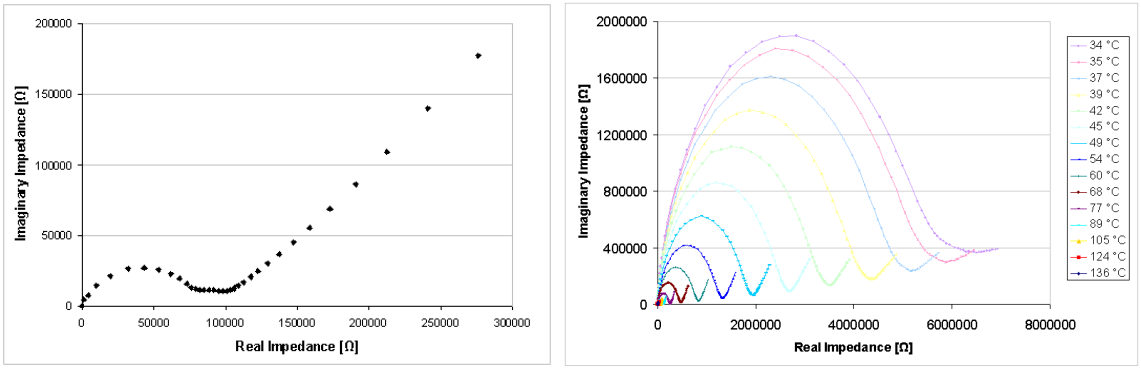

Fig. 6.17: Impedance plot for conductivity measurement at room temperature before activation energy measurement (left) and activation energy measurement between 34 °C and 136 °C (right) of $Li_{6.5}Sr_{0.5}La_{2.5}TaZrO_{12}$ *(thick pellet)*

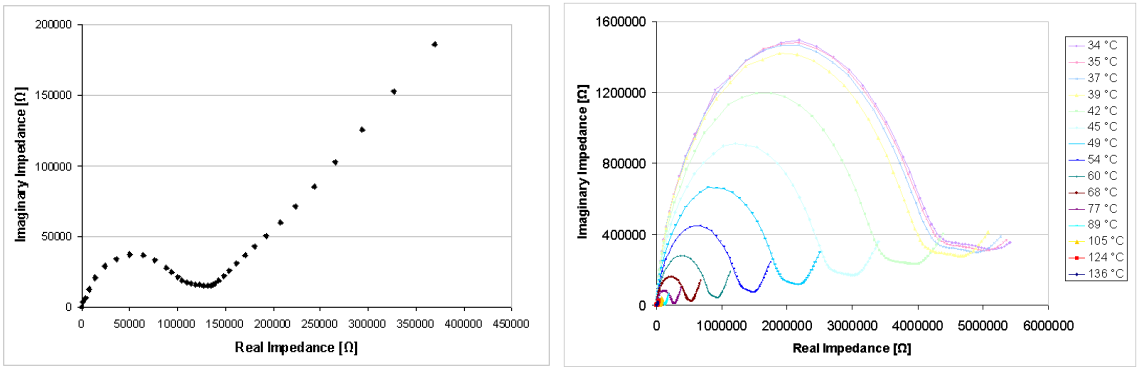

Fig. 6.18: Impedance plot for conductivity measurement at room temperature before activation energy measurement (left) and activation energy measurement between 34 °C and 136 °C (right) of $Li_{6.5}Sr_{0.5}La_{2.5}TaZrO_{12}$ *(thin pellet)*

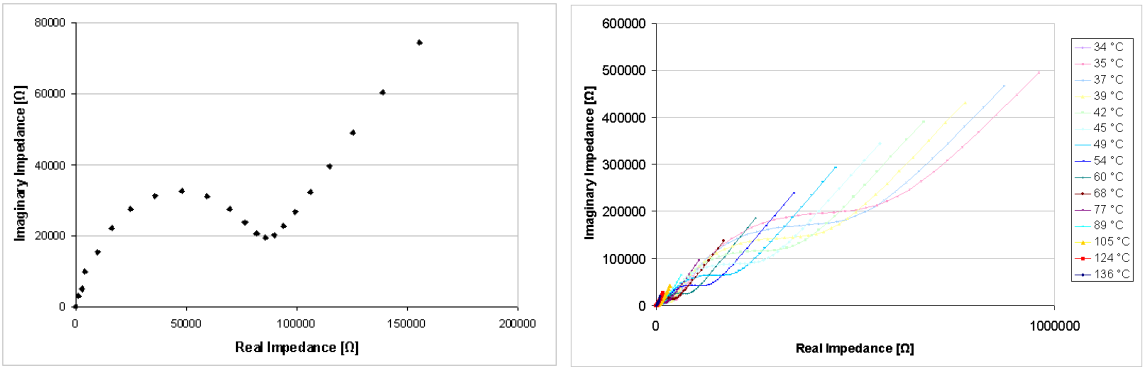

Fig. 6.19: Impedance plot for conductivity measurement at room temperature before activation energy measurement (left) and activation energy measurement between 34 °C and 136 °C (right) of $Li_{5.5}Sr_{0.5}La_{2.5}Ta_2O_{12}$ *(thick pellet)*

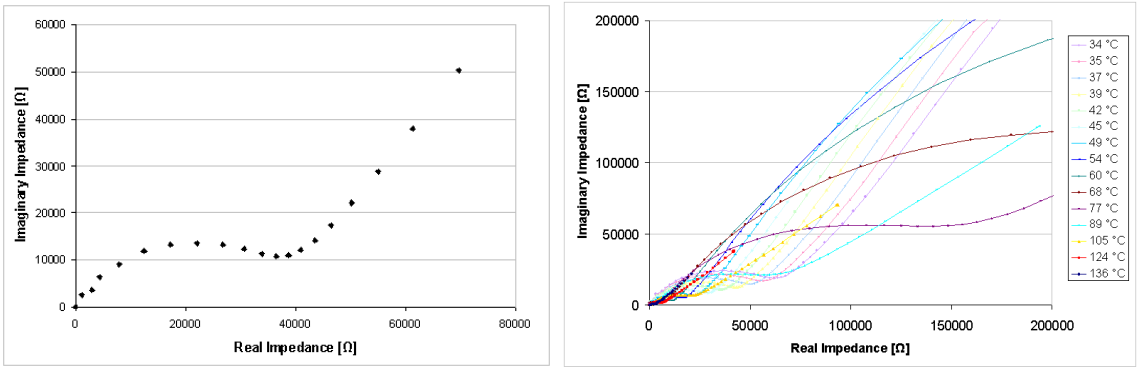

Fig. 6.20: Impedance plot for conductivity measurement at room temperature before activation energy measurement (left) and activation energy measurement between 34 °C and 136 °C (right) of $Li_{5.5}Sr_{0.5}La_{2.5}Ta_2O_{12}$ *(thin pellet)*

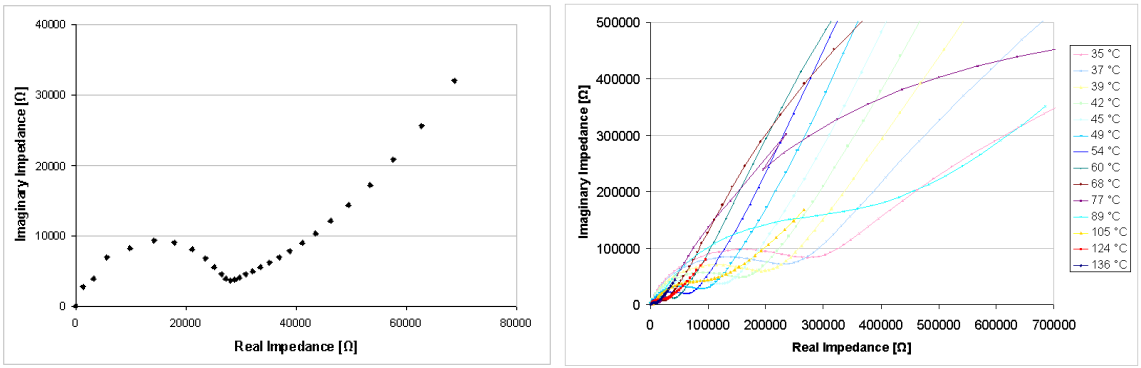

Fig. 6.21: Impedance plot for conductivity measurement at room temperature before activation energy measurement (left) and activation energy measurement between 35 °C and 136 °C (right) of $Li_6SrLa_2Ta_2O_{12}$ *(thick pellet)*

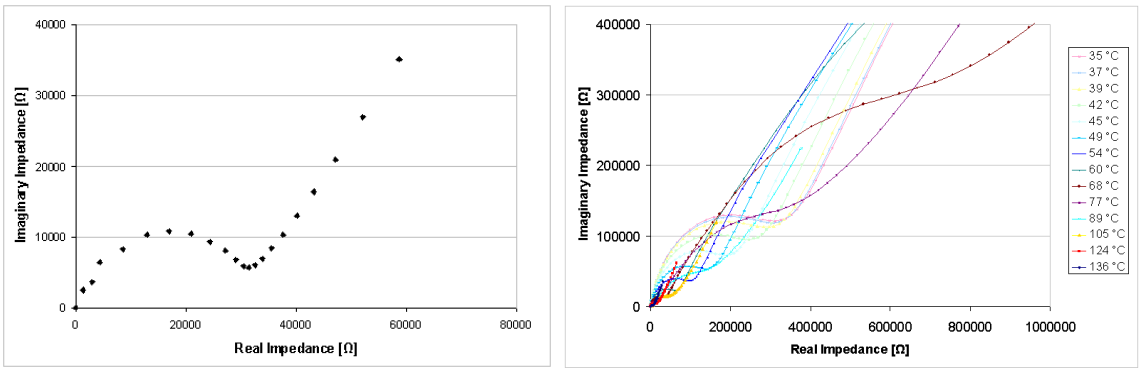

Fig. 6.22: Impedance plot for conductivity measurement at room temperature before activation energy measurement (left) and activation energy measurement between 35 °C and 136 °C (right) of $Li_6SrLa_2Ta_2O_{12}$ *(thin pellet)*

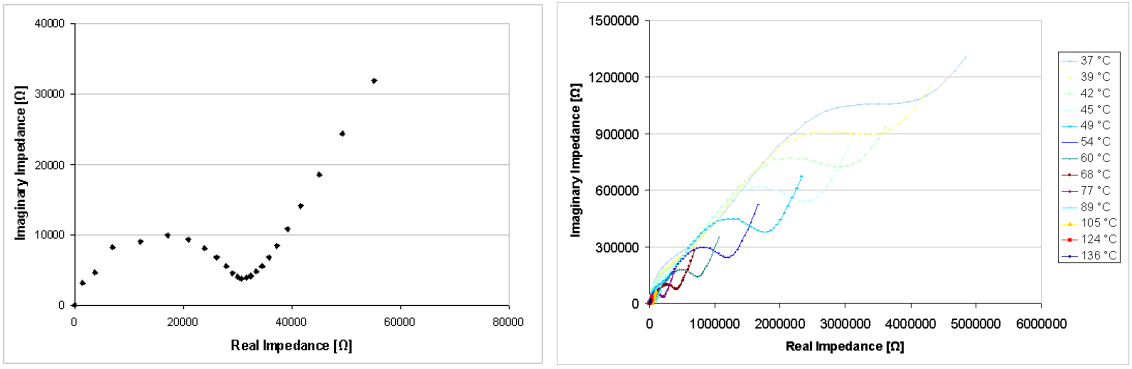

Fig. 6.23: Impedance plot for conductivity measurement at room temperature before activation energy measurement (left) and activation energy measurement between 37 °C and 136 °C (right) of $Li_{6.4}Sr_{1.4}La_{1.6}Ta_2O_{12}$ *(thick pellet)*

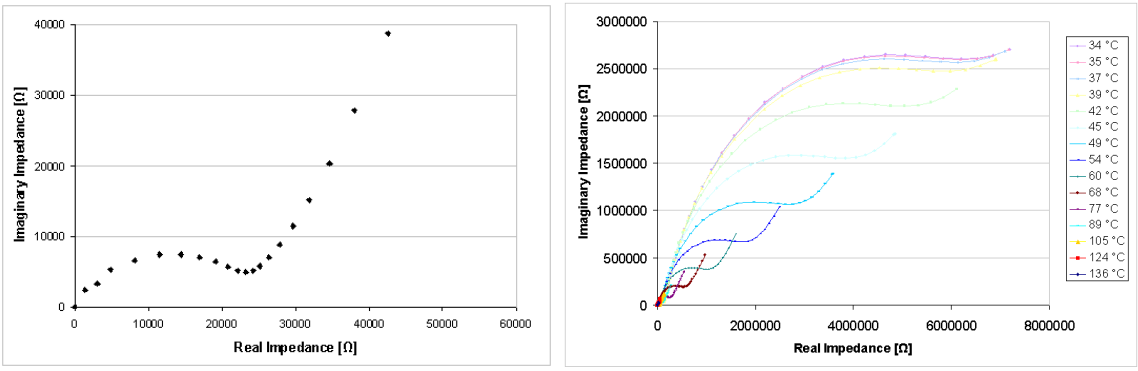

Fig. 6.24: Impedance plot for conductivity measurement at room temperature before activation energy measurement (left) and activation energy measurement between 34 °C and 136 °C (right) of $Li_{6.4}Sr_{1.4}La_{1.6}Ta_2O_{12}$ *(thin pellet)*

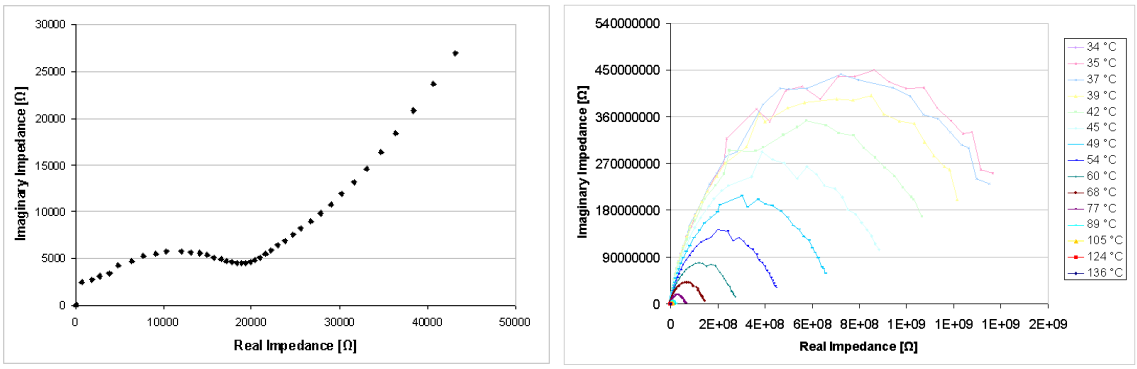

Fig. 6.25: Impedance plot for conductivity measurement at room temperature before activation energy measurement (left) and activation energy measurement between 34 °C and 136 °C (right) of $Li_{6.875}Ba_{0.125}La_{2.875}Ta_{0.25}Zr_{1.75}O_{12}$ *(thick pellet)*

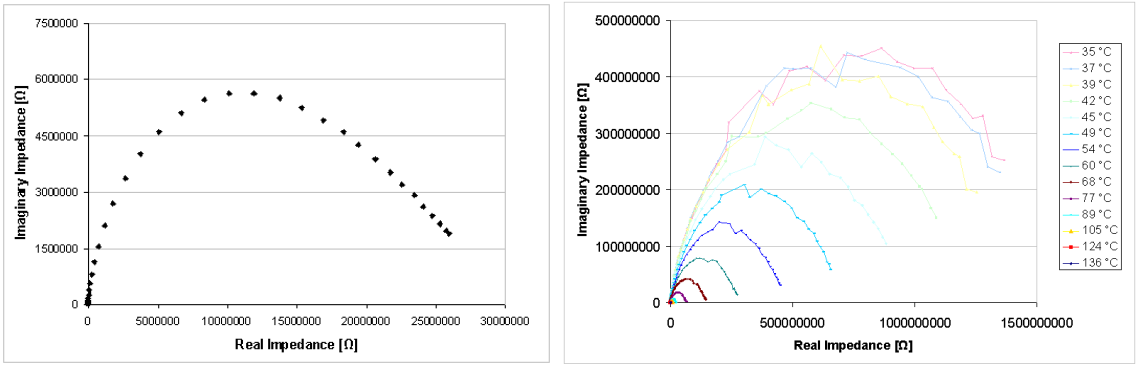

Fig. 6.26: Impedance plot for conductivity measurement at room temperature before activation energy measurement (left) and activation energy measurement between 35 °C and 136 °C (right) of $Li_{6.875}Ba_{0.125}La_{2.875}Ta_{0.25}Zr_{1.75}O_{12}$ *(thin pellet)*

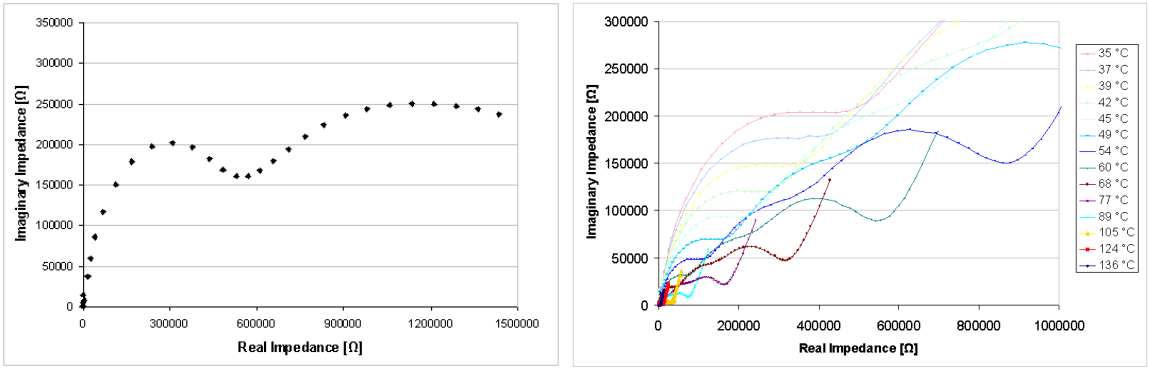

Fig. 6.27: Impedance plot for conductivity measurement at room temperature before activation energy measurement (left) and activation energy measurement between 35 °C and 136 °C (right) of $Li_{6.25}Ba_{0.25}La_{2.75}TaZrO_{12}$ *(thick pellet)*

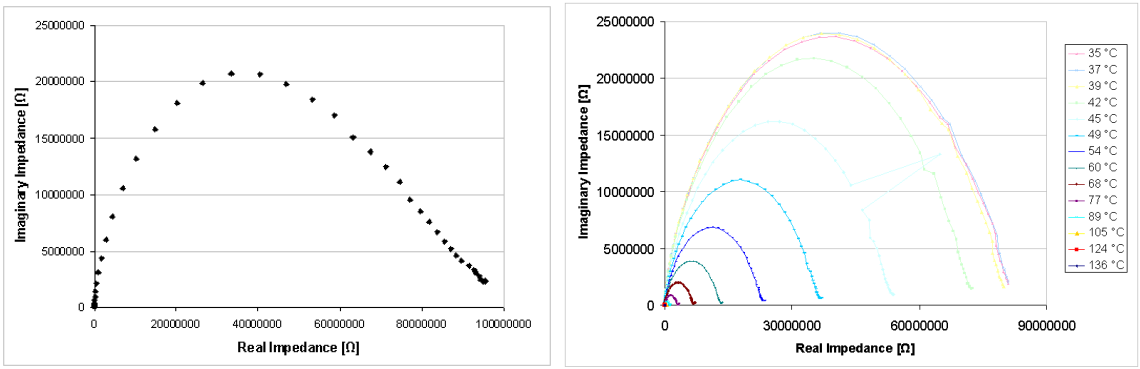

Fig. 6.28: Impedance plot for conductivity measurement at room temperature before activation energy measurement (left) and activation energy measurement between 35 °C and 136 °C (right) of $Li_{6.25}Ba_{0.25}La_{2.75}TaZrO_{12}$ *(thin pellet)*

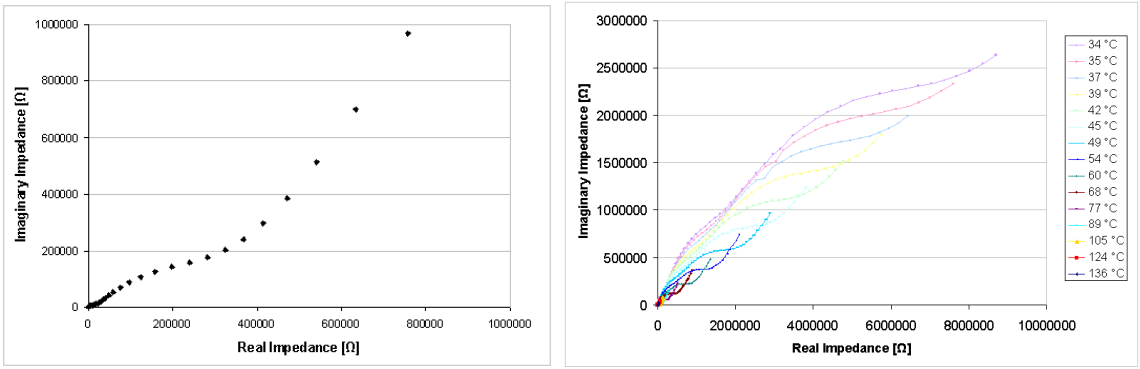

Fig. 6.29: Impedance plot for conductivity measurement at room temperature before activation energy measurement (left) and activation energy measurement between 34 °C and 136 °C (right) of $Li_{6.5}Ba_{0.5}La_{2.5}TaZrO_{12}$ *(thick pellet)*

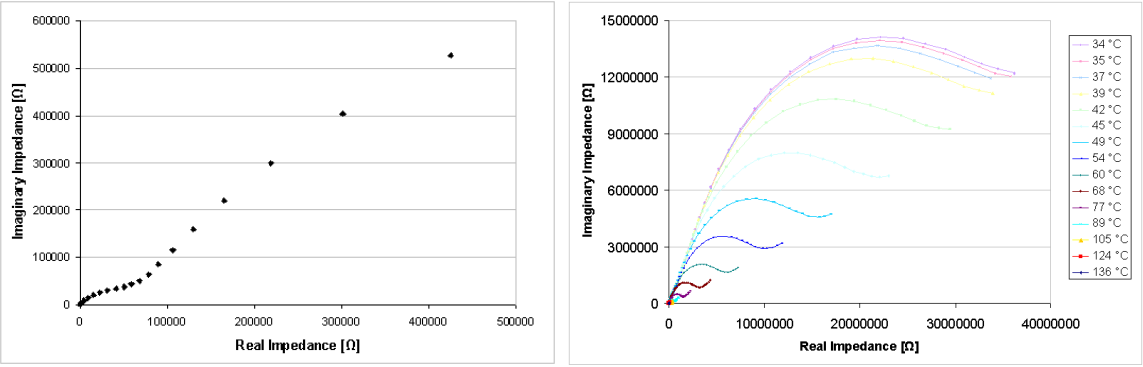

Fig. 6.30: Impedance plot for conductivity measurement at room temperature before activation energy measurement (left) and activation energy measurement between 34 °C and 136 °C (right) of $Li_{6.5}Ba_{0.5}La_{2.5}TaZrO_{12}$ *(thin pellet)*

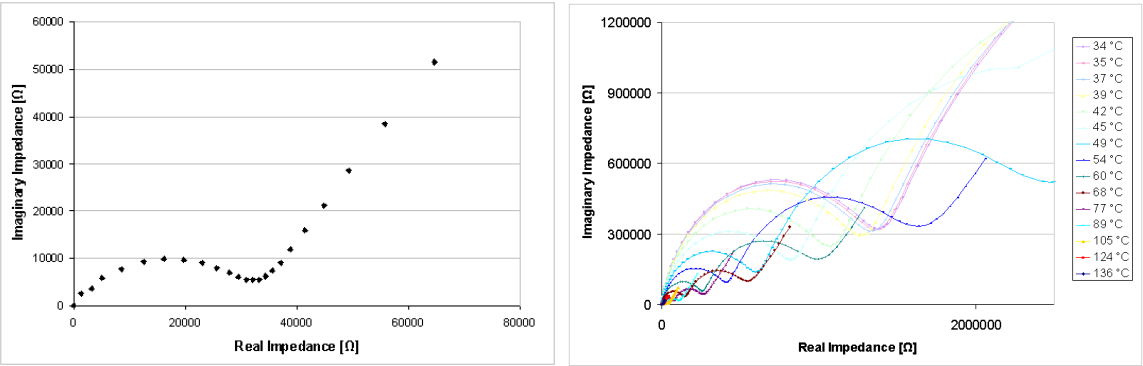

Fig. 6.31: Impedance plot for conductivity measurement at room temperature before activation energy measurement (left) and activation energy measurement between 34 °C and 136 °C (right) of $Li_{5.5}Ba_{0.5}La_{2.5}Ta_2O_{12}$ *(thin pellet)*

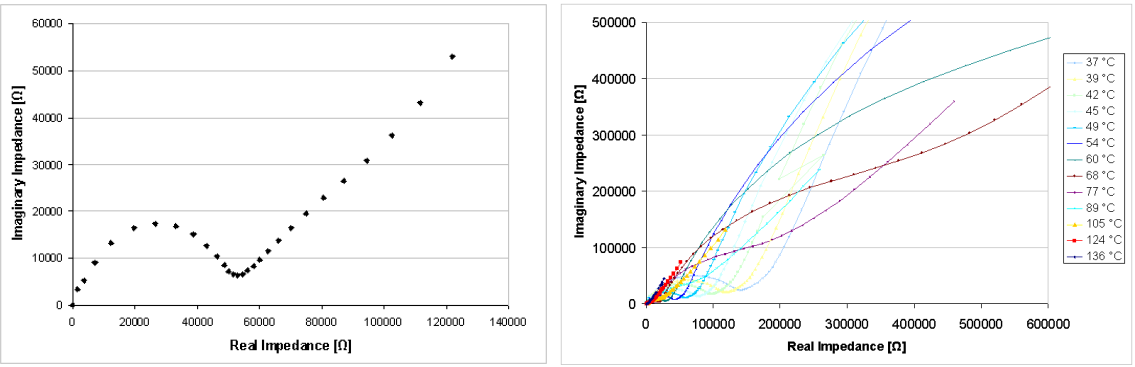

Fig. 6.32: Impedance plot for conductivity measurement at room temperature before activation energy measurement (left) and activation energy measurement between 37 °C and 136 °C (right) of $Li_6BaLa_2Ta_2O_{12}$ *(thick pellet)*

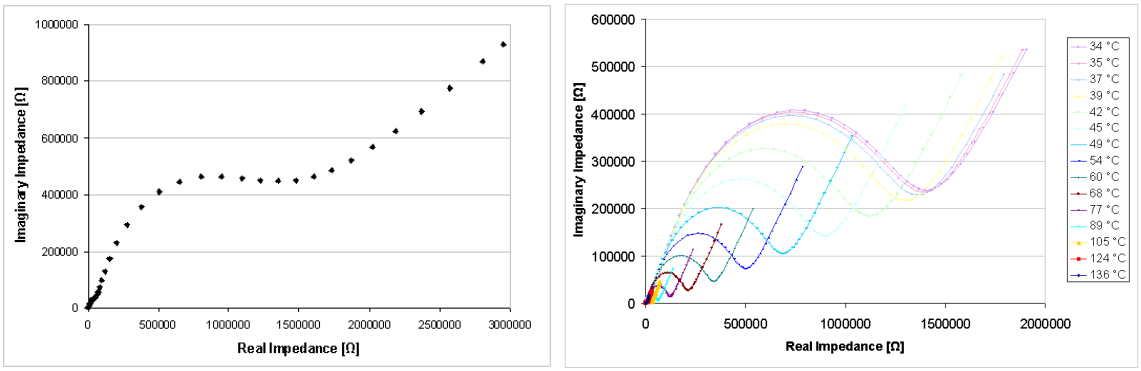

Fig. 6.33: Impedance plot for conductivity measurement at room temperature before activation energy measurement (left) and activation energy measurement between 34 °C and 136 °C (right) of $Li_6BaLa_2Ta_2O_{12}$ *(thin pellet)*

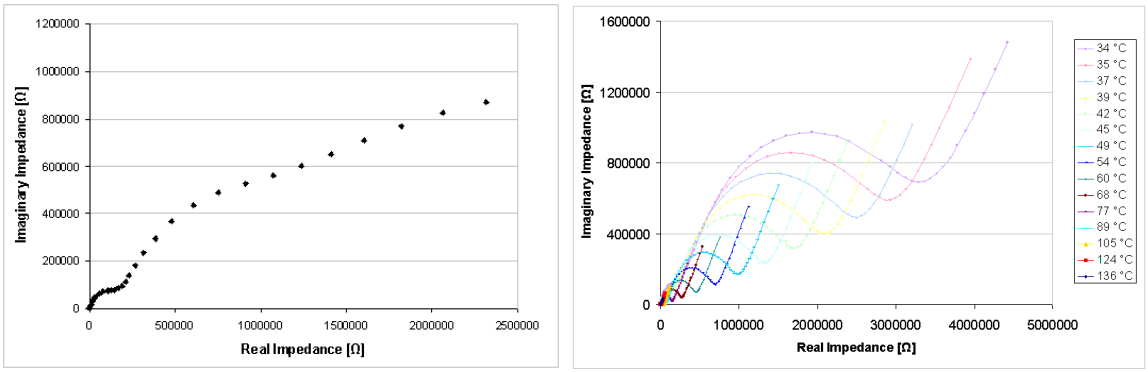

Fig. 6.34: Impedance plot for conductivity measurement at room temperature before activation energy measurement (left) and activation energy measurement between 34 °C and 136 °C (right) of $Li_{6.4}Ba_{1.4}La_{1.6}Ta_2O_{12}$ *(thick pellet)*

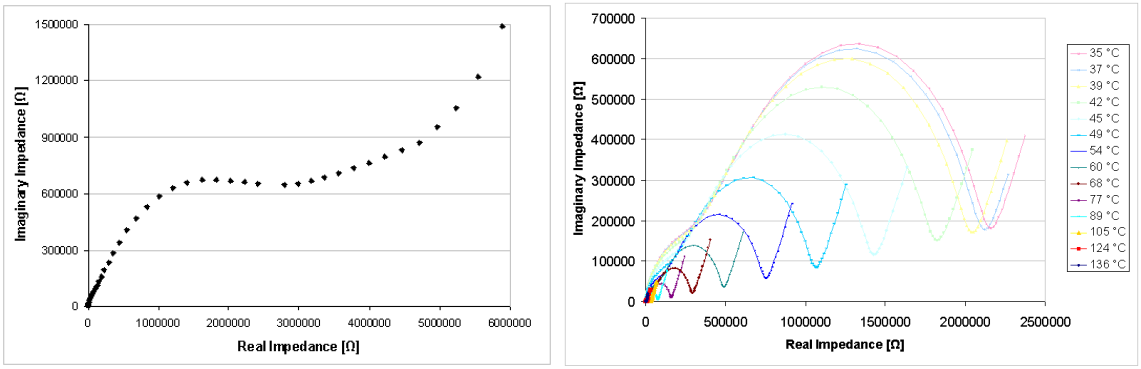

Fig. 6.35: Impedance plot for conductivity measurement at room temperature before activation energy measurement (left) and activation energy measurement between 35 °C and 136 °C (right) of $Li_{6.4}Ba_{1.4}La_{1.6}Ta_2O_{12}$ *(thin pellet)*

6.2. Appendix 2 – Materialographic investigation of garnet-like materials

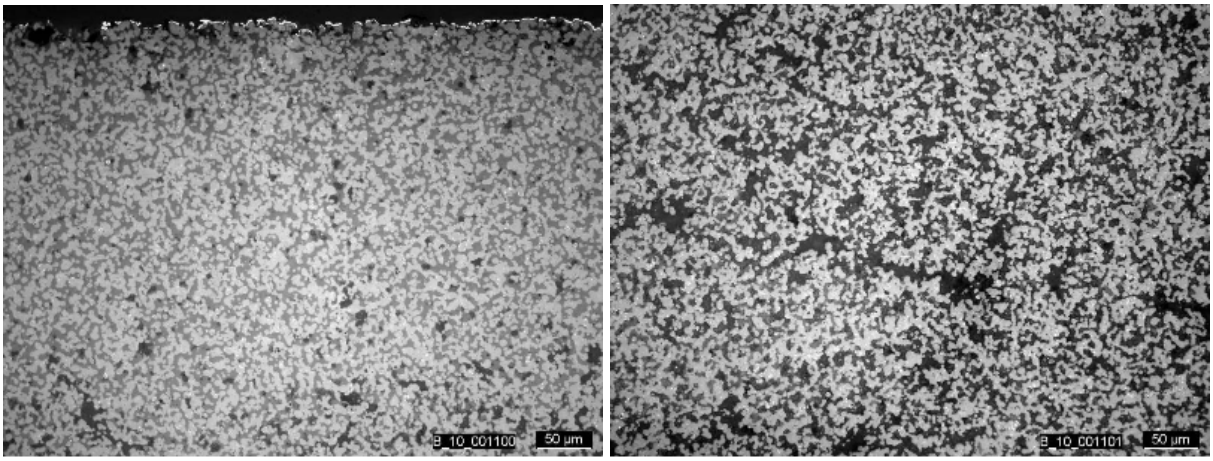

Fig.6.36: Microstructural investigation of $Li_{6.5}La_3Ta_{0.5}Zr_{1.5}O_{12}$ *(thick pellet) by light microscopy.*

Left picture: edge, Right picture: middle.

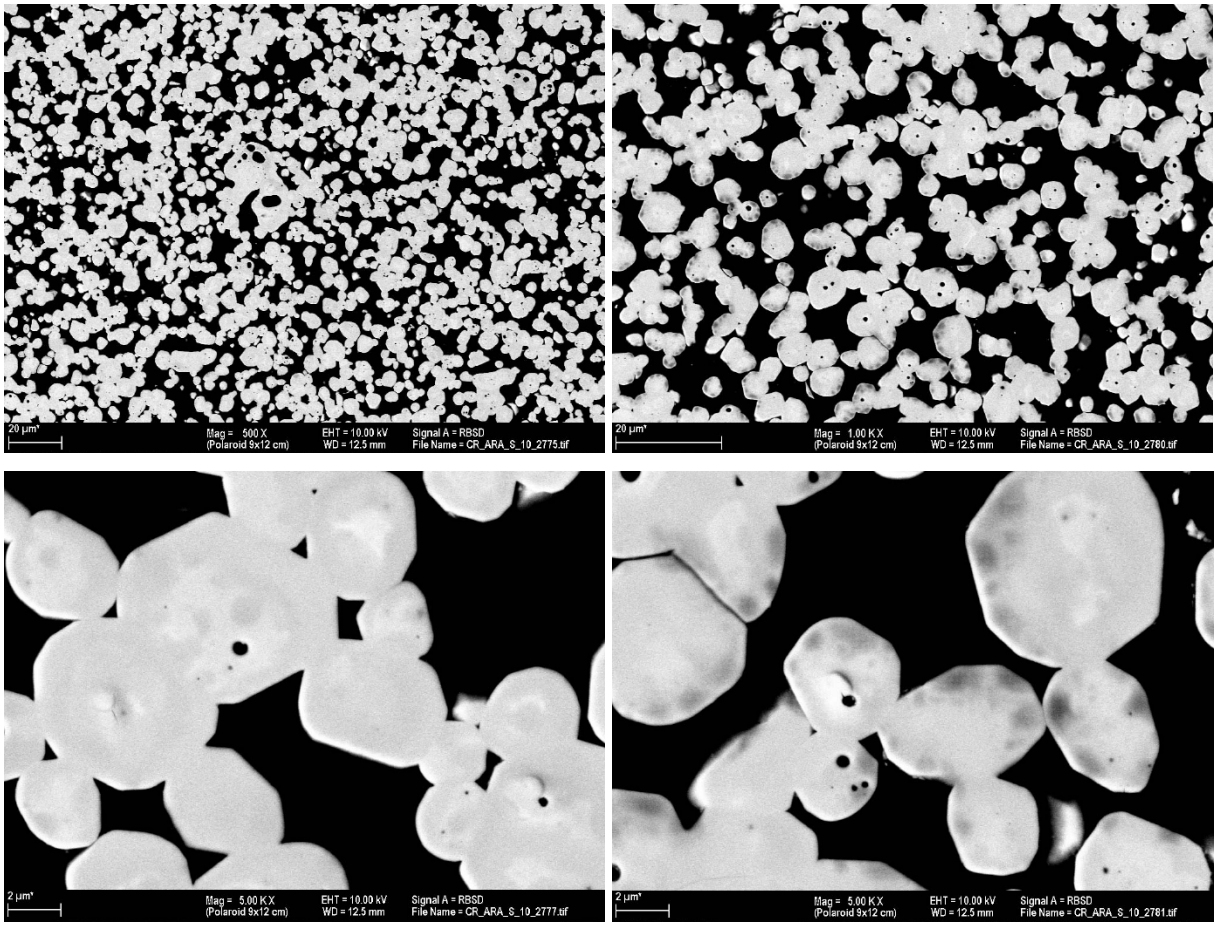

Fig.6.37: Microstructural investigation of $Li_{6.5}La_3Ta_{0.5}Zr_{1.5}O_{12}$ *(thick pellet-middle) by SEM.*

Left pictures: edge, Right pictures: middle

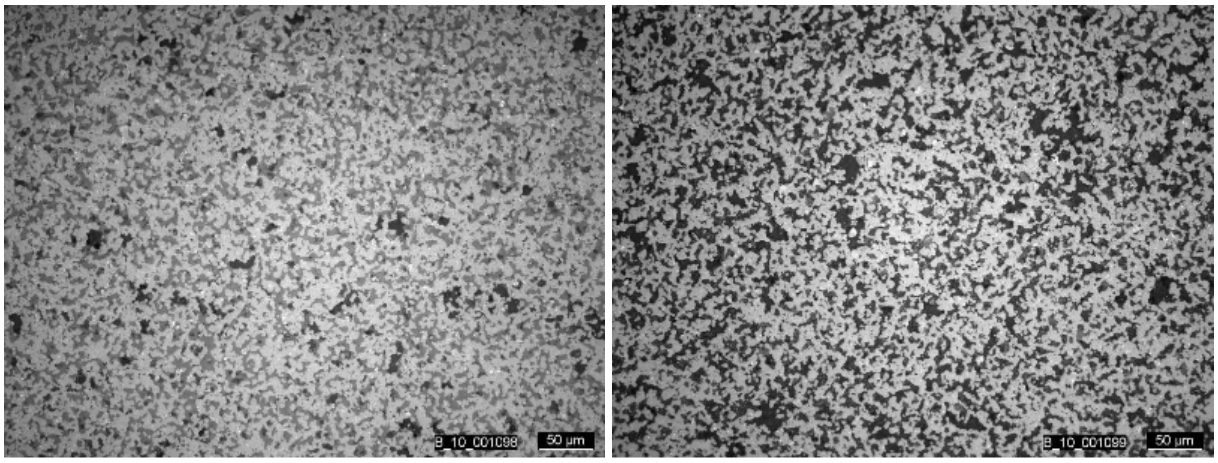

Fig.6.38: Microstructural investigation of $Li_6La_3TaZrO_{12}$ *(thick pellet) by light microscopy.*

Left picture: edge, Right picture: middle.

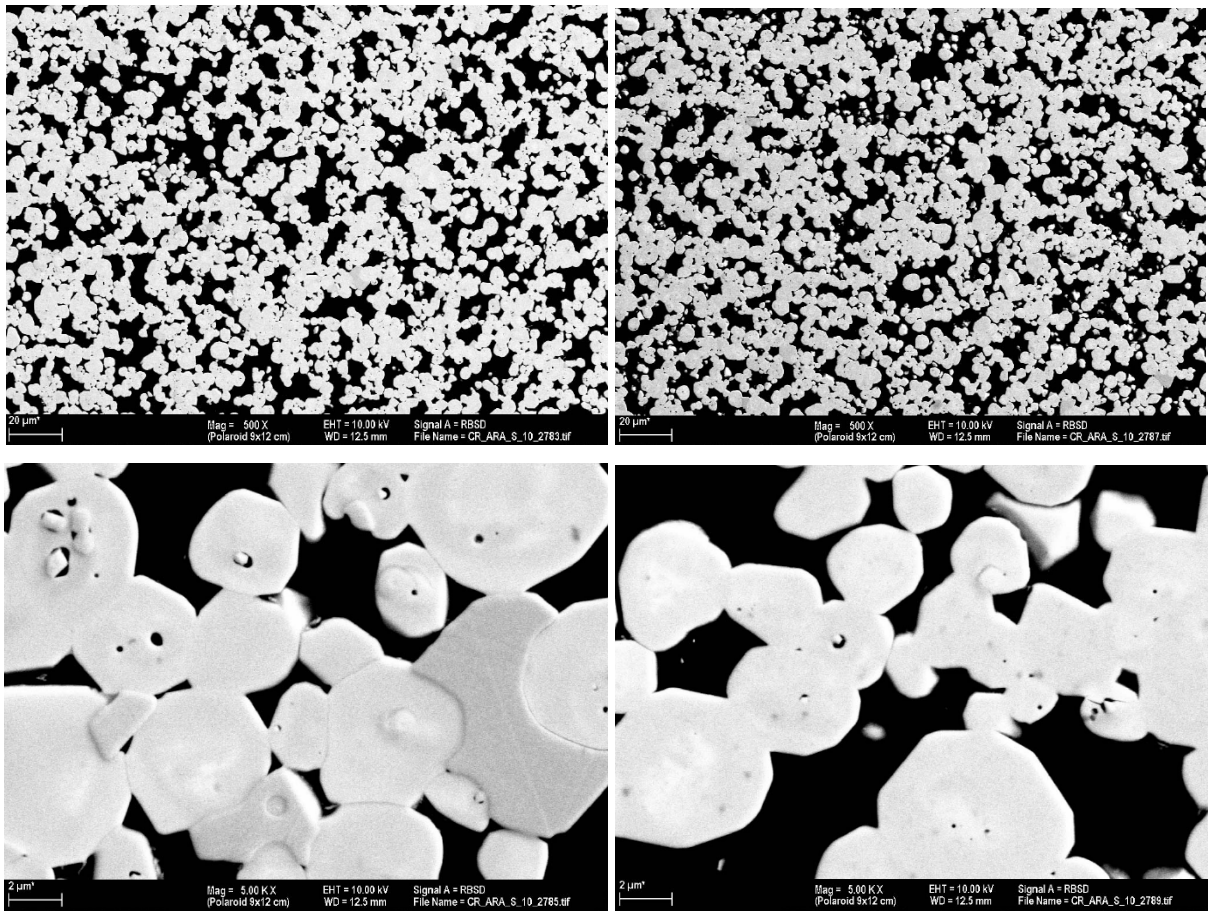

Fig.6.39: Microstructural investigation of $Li_6La_3TaZrO_{12}$ *(thick pellet-middle) by SEM.*

Left pictures: edge, Right pictures: middle

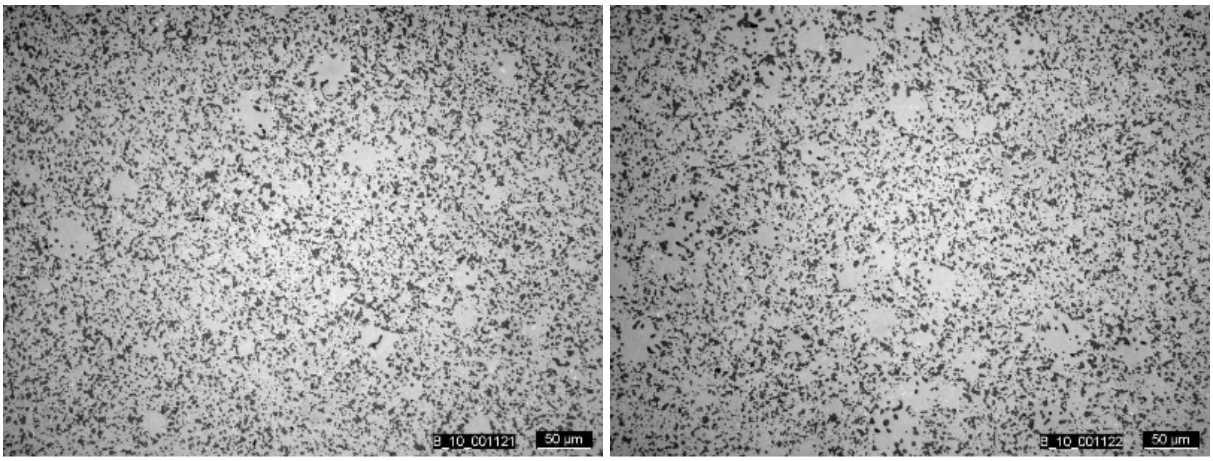

Fig.6.40: Microstructural investigation of $Li_5La_3Ta_2O_{12}$ (thick pellet) by light microscopy. Left picture: edge, Right picture: middle.

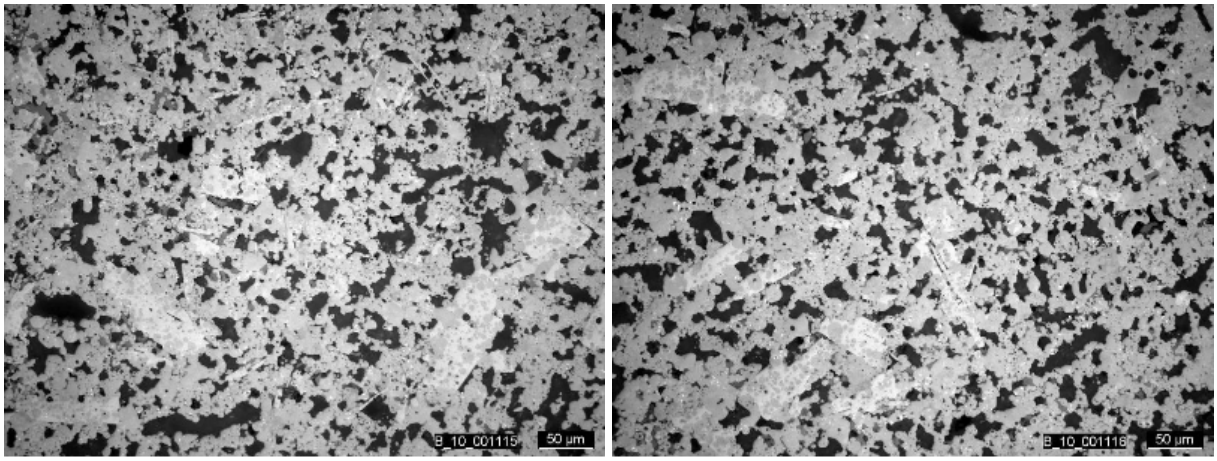

Fig.6.41: Microstructural investigation of $Li_{6.75}Sr_{0.25}La_{2.75}Ta_{0.5}Zr_{1.5}O_{12}$ (thick pellet) by light microscopy. Left picture: edge, Right picture: middle.

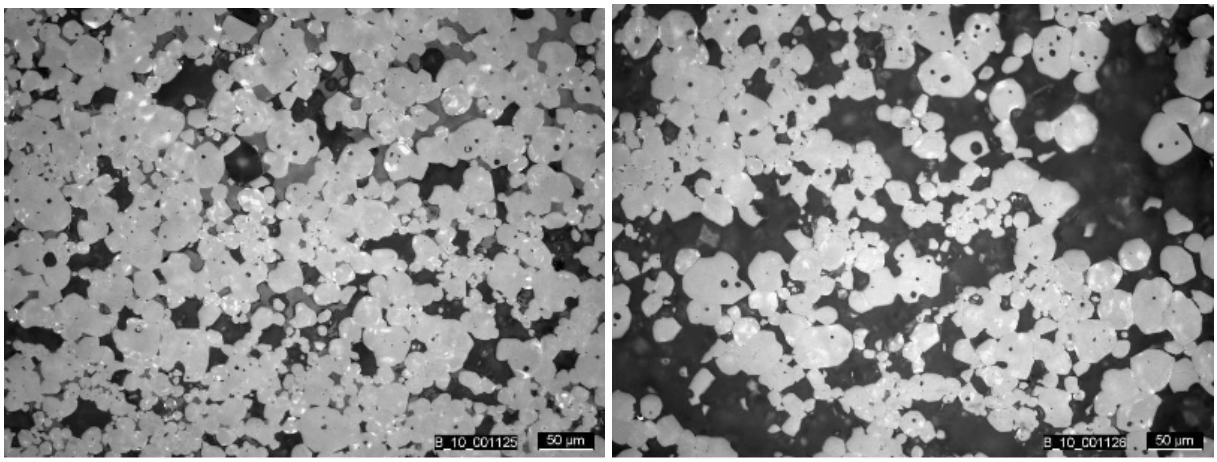

Fig.6.42: Microstructural investigation of $Li_{5.5}Sr_{0.5}La_{2.5}Ta_2O_{12}$ (thick pellet) by light microscopy. Left picture: edge, Right picture: middle.

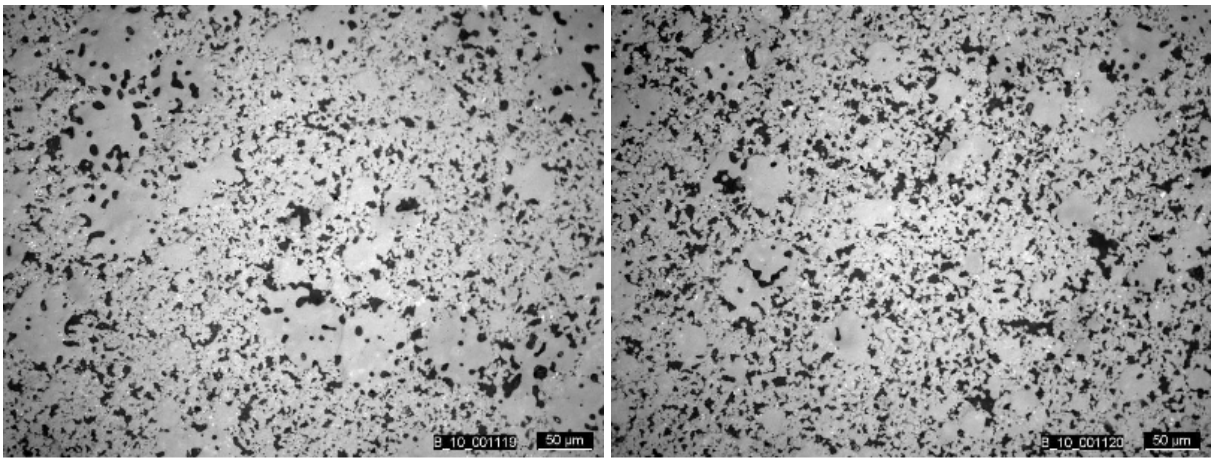

Fig.6.43: Microstructural investigation of $Li_6SrLa_2Ta_2O_{12}$ *(thick pellet) by light microscopy. Left picture: edge, Right picture: middle.*

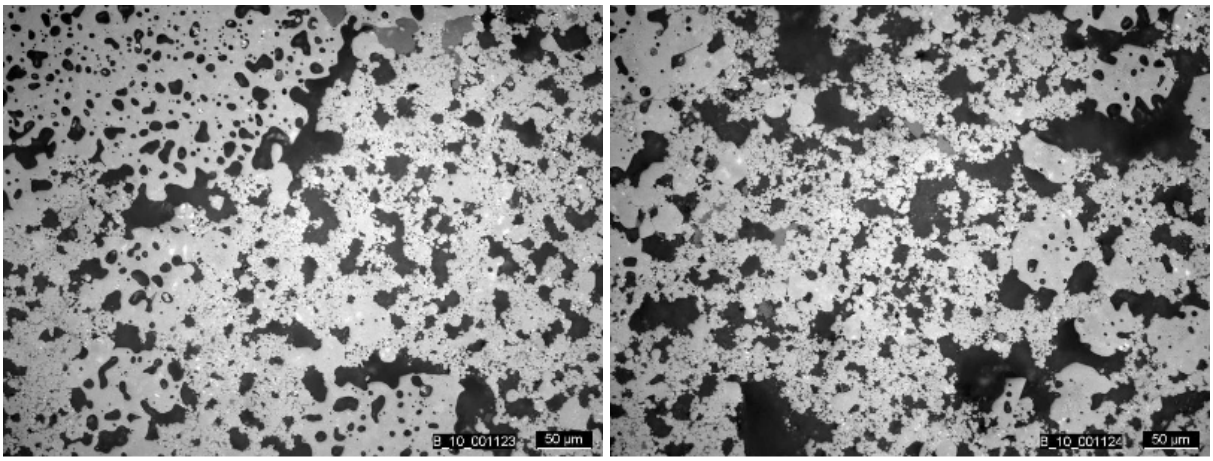

Fig.6.44: Microstructural investigation of $Li_{6.4}Sr_{1.4}La_{1.6}Ta_2O_{12}$ *(thick pellet) by light microscopy. Left picture: edge, Right picture: middle.*

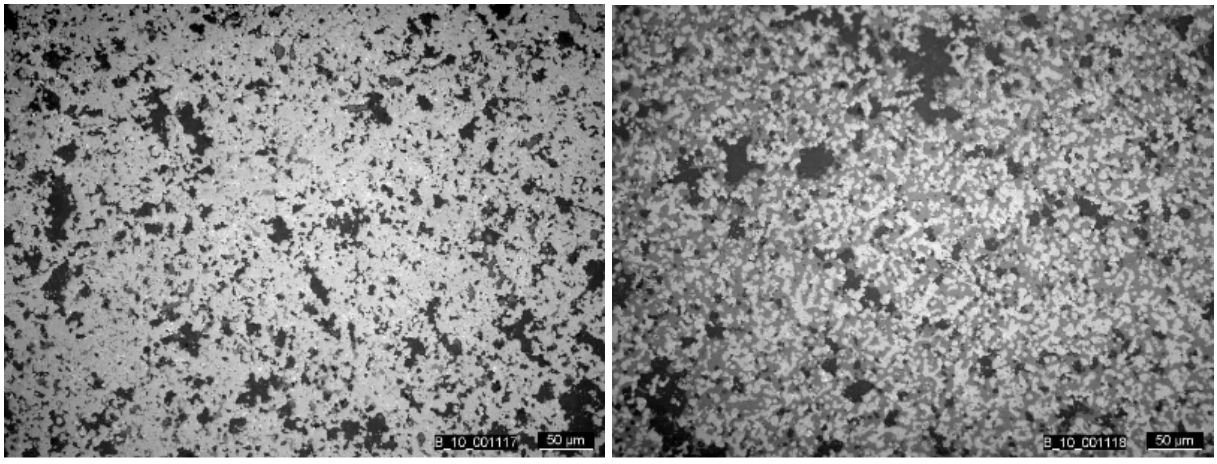

Fig.6.45: Microstructural investigation of $Li_{6.25}Ba_{0.25}La_{2.75}TaZrO_{12}$ *(thick pellet) by light microscopy. Left picture: upper edge, Right picture: lower edge.*

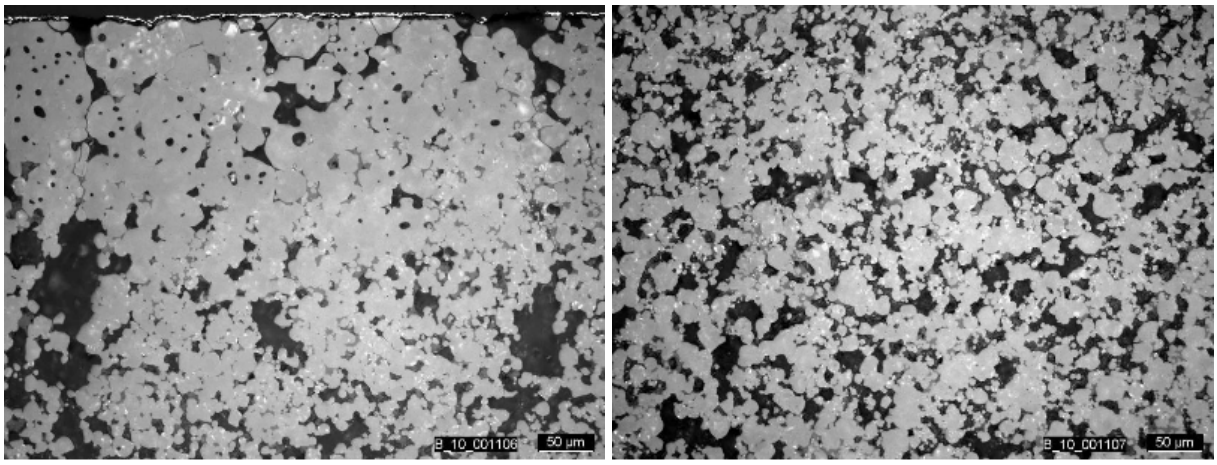

Fig.6.46: Microstructural investigation of $Li_{6.875}Ba_{0.125}La_{2.875}Ta_{0.25}Zr_{1.75}O_{12}$ *(thick pellet) by light microscopy. Left picture: edge, Right picture: middle.*

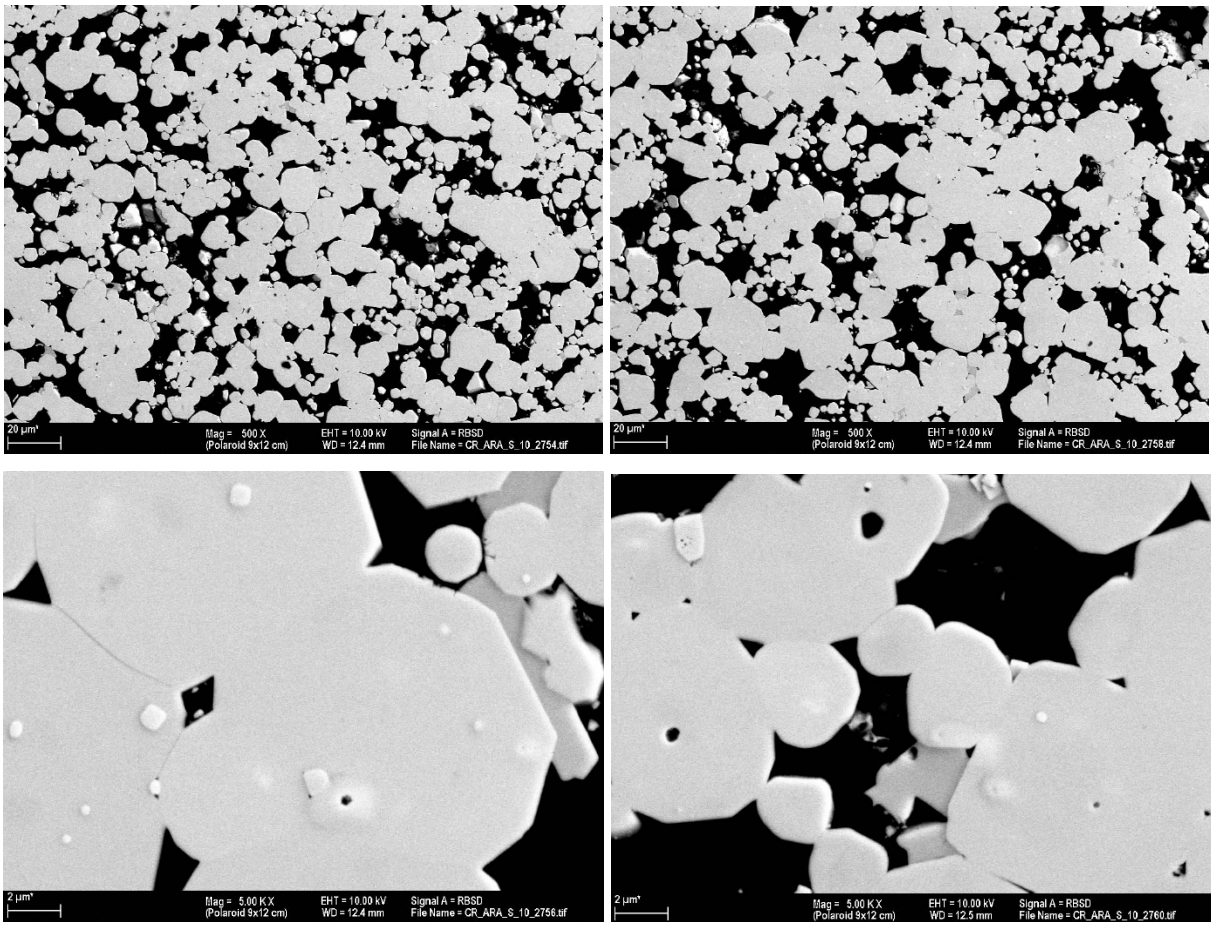

Fig.6.47: Microstructural investigation of $Li_{6.875}Ba_{0.125}La_{2.875}Ta_{0.25}Zr_{1.75}O_{12}$ *(thick pellet-middle) by SEM.. Left pictures: edge, Right pictures: middle*

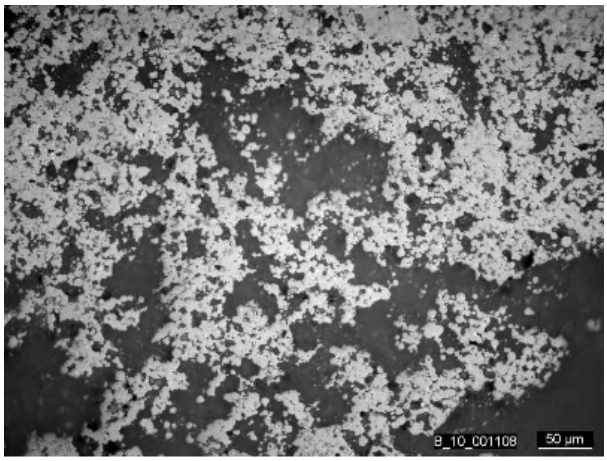

Fig.6.48: Microstructural investigation of $Li_{6.5}Ba_{0.5}La_{2.5}TaZrO_{12}$ *(thick pellet) by light microscopy.*

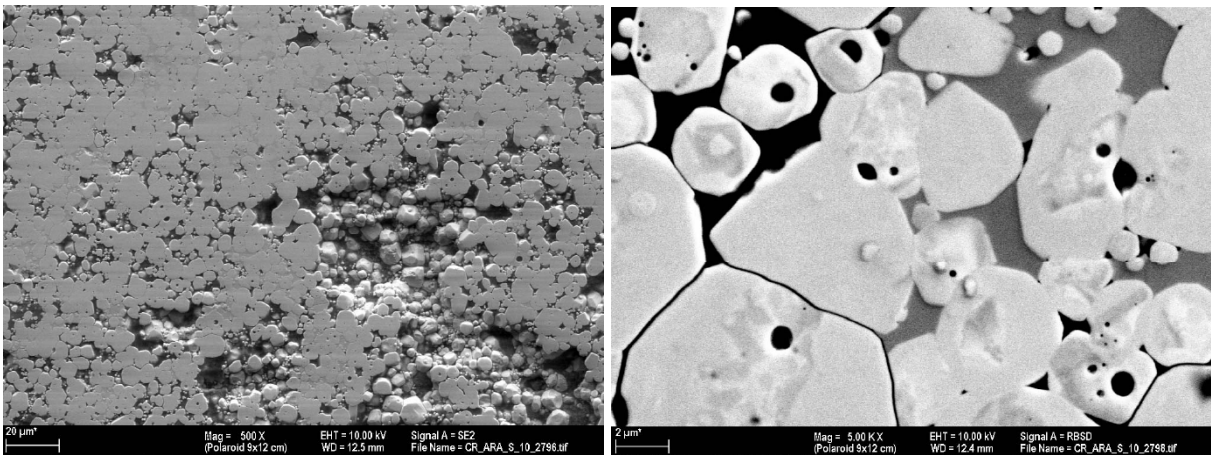

Fig.6.49: Microstructural investigation of $Li_{6.5}Ba_{0.5}La_{2.5}TaZrO_{12}$ *(thick pellet-middle) by SEM.*

7. Bibliography

[1] C. H. Hamann, W. Vielstich, *Elektrochemie*, 4., vollständig überarbeitete und aktualisierte Auflage, Viley-VCH, **2005**

[2] Batterien für Elektro- und Hybridfahrzeuge – Lithium Ion www.tuebke.de/folien/lithium.pdf

[3] A. Jossen, W. Weydanz, *Moderne Akkumulatoren richtig einsetzen*, 1. Auflage, Ubooks Verlag, **2006**

[4] M. Winter, K.-C. Möller, *Primäre und wieder aufladbare Lithiumbatterien*, Institut für Chemische Technologie Anorganischer Stoffe, TU Graz, **2005**

[5] M. Winter, J. O. Besenhard, *Wiederaufladbare Batterien*, Chemie in unserer Zeit 33, 320-332, **1999**

[6] W. D. Kingery, H. K. Bowen, D. R. Uhlmann, Introduction to Ceramics, 2nd edition, John Wiley&Sons, **1976**

[7] J. R. Macdonald, *Impedance Spectroscopy – Emphasizing solid materials and systems*, John Wiley & Sons, Inc., **1987**

[8] M. Yoshio, R. J. Brodd, A. Kozawa, *Lithium-Ion Batteries – Science and Technologies*, Springer Science + Business Media, LLC **2009**

[9] C. E. Mortimer, U. Müller, *Chemie – das Basiswissen der Chemie*, 8., komplett überarbeitete und erweiterte Auflage, Thieme, **2003**

[10] www.practicalchemistry.org/experiments/rechargeable-commercial-cells-the-lead-acid-accumulator,180,EX.html

[11] G. Gutmann, *Session3: Lithiumakkumulatoren*, ZSW Ulm

[12] www.uni-salzburg.at/portal/page?_pageid=805,261552&_dad=portal&_schema=PORTAL

[13] F. Frey, *Neutronenbeugung – eine Einführung für Chemiker*, Department für Geo- und Umweltwissenschaften, Ludwig-Maximilians-Universität München

[14] Gamry Instruments, Basics of Electrochemical Impedance Spectroscopy, www.gamry.com

[15] B. A. Boucamp, *Electrochemical Impedance Spectroscopy*, Department of Science and Technology, University of Twente, **2008**

[16] L. Koll, *Praktikum Werkstoffkunde – Rasterelektronenmikroskopie*, Lehrstuhl für Werkstoffkunde und Werkstoffmechanik, Technische Universität München

[17] R. Murugan, V. Thangadurai, W. Weppner, *Effect of lithium ion content on the lithium ion conductivity of the garnet-like structure* $Li_{5+x}BaLa_2Ta_2O_{11.5+0.5x}$ *(x=0-2)*, Applied Physics A 91, 615-620, **2008**

[18] A. Ramzy, V. Thangadurai, *Tailor-Made Development of Fast Li Ion Conducting Garnet-Like Solid Electrolytes*, Applied Materials & Interfaces 2, No.2, 385-390, **2010**

[19] R. Murugan, V. Thangadurai, W. Weppner, *Schnelle Lithiumionenleitung in granatartigem* $Li_7La_3Zr_2O_{12}$, Angewandte Chemie 119, 7925-7928, **2007**

[20] R. Murugan, V. Thangadurai, W. Weppner, *Lattice Parameter and Sintering Temperature Dependence of Bulk and Grain-Boundary Conduction of Garnet-like Solid Li-Electrolytes*, Journal of The Electrochemical Society 155 (1), A90-A101, **2008**

[21] Jeffrey W. Fergus, *Ceramic and Polymeric Solid Electrolytes for Lithium Ion Batteries*, Journal of Power Sources 195, 4554-4569, **2010**

[22] J. Awaka, N. Kijima, H. Hayakawa, J. Akimoto, *Synthesis and structure analysis of tetragonal* $Li_7La_3Zr_2O_{12}$ *with a garnet-related type structure*, Journal of Solid State Chemistry 182, 2046-2052, **2009**

[23] A. Kaeriyama, H. Munakata, K. Kajihara, K. Kanamura, Y. Sato, T. Yoshida, *Fabrication and evaluation of electrochemical characteristics of $Li_7La_3Ta_2O_{12}$ solid electrolyte*, **2008**

[24] J. Percival, D. Apperley, P.R. Slater, *Synthesis and structural characterisation of the Li on conducting garnet-related systems, $Li_6ALa_2Nb_2O_{12}$ (A=Ca, Sr)*, Solid State Ionics 179, 1693-1696, **2008**

[25] J. Awaka, N. Kijima, Y. Takahashi, H. Hayakawa, J. Akimoto, *Synthesis and crystallographic studies of garnet-related lithium-ion conductors $Li_6CaLa_2Ta_2O_{12}$ and $Li_6BaLa_2Ta_2O_{12}$*, Solid State Ionics 180, 602-606, **2009**

[26] R. Murugan, W. Weppner, P. Schmid-Beurmann, V. Thangadurai, *Structure and lithium ion conductivity of garnet-like $Li_5La_3Sb_2O_{12}$ and $Li_6SrLa_2Sb_2O_{12}$*, Materials Research Bulletin 43, 2579-2591, **2008**

[27] V. Thangadurai, J. Schwenzel, W. Weppner *Development of all-solid state lithium batteries*, Solid State Ionics, Proc. Asian Conf. 10th, Kandy, Sri Lanka, 723-734, **2006**

[28] V. Thangadurai, J. Schwenzel, W. Weppner, *Tailoring Ceramics for Specific Applications: A Case Study of the Development of All-Solid-State Lithium Batteries*, Ionics 11, 11-23, **2005**

[29] M. P. O'Callaghan, E. J. Cussen, *The structure of the lithium-rich garnets $Li_6SrLa_2M_2O_{12}$ and $Li_{6.4}Sr_{1.4}La_{1.6}M_2O_{12}$ (M=Sb, Ta)*, Solid State Sciences 10, 390-395, **2008**

[30] R. Murugan, W. Weppner, P. Schmid-Beurmann, V. Thangadurai, *Structure and lithium ion conductivity of bismuth containing lithium garnets $Li_5La_3Bi_2O_{12}$ and $Li_6SrLa_2Bi_2O_{12}$*, Materials Science and Engineering B 143, 14-20, **2007**

[31] V. Thangadurai, H. Kaack, W. Weppner, *Novel Fast Lithium Ion Conduction in Garnet-Type $Li_5La_3M_2O_{12}$ (M=Nb, Ta)*, Journal of the American Ceramic Society 86 [3], 437-440, **2003**

[32] E. J. Cussen, *The structure of lithium garnets: cation disorder and clustering in a new family of fast Li^+ conductors*, The Royal Society of Chemistry, Chemical Communication, 412-413, **2006**

[33] V. Thangadurai, W. Weppner, *$Li_6ALa_2Ta_2O_{12}$ (A=Sr, Ba): Novel Garnet-Like Oxides for Fast Lithium Ion Conduction*, Advanced Functional Materials 15, No.1, 107-112, **2005**

[34] D. Kikutani, T. Okumura, T. Fukutsuka, Y. Uchimoto, *Local Structure and Li-Ion Conduction in $Li_{5+x}La_{3-x}Sr_xNb_2O_{12}$ having Garnet-related Structure*, **2008**

[35] V. Thangadurai, W. Weppner, *Effect of sintering on the ionic conductivity of garnet-related structure $Li_5La_3Nb_2O_{12}$ and In- and K-doped $Li_5La_3Nb_2O_{12}$*, Journal of Solid State Chemistry 179, 974-984, **2006**

[36] R. Murugan, V. Thangadurai, W. Weppner, *Lithium ion conductivity of $Li_{5+x}Ba_xLa_{3-x}Ta_2O_{12}$ (x=0-2) with garnet-related structure in dependence of the barium content*, Ionics 13, 195-203, **2007**

[37] V. Thangadurai, W. Weppner, *$Li_6ALa_2Nb_2O_{12}$ (A=Ca, Sr, Ba): A New Class of Fast Lithium Ion Conductors with Garnet-Like Structure*, Journal of American Ceramic Society 88, 411-418, **2005**

[38] J. Percival, E. Kendrick, P.R. Slater, *Synthesis and characterisation of the garnet-related Li ion conductor, $Li_5Nd_3Sb_2O_{12}$*, Materials Research Bulletin 43, 765-770, **2008**

[39] V. Thangadurai, W. Weppner, *Recent progress in solid oxide and lithium ion conducting electrolyte research*, Ionics 12, 81-92, **2006**

[40] V. Thangadurai, W. Weppner, *Investigations on electrical conductivity and chemical compatibility between fast lithium ion conducting garnet-like $Li_6BaLa_2Ta_2O_{12}$ and lithium battery cathodes*, Journal of Power Sources 142, 339-344, **2005**

[41] L. Van Wüllen, T. Echelmeyer, H.-W. Meyer, D. Wilmer, *The mechanism of Li-ion transport in the garnet $Li_5La_3Nb_2O_{12}$*, Physical Chemistry Chemical Physics 9, 3298-3303, **2007**

[42] B. Koch, M. Vogel, *Lithium ionic jump motion in the fast solid ion conductor $Li_5La_3Nb_2O_{12}$*, Solid State Nuclear Magnetic Resonance 34, 37-43, **2008**

[43] V. Thangadurai, S. Adams, W. Weppner, *Crystal Structure Revision and Identification of Li^+-Ion Migration Pathways in the Garnet-like $Li_5La_3M_2O_{12}$ (M=Nb, Ta) Oxides*, Chemistry of Materials 16, 2998-3006, **2004**

[44] M. Kotobuki, K. Kanamura, Y. Sato, K. Yamamoto, T. Yoshida, *Fabrication of All-Solid-State lithium battery using novel garnet type electrolyte*, **2010**

[45] E. J. Cussen, *Structure and ionic conductivity in lithium garnets*, Journal of Materials Chemistry, (Advance Article), **2010**
http://www.electrochem.org/meetings/scheduler/abstracts/217/0361.pdf

[46] D. Mazza, *Remarks on a ternary phase in the La_2O_3-Me_2O_5-Li_2O system (Me=Nb,Ta)*, Materials Letters 7, No. 5-6, 205-207, **1988**

[47] H. Hyooma, K. Hayashi, *Crystal structures of $La_3Li_5M_2O_{12}$ (M=Nb, Ta)*, Materials Research Bulletin 23, Issue 10, 1399-1407, **1988**

[48] J. Isasi, M. L. Veiga, R. Saez-Puche, A. Jerez, C. Pico, *Synthesis, structure determination and magnetic susceptibilities of the oxides Ln3Li5Sb2O12 (Ln≡Pr, Nd, Sm)*, Journal of Alloys and Compounds 177, 251-257, **1991**

[49] P. Pasierb, R. Gajerski, M. Rokita, M. Rekas, *Studies on the binary system Li_2CO_3-$BaCO_3$*, Physica B Condensed Matter 304, 463-476, **2001**

[50] Mc.Murdie, Levin, *Phase Diagrams for Ceramists*, The American Ceramic Society, Vol. 1, Fig. 179, **1969**

7.1. List of figures:

7.2. List of tables:

Curriculum vitae

Personal details

Name:	Barbara Stiaszny
Date of birth:	09.08.1987
Place of birth:	Linz
Parents:	Maria and Dr. Peter Stiaszny
Nationality:	Austria

Education

1993 – 1997:	Primary School Mauthausen
1997 – 2005:	Secondary Grammar School Linz Fadingerstraße
June 2005:	School leaving exam passed with successfulness
Since 2005:	Academic studies of Chemistry at the University of Vienna

Professional Experience

July 2007: Internship at the voestalpine Stahl Linz: Department for analysis

Different analysis of process effluents, determination of chlorine in oil residues and absorption oils, concentration and NO_x-determination in concentrated sulphuric acid

July 2008: Internship at the Technical University Munich: Institute for mechanical engineering, department for materials science and materials mechanics

Metallographic investigations and analysis of steel samples with bright field microscope, dilatometer and REM, determination of residual austenite content, determination of residual stress in aluminium component parts

January 2009: Tutor at the Institute of Inorganic Chemistry at the University of Vienna